FEDERAL UNIVERSITY OF SÃO CARLOS
EXACT AND TECHNOLOGY SCIENCES CENTER
GRADUATE PROGRAM IN CHEMICAL ENGINEERING

PATRICIA TREVISANI JUCHEN

Electrochemical desalination using polyglycerol activated carbon: Electrode, cell, and process development

Dessalinização eletroquímica usando carvão ativado de poliglicerol: Desenvolvimento do eletrodo, célula e processo

SÃO CARLOS

2022

PATRICIA TREVISANI JUCHEN

Electrochemical desalination using polyglycerol activated carbon: Electrode, cell, and process development

Dessalinização eletroquímica usando carvão ativado de poliglicerol: Desenvolvimento do eletrodo, célula e processo

Ph.D. thesis presented to the Graduation Program in Chemical Engineering of the Federal University of São Carlos as part of the requirements to obtain the title of Ph.D. in Chemical Engineering, in the field of Research and Development of Chemical Processes.

Advisor: Prof. Dr. Luís Augusto Martins Ruotolo

SÃO CARLOS

2022

UNIVERSIDADE FEDERAL DE SÃO CARLOS

Centro de Ciências Exatas e de Tecnologia
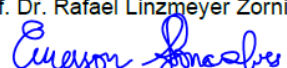Programa de Pós-Graduação em Engenharia Química
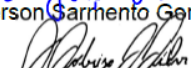

Folha de Aprovação

Defesa de Tese de Doutorado da candidata Patricia Trevisani Juchen, realizada em 18/11/2022.

Comissão Julgadora:

Prof. Dr. Luis Augusto Martins Ruotolo (UFSCar)

Prof. Dr. Rafael Linzmeyer Zornitta (HERAEUS)

Prof. Dr. Emerson Sarrhento Gonçalves (ITA)

Prof. Dr. Rodrigo Sanchotene Silva (UERGS)

Prof. Dr. Helio Ribeiro (Mackenzie)

O Relatório de Defesa assinado pelos membros da Comissão Julgadora encontra-se arquivado junto ao Programa de Pós-Graduação em Engenharia Química.

This thesis is dedicated to my parents, Carlos and Sandra, and my loving fiancé Thiago, who have been a constant source of support and encouragement during the challenges of graduate school and life.

ACKNOWLEDGEMENTS

RESUMO

A deionização capacitiva (DIC) surgiu como uma tecnologia eletroquímica promissora para a dessalinização de água salobra, a qual promove a eletrossorção de íons na dupla camada elétrica. Nos últimos anos, houve um crescimento significativo dos estudos sobre deionização capacitiva, porém, questões desafiadoras ainda persistem, como a obtenção de eletrodos de carbono de baixo custo, com alta capacidade de eletrossorção e estabilidade ao longo dos ciclos de eletrossorção/dessorção, assim como um melhor entendimento como os aspectos hidrodinâmicos que influenciam a transferência de massa e a eficácia do processo. Neste sentido, o objetivo desta tese foi desenvolver um eletrodo de carvão ativado utilizando como precursor um polímero obtido a partir do glicerol residual do biodiesel e investigar os efeitos da arquitetura de diferentes células DIC na dessalinização eletroquímica.

Os resultados mostraram que foi possível preparar eletrodos empregando como precursor o polímero de glicerol residual. Nos experimentos de eletrossorção, o eletrodo PGAC demonstrou estabilidade ao longo de 50 ciclos, aplicando-se voltagens de 1,1 V e 1,2 V, na configuração simétrica, comportamento desejável para permitir o processo por longos períodos de operação. No entanto, ao se aplicar 1,4 V, o potencial do eletrodo positivo ultrapassou o potencial limite de estabilidade anódica, ocasionando reações de oxidação no ânodo e, consequentemente, perda da capacidade de dessalinização. As configurações assimétrica e com membrana (MCDI) foram também analisadas com o intuito de melhorar a capacidade de adsorção de sal (*salt adsorption capacity - SAC*). Utilizando-se configuração assimétrica foi possível minimizar o efeito deletério da expulsão de co-íons, visto que houve um aumento de eficiência de carga (Q_E) de 62,9% para 88,4%. Já na configuração MCDI, a aplicação de membranas de troca iônica levou a um aumento significativo dos valores de *SAC* e Q_E. Essa melhoria é atribuída à presença dos co-íons repelidos dos microporos e que são impedidos de migrar para a solução devido à presença da membrana. Esses co-íons acumulam-se então nos macroporos do material, constituindo-se em uma força de atração adicional dos contra-íons, uma vez que a eletroneutralidade deve ser mantida. Esses resultados mostraram que o eletrodo PGAC, além de ser um material de baixo custo, revelou-se promissor para dessalinização de água salobra por deionização capacitiva.

Na sequência, a comparação de diferentes células de DIC evidenciou que suas arquiteturas influenciaram na transferência de massa e cinética do processo. Para um eletrodo de menor

espessura, a célula *flow-by* (CFB) apresentou melhor performance de dessalinização comparada à célula *flow-through* (CFT), devido à menor resistência ao carregamento da dupla camada elétrica e maior difusão nos microporos. Porém, para um eletrodo mais espesso, uma notável redução de *SAC* ocorreu na CFB, resultado atribuído à menor transferência de massa da superfície do eletrodo até os sítios ativos de adsorção. Este efeito não ocorreu ao se usar a CFT, pois nesta arquitetura o transporte convectivo de massa nos poros intersticiais promoveu uma cinética mais rápida quando comparada à CFB. Considerando esses resultados, uma célula de fluxo com percolação (CFP) foi proposta para combinar os aspectos benéficos das arquiteturas de célula investigadas anteriormente. Com o fluxo do eletrólito percolando o eletrodo e sendo perpendicular ao campo elétrico, a CFP permitiu aumentar o parâmetro "*optimized salt removal*" (*OSR*), devido à transferência de massa mais rápida promovida pela permeação do eletrólito através do filme de carbono do eletrodo. Uma investigação do tamanho de partícula utilizado na elaboração do eletrodo mostrou que esse tamanho influencia diretamente no fenômeno de transferência de massa, sendo possível aumentar as constantes cinéticas com partículas menores, porém as mesmas promoveram um *SAC* menor devido a alterações nas propriedades texturais. Esses resultados evidenciaram que existe um tamanho de partícula ideal para obter um valor elevado de *OSR*. Por fim, a análise do modo galvanostático e *quase single-pass* foram analisadas utilizando a CFP. Os resultados mostraram que a vazão e a densidade de corrente mais elevadas aceleram a cinética, mas atingem rapidamente o potencial de corte, afetando o *OSR*. Logo as condições operacionais que mostraram serem mais efetivas para obter o maior valor de *OSR* foram 7 ml min^{-1} e 1 mA cm^{-2}, evidenciando a importância de analisar simultaneamente o *SAC* e o tempo de ciclo.

ABSTRACT

Capacitive deionization (CDI) has emerged as a promising electrochemical technology for the desalination of brackish water, which promotes the electrosorption of ions in the electrical double layer. In recent years, there has been significant growth in studies on capacitive deionization, however, challenging issues still persist, such as obtaining low-cost carbon electrodes with high electrosorption capacity and stability over electrosorption/desorption cycles, as well as a better understanding of how the hydrodynamic aspects influence mass transfer and process efficiency. In this sense, the objective of this thesis was to develop an activated carbon electrode using a polymer obtained from residual glycerol from biodiesel as a precursor and to investigate the effects of the architecture of different CDI cells on electrochemical desalination.

The results showed that it was possible to prepare electrodes using residual glycerol polymer as the precursor. In electrosorption experiments, the PGAC electrode demonstrated stability over 50 cycles, applying voltages of 1.1 V and 1.2 V, in a symmetrical configuration, desirable behavior to allow the process for long periods of operation. However, when applying 1.4 V, the positive electrode potential exceeded the limit potential of anodic stability, causing oxidation reactions at the anode and, consequently, loss of desalination capacity. The asymmetric and membrane configurations (MCDI) were also analyzed in order to improve the salt adsorption capacity (SAC). Using an asymmetric configuration, it was possible to minimize the deleterious effect of co-ion repulsion, since there was an increase in charge efficiency (Q_E) from 62.9% to 88.4%. In the MCDI configuration, the application of ion exchange membranes led to a significant increase in the values of SAC and Q_E. This improvement is attributed to the presence of co-ions repelled from the micropores and which are prevented from migrating into the solution due to the presence of the membrane. These co-ions then accumulate in the macropores of the material, constituting an additional force of attraction of the counter-ions, since electroneutrality must be maintained. These results showed that the PGAC electrode, in addition to being a low-cost material, proved to be promising for brackish water desalination by capacitive deionization.

In sequence, the comparison of the different CDI cells showed that the cell architectures influenced the mass transfer and kinetics of the process. For a thinner electrode, the flow-by cell (FBC) showed better desalination performance compared to the flow-through cell (FTC), due to the lower resistance to charging of the electrical double layer and higher diffusion in the micropores. However, for a thicker electrode a notable reduction of SAC occurred in the FBC, a result attributed to the lower mass transfer from the electrode surface to the adsorption active sites. This effect did not occur when using FTC, because in this architecture the convective transport of mass in the

interstitial pores promotes a faster kinetics when compared to FBC. Considering these results, a percolation flow cell (PFC) was proposed, to combine the beneficial aspects of previously investigated cell architectures. With the flow of electrolyte percolating through the electrode and being perpendicular to the electric field, the PFC allowed the increase of optimized salt removal (OSR), due to faster mass transfer promoted by the permeation of the electrolyte through the carbon film of the electrode. An investigation of the particle size used in the preparation of the electrode showed that this size directly influences the mass transfer phenomenon, being possible to increase the kinetics constants with smaller particles, but they promoted a lower *SAC* due to changes in textural properties. These results showed that there is an ideal particle size to obtain a high *OSR* value. Finally, galvanostatic and quasi-single-pass mode analysis were analyzed using PFC. The results showed that higher flux flow and current density accelerate the kinetics, but quickly reach the cutting potential, affecting the *OSR*. Therefore, the operating conditions that showed to be more effective to obtain the highest *OSR* value were 7 ml min^{-1} and 1 mA cm^{-2}, highlighting the importance of simultaneously analyzing *SAC* value and cycle time.

SUMMARY

LIST OF TABLES

LIST OF FIGURES

NOMENCLATURE

A_0	Admittance	$[\text{S s}^{1/2}\,\text{cm}^{-2}]$
$A_{c\text{-}s}$	Cross-sectional area available for the electrolyte flow	$[\text{m}^2]$
C_0	Initial salt concentration	$[\text{mg L}^{-1}]$
C_t	Salt concentration	$[\text{mg L}^{-1}]$
C_{INT}	Capacitance at the electrolyte/electrode interface	$[\text{F g}^{-1}]$
C_{EIS}	Capacitance inside the micropores	$[\text{F g}^{-1}]$
C_{min}	Lowest observed capacitance	$[\text{F g}^{-1}]$
C_{GCD}	Average capacitance obtained from charge-discharge	$[\text{F g}^{-1}]$
C_{CV}	Total specific capacitance	$[\text{F g}^{-1}]$
$C_{s,CV}$	Specific capacitance	$[\text{F g}^{-1}]$
$C_{s,EIS}$	EIS specific capacitance	$[\text{F g}^{-1}]$
E_1	Lower value of the potential window	$[\text{V}]$
E_2	Upper value of the potential window	$[\text{V}]$
E_{cc}	Cutting cell potential	$[\text{V}]$
E_{cell}	Cell potential	$[\text{V}]$
E_{EQ}	Equilibrium potential	$[\text{V}]$
D_{50}	Median particle diameter	$[\mu\text{m}]$
d_{50}	Average pore diameter	$[\text{nm}]$
E_{cc}	Cutting cell potential	$[\text{V}]$
E_0	Sort-circuit potential	$[\text{V}]$
$E_{pw}+$	Anodic potential limit	$[\text{V}]$
E_{PZC}	Potential of zero charge	$[\text{V}]$
F	Faraday constant	$[\text{C mol}^{-1}]$
I	Current	$[\text{A}]$
I_D/I_G	Raman peak intensity ratio	-
IR_{drop}	Ohmic drop	$[\text{V}]$
I_d	Discharge current	$[\text{A}]$
j	Imaginary number	-
k_e	Pseudo-first order kinetic constant for electrosorption	$[\text{s}^{-1}]$
k_d	Pseudo-first order kinetic constant for and desorption	$[\text{s}^{-1}]$

m	Mass of activated carbon in the working electrode	[g]
M_{NaCl}	Molecular weight of NaCl	[mg mol^{-1}]
m_E	Total mass of the active material in both electrodes	[g]
m_{rem}	Mass of ions removed from the solution	[mg]
N	Ideality factor	-
N_A	Avogadro constant	[mol^{-1}]
N_{cycles}	Number of cycles	-
OSR	Optimized salt removal	[mg g^{-1} day^{-1}]
Q^0	Non-ideal capacitance	[S s^N]
Q_E	Charge efficiency	[%]
Q_{neg}	Accumulated charge during the discharging scan	[C]
Q_{pos}	Accumulated charge during the charging scan	[C]
R	Faradaic Fraction	-
$R\text{-}Value$	R-value calculed by Faradaic Fraction	-
R_{pos}	$R\text{-}Value$ for anodic window	-
R_{CT}	Charge-transfer resistance	[Ω]
R_{Ω}	Ohmic resistance	[Ω]
SAC	salt adsorption capacity	[mg g^{-1}]
SSA	Specific surface area	[m² g^{-1}]
SSA_{BET}	SSA calculated by the Brunauer-Emmett-Teller equation	[m² g^{-1}]
$t_{e\text{-}opt}$	Optimized electrosorption time	[s]
t_d	Desorption time	[s]
u	Flow velocity	[m s^{-1}]
V	Electrolyte volume	[L]
V_{mes}	Mesopore volume	[cm³ g^{-1}]
V_{mic}	Micropore volume	[cm³ g^{-1}]
V_T	Total pore volume	[cm³ g^{-1}]
W	Warburg element	[Ω s$^{-1/2}$]
Y_A	Polyglycerol activation yield	[%]
Y_C	Polyglycerol carbonization yield	[%]
Y_P	Polyglycerol polymerization yield	[%]
Y_T	PGAC treatment with HF yield	[%]

Y_0	Overall yield	[%]
Z''	Imaginary part of the impedance spectrum	-
z	Ion valence	-
$\%V_{mes}$	Percentage of mesopores	[%]

SYMBOLS

η	Energy consumption	[J mg^{-1}]
v	Scan rates	[mV s^{-1}]
ω	Angular frequency	[rad s^{-1}]
σ	Conductivity	[μS cm^{-1}]
ε	Interparticle porosity	[-]
ξ	Electrode thicknesses	[μm]
θ	Contact angle	[°]
δ	Diffusion film thickness layer	[μm]

ABBREVIATIONS

AC	Activated carbon
BC	Blade-casting
CB	Carbon-black
CDI	Capacitive deionization
C-MCDI	CDI using solely cation exchange membrane
CPE	Constant phase element
CV	Cyclic voltammetry
DTG	Derivative thermogravimetric analysis
FS	Free-standing
GCV	Galvanostatic charge-discharge
EDL	Electric double layer
EIS	Electrochemical impedance spectroscopy
FBC	Flow-by cell
FTC	Flow-through cell
HF-PGAC	PGAC treated with aqueous HF solution
HF-PGAC90	90 wt% of HF-PGAC
HF-PGAC85CB10	85 wt% of HF-PGAC and 10% of CB
IEMs	Ion exchange membranes
MCDI	Membrane capacitive deionization
NMP	N-methyl-pyrrolidone
N-PGAC	PGAC from chemical surface treatment using HNO_3
PFC	Percolation flow cell
PG	Polyglycerol
PGC	Carbonized polyglycerol
PGAC	Polyglycerol activated carbon
PGACE	PGAC electrode
PGAC*	PGAC from analytical grade glycerol
PGAC95	95 wt% of PGAC
PGAC90	90 wt% of PGAC
PSD	Pore size distribution
PSW	Potential stability window
PVDF	Polyvinylidene fluoride
PTFE	Polytetrafluoroethylene
SOG	Surface oxygen groups
TG	Thermogravimetric analysis

1   CHAPTER

INTRODUCTION

1.1   Broad context

Water insufficiency worldwide is expected to occur in the coming decades, and it is already a world-critical issue since the availability of affordable clean water is unavailable to one out of seven people worldwide [1,2]. The increase in substantial consumption, population growth, climate change, industrial development, and widespread water pollution contribute to water scarcity issue. In this regard, the development of new technologies has received significant attention for reclaiming this valuable life-sustaining resource.

Seawater contains approximately 35,000 mg L^{-1} of dissolved salts, while brackish water contains 1000 mg L^{-1} [3]. For water to be considered appropriate for consumption, the concentration of salts must be below or equal to 500 mg L^{-1} of total dissolved solids [4]. In relation to quantity, brackish water represents 1% of the overall water in the world, while freshwater accounts only for 0.8%, and the general part is seawater with 96.5% [5]. Brackish water is mainly found in Saudi Arabia, Egypt, Turkey, Northwestern China, and the western part of the United States [5]. Even in Brazil, where a large volume of superficial water is available, issues related to this resource have also become relevant because such water is poorly distributed in the national territory and some microregions have endemic drought spells [6]. The remote communities of Brazilian semiarid regions have brackish groundwater available and its desalination can be a viable alternative to produce clean water for isolated communities with scarce freshwater resources [7]. In addition, the desalination of water from the Guarani Aquifer, which in some regions is brackish, could supply water to the population of the southern region, where droughts have been far more frequent [6].

From this perspective, desalination technologies are important to help overcome the demand for freshwater. Therefore, saltwater desalination is considered a key strategic solution to mitigate the problem of freshwater shortage and sustain future generations across the globe.

1.2   Desalination technologies

In order to obtain potable water, desalination technologies can use different separation methods, such as the use of membranes and thermal or chemical processes. The conventional technologies used for water desalination are multi-stage flash distillation, reverse osmosis, and electrodialysis.

Distillation is a thermal process that uses heat exchange to evaporate water, which condenses and consequently separates from the salts. This method can also be used to separate other impurities contained in water such as other dissolved solids, such as iron, manganese, and magnesium. The multiple-stage flash distillation (Figure 1.1(a)) is widely used because of its reliability and simplicity [8,9]. In this process, salt water is evaporated by reducing pressure and increasing temperature. In this technique, it is possible to reduce energy consumption because the water to be desalinated is preheated when passing through the closed pipes also used as a heat exchange to condense the evaporated water. Then the temperature of the saltwater fed into the process increases, reducing the amount of energy required to evaporate it. Separation by distillation is limited as the removal of volatile organic compounds, solvents, and pesticides with boiling points close to or lower than water are vaporized along with the water inside the column, thus another process is necessary to perform the separation of these. Another disadvantage of this process is high energy consumption in the range from 15 to 58 kW h m^{-3} [10], which makes its application on an industrial scale unfeasible.

Reverse osmosis (Figure 1.1(b)) is one of the most used processes for desalination, in which it performs the separation through the use of membranes and high pressure. The porous membrane used allows the passage of water molecules and prevents the passage of undesirable components, using pressure as a driving force [11]. In reverse osmosis a high pressure, higher than the osmotic pressure, is applied which reverses the flow and saline solution moves across the membrane, and salts are retained in the membrane, resulting in brine and purified water streams [11]. The energy required to desalinate water by this process is around 2.9 and 3.7 kWh m^{-3} [3]. Furthermore, the use of membranes is a drawback due to membrane fouling problems and because their replacement is expensive. Commercial interest in RO technology is increasing globally due to the continuous advances in membrane materials, process design, feed pre-treatment, and energy recovery [12].
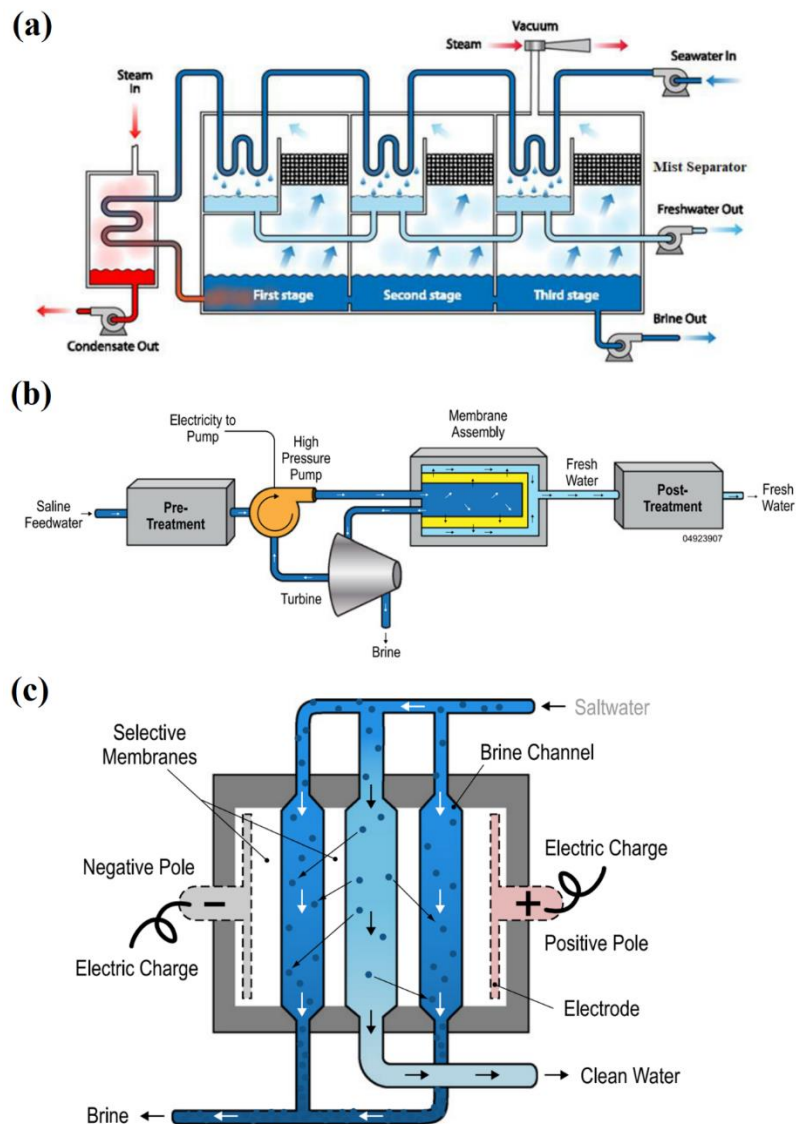
Figure 1.1. Desalination technologies: Multi-stage flash distillation **(a)**; Reverse osmosis **(b)**; and Electrodialysis **(c)** [13].

Electrodialysis also uses a membrane to carry out the separation process, but unlike reverse osmosis, a high voltage is applied as a driving force. The process uses parallel electrodes separated by membranes forming individual units called pairs of cells, these units may vary depending on the process need. In electrodialysis (Figure 1.1(c)), the pressure applied to the process is lower than that applied in reverse osmosis and membranes are selective, allowing the cations migration through the cationic membrane and anions through anionic membrane [3]. After applying a potential to the cell, ion hydroxyl (OH^-) formation occurs on the cathode and ion hydronium (H^+) at the anode due to electrolysis of water. In this way, the chloride crosses the anion exchange membrane to the anode

chamber, while sodium moves through the cation exchange membrane to the cathode chamber. These ions' movement to compartments results in compartments with a brine stream and another with a diluted stream. To carry out the regeneration of encrusted membranes reversing the polarity is applied causing inversion between the cathode and anode. This technology is limited compared to other technologies, being economically competitive for concentrations up to 6000 mg L^{-1} due to energy cost [3].

1.3 Capacitive deionization (CDI)

Capacitive deionization (CDI) has emerged as a promising technology to desalinate brackish water, with high energy efficiency and cost-effectiveness potential for brackish water desalination compared to conventional desalination technologies, and also an environmentally friendly chemical-free process. The principle of the CDI process relies on a low electrical potential difference applied between two porous electrodes to remove salt ions from brackish water. The applied potential difference generates an unbalance of charges that induces the transport of electrically charged species (ions) to oppositely charged electrodes due to electrostatic attraction. Thus, cations and anions will be removed from the aqueous phase and immobilized in the electric double layer (EDL) formed at the negatively and positively polarized electrodes, respectively, as shown in Figure 1.2(a).
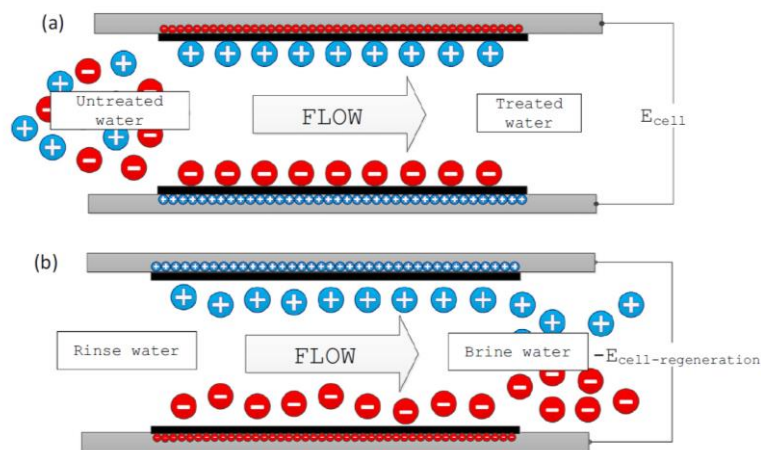
Figure 1.2. Scheme of capacitive deionization device **(a)** electrosorption and **(b)** desorption [14].

The CDI mechanism consists of a two-step process, as shown in Figure 1.2. The first step is electrosorption, where the ions are immobilized in the EDL, and as a result, the desalinated water

stream is produced (Figure 1.2.(a)). After some time, the accessible pore volume is completely saturated with electrosorbed ions, and the maximum storage capacity of the electrodes is reached. Short-circuiting or reversing electric potential is applied for electrode regeneration, and ions are released back into the bulk solution. This step is called desorption, which produces a waste brine stream (Figure 1.2.(b)). Thus, desalination through CDI operates usually in a non-continuous mode with alternate electrosorption and desorption steps that complete an operational cycle. When irreversible reactions are avoidable, high-capacity retention over CDI cycles can be achieved.

For low salt concentration, the CDI offers significant advantages as low energy requirements due to the relatively low voltage required to operate the system, but mainly, due to the possibility of recovering part of the energy used for the electrosorption of ions through electrode regeneration, which reduces the energy cost [15,16]. These two advantages make CDI an attractive energy-efficient option for brackish water desalination. Additionally, the CDI process has other advantages, such as the absence of hydraulic pressure, which allows a simple equipment structure and operation, and low environmental impact due to no hazardous substances generation [17–19]. Therefore, CDI technology has a strong potential to become a competitor with other desalination technologies, especially for small desalination devices or plants.

1.4   CDI overview

The historical background of CDI shows the pioneering work of water desalination started in 1960s when the first study was performed by Blair and Murphy [20]; at that time the concept of water desalination was called "electrochemical demineralization of water". In the 1970s, the Electric Double Layer (EDL) theory was identified as the mechanism of ions removal by Johnson and co-workers [21], and after, the study by Johnson and Newman (1971) [22] indicated that the ion capacity of the electrode depends on the available surface area and applied cell voltage. After 2009, academic interest in CDI increased exponentially, as shown in Figure 1.3(a). The first studies aimed to use the CDI process for water desalination and softening, especially for brackish water desalination to obtain drinking water [3]. More recently, CDI has also been applied to the removal of toxic metal ions from wastewater, which could even enable the reuse of water [23,24].
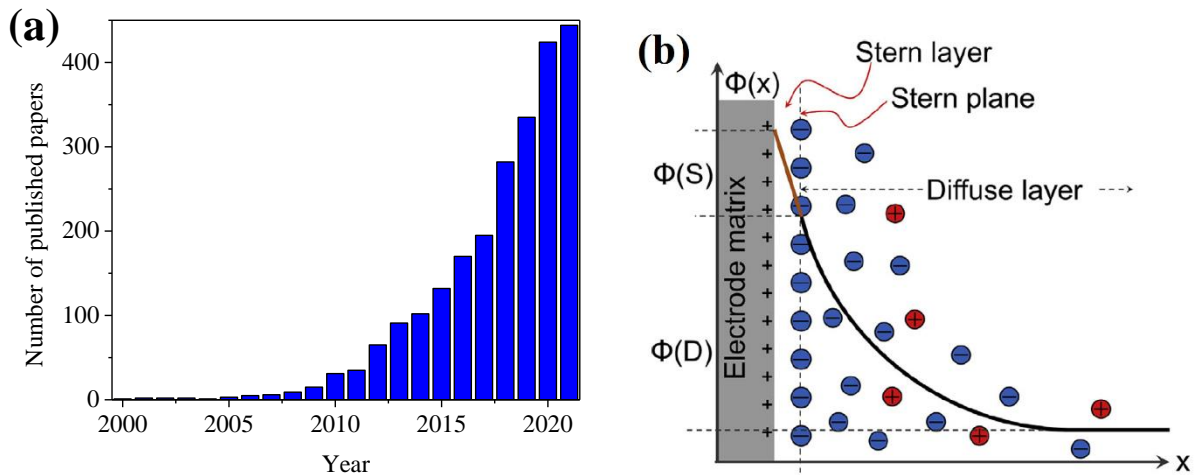
Figure 1.3. (a) Evolution of the number of publications regarding capacitive deionization since 2000 (Web of Science; keyword: "capacitive deionization"). **(b)** Schematic structure of electrical double layer according to the Gouy-Chapman-Stern theory for single planar EDL [25].

The Gouy-Chapman-Stern theory can be applied to describe the structure and interfacial properties between an electronic conductor and an aqueous electrolyte in capacitive deionization. The electrical capacity of the interface can be expressed by the sum of two capacitors in series, one being the capacitance of the compact layer, and the other being the capacitance of the diffuse layer. The EDL formed within micropores inside CDI electrodes, refers to the two layers next to the electrode-solution interface where ions are compactly and diffusively distributed (Figure 1.3(b)) [26]. Considering these aspects, many of the variables that affect the EDL and its ability to store ions (capacitance) also apply to CDI, such as the properties of the electroactive material and the effective electric potential applied in counterions electrosorption.

In this regard, many CDI studies aiming to optimize CDI performance focus on understanding the electrochemical and textural properties of the electrode, such as pore volume, specific surface area (SSA), pore size distribution, electronic conductivity, and electrochemical stability [2]. The electrode structure is highly important since micropores describe the pore space inside carbon particles, then microporous materials with high SSA and high electronic conductivity have shown to be the most promising. Moreover, mesopores could offer pathways for ion transport, so large mesoporous structures could be an effective strategy for faster ion diffusion and enhance accessible electron-transfer pathways [27,28].

Another important aspect of the CDI mechanism concerns the presence of different functional groups on the carbon electrode surface, which will determine its ability to remove ions from the solution. For instance, positive surface groups may enhance the desalination performance of the positive electrode and lower the performance if the material is applied as the negative electrode [29,30]. In this sense, different approaches were performed to modify the surface chemistry of carbon materials by different carbonization and activation methods, oxidation reactions, and electrochemical/physical/chemical treatments [28,31]. The material produced is expected to have a lower or higher amount of carboxylic, phenolic, carbonyl, anhydride, and lactone groups, among others, depending on the reactions provoked by carbonization and activating methods. These functional groups, besides improving the electrode surface wettability, also influence the electrochemical activity and textural properties [27,31,32]. Recent studies showed that surface chemistry can change the potential of zero charge of the electrodes, affecting the co-ion repulsion effect and, consequently, the performance of electrodes used for CDI [29,33].

The quantity of ions adsorbed on the carbon electrode is proportional to the applied cell potential. Thus, to increase the electrosorption, the highest potential within a range in which Faradaic reactions do not occur should be applied. Application of potentials out of the electrode stability window will cause parasitic reactions, such as water splitting, oxygen reduction at the cathode, and electrooxidation at the anode, which can modify the electrode surface [34–37]. Except when used to create pseudo capacitance, the Faradaic reactions are detrimental to CDI performance, decreasing the electrode lifespan, increasing energy consumption, and reducing the desalination efficiency since part of some charges are deviated to faradaic reactions instead of electrosorption [34]. Usually, the cell potential (E_{cell}) of 1.2 V is applied in the CDI cell to avoid faradaic reactions, but the presence of other resistive elements, such as membranes, leads to additional ohmic drop, and this value of E_{cell} could be revised. In summary, the electrode potential control is important to ensure electrode stability, allowing a high number of charge/discharge cycles in the CDI process.

In addition to the studies regarding the electrode materials, efforts have been devoted to developing new CDI cell configurations, such as the membrane CDI (MCDI). In MCDI, ion exchange membranes are placed in front of each electrode, specifically, a cation exchange membrane is placed adjacent to the cathode, and an anion exchange membrane is placed adjacent to the anode. The use of MCDI is one strategy to avoid co-ion repulsion and, consequently, enhance salt adsorption capacity and the charge efficiency of the process. The co-ions repulsion effect

occurs when an electric potential is applied and the co-ions inside the pores of carbon are expelled and end up in the spacer channel electrode, this effect causes a reduction in desalination efficiency [26,38]. Using a membrane cell, the co-ions are expelled and prevented from leaving the spacer channel, then remain stored in the macropores of the electrode. In order to maintain electroneutrality, they could serve as an extra storage space for counterions, improving salt adsorption and charge efficiency [19,39,40].

Other operational strategies to optimize CDI desalination performance include the use of the asymmetric configuration, which can be assessed by using electrodes with different thicknesses, sizes, masses, materials, and surface charges [41,42]. The main reasons for the desalination improvements observed using asymmetric configuration are (i) the adequate position of the point of zero charge (E_{PZC}) of the electrode, which maximizes the effective electrode potential, minimizing the co-ion repulsion, and (ii) the introduction of additional attractive forces that act to remove the counterions from the electrolyte solution [43–45].

1.5   CDI electrode materials

Electrode material development is fundamental for achieving high desalination capacity and removal efficiency. A suitable CDI electrode material, based on electric double layer formation, should have a high specific surface area available for electrosorption, proper pore size distribution, high electronic conductivity, fast response of the entire surface area to electrosorption/desorption cycles, good wettability (or hydrophilicity), and low-cost [46]. Considering these aspects, usually, CDI electrodes are made of porous carbon materials, especially activated carbons.

Significant efforts have been made to develop high adsorption capacity electrodes for CDI by fabricating different carbon-based materials, such as graphene [47], nitrogen-doped graphene [48], nanotubes [49], aerogel [50], and carbide-derived carbon [42]. Some of these materials presented promising capacitive performance, but most of them are laborious to produce and expensive, imposing restrictions on large-scale cells [32,51,52]. Recent studies have been devoted to the production of low-cost CDI electrodes. In this sense, the use of wastes and biowastes as precursors to produce novel activated carbons has been encouraged, such as watermelon peel [53], waste coffee grounds [54], sugarcane bagasse fly ash [28], rice husk [55,56], and lignin [33].

In the literature, the value of the salt adsorption capacity (*SAC*) by CDI desalination varies using activated carbon electrodes produced from biomass precursors. For example, when jackfruit peels [57] and palm shells [58] were used as precursors of activated carbon, low *SAC* values of 5.74 mg g^{-1} and 3.3 mg g^{-1} were obtained, respectively. However, when using watermelon peel as the precursor, a high *SAC* of 17.38 mg g^{-1} was achieved [53]. These results reveal that the CDI performance can vary significantly depending on textural and electrochemical properties resulting from the type of precursor material used in electrode preparation.

1.6   Crude glycerol

The environmental concerns and the economic dependence on fossil fuel reserves have stimulated the search for alternative fuels, produced from renewable feedstocks. In this context, biodiesel has gained great attention [59,60]. As a by-product of the biodiesel production process, large volumes of crude glycerol are produced, leading to an increasing oversupply in the glycerol market due to the expansion of biodiesel plants worldwide [61]. As a product of the transesterification process depicted in Figure 1.4, glycerol is formed from the chemical reaction between vegetal oils or animal fat and alcohol, in the presence of a homogeneous catalyst [62]. Approximately 10-20% of the total volume of biodiesel produced is made up of crude glycerol, which, in turn, contains between 75–80% of glycerol and impurities such as methanol, soap, fatty acid methyl esters, and alkaline catalyst residues [62]. In order to be used in different applications and industrial processes, glycerol needs expensive purification processes, such as vacuum distillation, ion exchange, and/or nanofiltration [63].
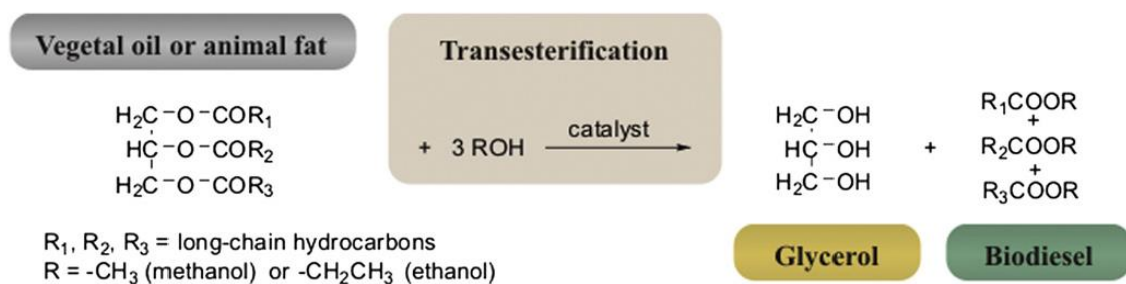
Figure 1.4. Biodiesel production: transesterification reaction [64]

Glycerol polymerization is an etherification process resulting in polyglycerol, which is applied in the production of polyurethanes, polyesters, epoxy resins, biodegradable surfactants, lubricants, and

cosmetics [65–68]. Moreover, polyglycerol is used as feed material for the production of polyglycerol esters, a nonionic surfactant commonly applied as an emulsifier in food products [69]. Polyglycerol is usually synthesized by polymerization using a base catalyst, but due to the presence of residual base catalyst and soap in the crude glycerol, it can be directly polymerized without catalyst addition [70].

Studies showed the polymerization of glycerol to produce polyglycerol can be performed using different types of catalysts, such as zeolites [71,72], acids [73], and oxides [74,75]. A study investigated the polymerization process of glycerol by applying basic and acidic catalysts. The polyglycerol obtained when sulfuric acid was used presented high molecular weight, and the NMR spectroscopy revealed that branched polymers were formed [76]. Other studies investigated the polymerization of crude glycerol by microwave irradiation to eliminate the use of catalysts [69] and heterogeneous catalysts to easier the separation process [77,78].

The use of glycerol as raw material for activated carbons was investigated by Gonçalves et al. [63], which used crude glycerol and H_2SO_4 as catalyst to obtain the polyglycerol, which was chemically activated using H_3PO_4 or $ZnCl_2$ as activating agents. The material produced showed morphology with large and irregular aggregates of smooth-surface, presence of micro and mesopores, and chemical mapping indicated the presence of C, O and, the one activated with H_3PO_4, also presented residual P. The results showed that the glycerin-activated carbons demonstrated potential application as supercapacitors and for the adsorption of organic contaminants from water, such as paracetamol and methylene blue dye. Medeiros et al. [79] also produced an activated carbon from glycerol to methylene blue dye adsorption application. The activated carbon adsorbent was elaborated by polymerization, carbonization, and activation of glycerol. The polymerization was performed with glycerol and sulfuric acid as catalyst, and the concentration of the catalyst was investigated. The resulting activated carbons had a specific area of $1630 \mathrm{~m}^2\mathrm{~g}^{-1}$, being essentially microporous, with a small amount of mesopores.

Cui and Atkinson [80] produced a tailored activated carbon from glycerol, which was applied to remove volatile organic compounds from a gas stream and Cr(VI) from an aqueous solution. The activated carbon was prepared via sulfuric or phosphoric acid-mediated polymerization and carbonization of glycerol followed by steam or CO_2 activation. The results showed the activated carbon prepared with H_3PO_4 is consistently more mesoporous than samples prepared with H_2SO_4, because of rudimentary pores generated in P-chars. Moreover, the activation

with steam produced an activated carbon more hydrophobic than the one activated with CO_2. The activated carbons prepared with sulfuric acid dehydration stand out for VOC adsorption, because of hydrophobicity and high micropore volume, but for aqueous adsorption, the activated carbons prepared with phosphoric acid dehydration are preferred, because of oxygen functionalities and high mesopore volume.

1.7   CDI cell architectures

In CDI, many studies mainly focused on the development of electrode materials, CDI applications, and energy efficiency understating, whereas a smaller fraction was dedicated to a better understanding of the influence of CDI architecture on desalination performance.

The most conventional design for CDI desalination cells is the flow-by cell (FBC) configuration, also called flow-between, where the electrolyte flows between the parallel electrodes. Basically, two electrodes are placed parallel to each other, in such a way that a small spacer channel is left in between, where the electrolyte flows, as shown in Figure 1.5(a). In this cell design, the electric field is perpendicular to the electrolyte flow. This classical architecture suffers from some limitations, such as insufficient utilization of the adsorption capacity of the electrode, infeasible for hydrophobic electrodes, and long spacer-to-electrode diffusion times [34].
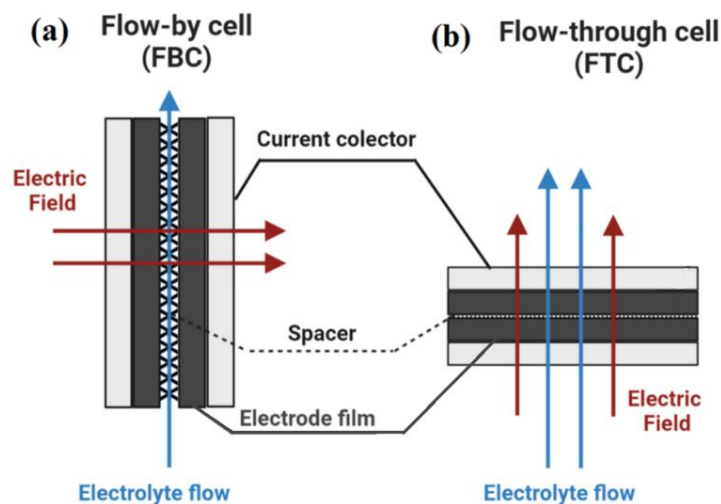
Figure 1.5. CDI cell architectures: Flow-by cell **(a)**, and flow-through **(b)** cells.

Another architecture is the flow-through cell (FTC), in which the electrolyte flows straight through the electrode's pores, from one electrode to another. This cell design is a promising approach because the enhanced mass transfer rate and the flow condition allows a faster system response than FBC, which needs time for the ion to diffuse from the spacer channel into the pores [2]. In this case, the electrolyte flows parallel to the applied electric field direction (Figure 1.5(b)). One advantage of this cell architecture is the possibility to eliminate the need for a separator layer that serves as the feed flow channel, thus the separator thickness to avoid short circuits may be minimized allowing more compact cells. Besides capacitive desalination, the flow-through technology has also been applied in other water treatments process as electrochemical membrane filtration, electrochemical disinfection, and energy production using microbial fuel cells [34].

Recent studies also evaluated a different CDI cell architecture, called flow-electrode capacitive desalination (FCDI) (Figure 1.6(a)), where instead of using static electrodes, a carbon slurry suspension is applied as the electrode in the CDI cell [81,82]. Generally, these suspensions are composed of active materials, conductive additives, and an aqueous electrolyte. High desalination efficiency and the possibility of continuous ion removal are the advantages of this architecture [83,84]. The high efficiency occurs due to the infinite uncharged carbon particles that are continuously introduced into the charging cell [19]. Some drawbacks related to FCDI are the energy cost for the electrode flow and the inefficient charge transfer between the current collectors and flowing particles [19].
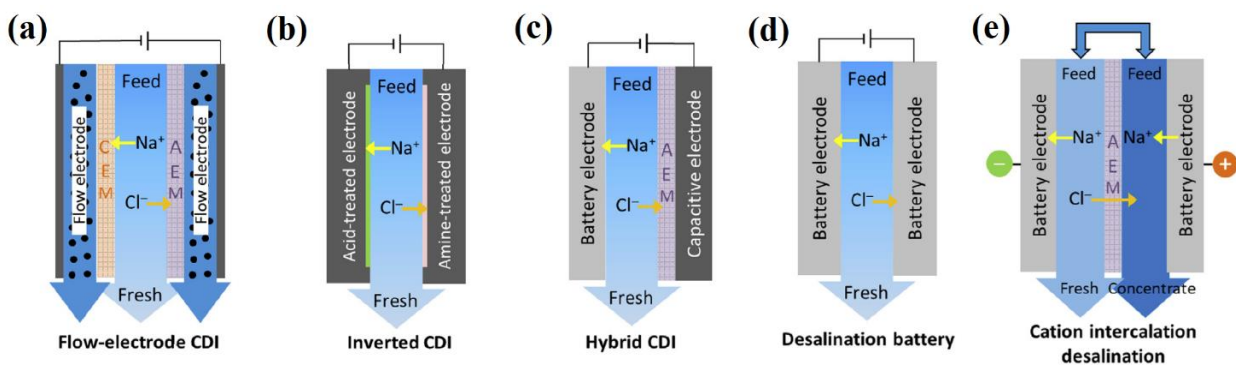
Figure 1.6. CDI cell architectures and cell configurations: **(a)** flow-electrode CDI, **(b)** inverted CDI, **(c)** hybrid CDI, **(d)** desalination battery, and **(e)** cation intercalation desalination [19].

Inverted capacitive deionization (i-CDI), shown in Figure 1.6(b), has same architecture of FBC, but with a different cell configuration, in which the anode with net negative surface charge and cathode with net positive surface charge are applied [30]. Basically, it is an inverted adsorption-desorption mechanism of the conventional CDI, whereby cell charging causes ion desorption and cell discharging results in ion electrosorption [85]. The application of i-CDI showed to be efficient to increase the electrode lifetime [43]. Hybrid capacitive deionization (HCDI) [86] and desalination battery [87] are other cell configurations present in literature, which have more complex mechanisms for ion removal since they involve Faradaic reactions involving reversible redox couples [19]. In the HCDI (Figure 1.6(c)), a capacitive electrode is used for anion adsorption and a battery electrode is used for cation uptake. In the battery electrode, the ions are not just adsorbed on the surface, but also intercalated into the crystal lattice structure via chemical bonds, providing higher specific capacity [88,89]. Unlike HCDI cell, the desalination battery cell shown in Figure 1.6(d) is formed by two different battery electrodes, in other words, Na^+ is intercalated in one electrode which is paired with a different electrode for Cl^- intercalation [90,91].

The cation intercalation desalination [92] is other cell architecture presented in literature, illustrated in Figure 1.6(e), also involve Faradaic reactions in the desalination mechanism. Since few materials are available for Cl^- intercalation, in the cation intercalation desalination, cation intercalation materials are employed as positive and negative, separated by an anion exchange membrane, in an architecture called "rocking-chair cell" [92,93].

Over the past decade, different CDI cell architectures, such as the ones described in this section, have been developed aiming to optimize electrosorption performance. However, a deep understanding of mass transfer in CDI cell architectures is still a remaining challenge to enhance desalination performance.

1.8   Objectives

CDI is a dynamic and complex process that depends on flow patterns and electric field direction in the CDI cell. Despite the significant progress achieved to date in the CDI area, the understanding of the fundamentals involved concerning these aspects is of paramount importance not only for the design of the electrochemical cell but also for process optimization. Moreover, the development of a low-cost effective electrode with electrode performance and stability over cycles

of electrosorption/desorption has been little explored in detail in the literature, which is still a challenge to overcome in order to make CDI feasible for large-scale applications.

The current thesis intends to fill these aforementioned gaps, so the main objective of this thesis was to optimize the CDI desalination by developing a cost-effective electrode, optimizing the operational conditions, improving the electrode stability, and developing a cell architecture to maximize the desalination and minimize the energy consumption. In order to achieve the main objective, the following specific objectives were established:

- obtain an activated carbon using polyglycerol synthesized with crude glycerol from the biodiesel production process, in order to apply this material to produce a sustainable low-cost electrode for CDI;

- understand the effects of cell potential and asymmetry on the electrode performance aiming for stable electrochemical desalination over desalination cycles;

- apply different electrode configurations (symmetric, asymmetric, MCDI, C-MCDI), operational conditions (potentiostatic, galvanostatic, batch mode, quasi single-pass mode), and cell architectures (FBC, FTC, PFC) aiming to optimize desalination performance in a CDI desalination process;

- understand the effects of mass transfer phenomena on the CDI performance and kinetics for different cell architectures in order to maximize the *OSR*;

- comprehend the influence of electrode thickness and the particle diameter used on electrode preparation on the CDI performance, correlating them to mass transfer phenomena.

1.9   Thesis Outline

In this thesis, activated carbons produced with polyglycerol from crude glycerol were employed as electrode material for capacitive deionization desalination. The main purposes of this work were to develop a sustainable low-cost activated carbon and understand the electrochemical and mass transfer phenomena affecting the capacitive deionization in order to improve the desalination performance to achieve electrode stability, fast kinetics, and high salt electrosorption capacity.

The results are presented in two chapters. Since crude glycerol is produced in large volumes in biodiesel plants, new applications for this by-product are attractive for sustainability purposes.

Considering this, in Chapter 2 is reported the development of a new activated carbon using as precursor the polymerized glycerol from biodiesel production without any purification process. The crude glycerol was firstly polymerized and the resulting polyglycerol was carbonized, activated, characterized and then employed as electrode for electrochemical desalination of brackish water. Additionally, the electrodes were tested regarding their stability and evaluated considering the shift of the potential of zero charge after 50 cycles of electrosorption/desorption. The effects of cell potential and cell configuration were investigated aiming to optimize the electrode performance and also considering the long-term stability. In order to further improve the desalination system, membrane CDI was tested using the polyglycerol activated carbon as positive and negative electrodes.

In Chapter 3, firstly, the electrode prepared using polymerized crude glycerol from biodiesel plants was optimized considering the technical and practical aspects from the engineering point of view. Therefore, a comparison between different cell architectures (flow-by and flow-through cells) and a proposed cell, called percolation flow cell (PFC), was carried out. To evaluate the CDI performance between the cell architectures the parameter optimized salt removal (*OSR*) was used, which consider simultaneously the effects of kinetics and adsorption capacity on the desalination process. The studied cell architectures considered hydrodynamics and electrochemical aspects in order to investigate the influence of the relative direction between flow velocity and electric fields (parallel or perpendicular) on the *SAC*, charge efficiency, and specific energy consumption. From the results using the flow-by and flow-through cells, the percolation cell was proposed and further investigated under more realistic conditions (single pass and galvanostatic modes). It is also worth mentioning that in this chapter it was investigated the influence of the electrode particle diameter and electrode thickness on the process performance, correlating them to the mass transfer phenomenon.

In Chapter 4, an overall conclusion about the main results obtained in this thesis is presented, along with suggestions for future works.

2   CHAPTER

USING CRUDE RESIDUAL GLYCEROL AS PRECURSOR OF SUSTAINABLE ACTIVATED CARBON ELECTRODES FOR CAPACITIVE DEIONIZATION DESALINATION

Capacitive deionization (CDI) is a promising electrochemical technology for water desalination that can contribute to reducing water scarcity. At the same time, appropriate routes for the disposal or reuse of liquid wastes are also a major current concern. Based on the water-waste nexus concept, this work demonstrates that crude glycerol from biodiesel plants can be successfully used to obtain a new sustainable activated carbon. After polymerization, the crude glycerol was carbonized and activated to obtain polyglycerol activated carbon (PGAC), which was employed as an electrode for CDI desalination of brackish water. Evaluation was made of the electrode performance and stability over cycles of electrosorption/desorption, using different cell configurations (symmetric, asymmetric, and membrane CDI) and cell voltages (E_{cell}). It was observed that maintaining the potential of zero charge of the negative and positive electrodes outside their working domains during the cycles enabled minimization of that part of the applied potential deviated to co-ion repulsion, consequently improving the salt adsorption capacity (SAC) and charge efficiency (Q_E). Furthermore, maintaining the potential of the positive electrode below the oxidation potential by controlling the applied E_{cell} could ensure electrode stability. The best desalination performance using the PGAC electrode was achieved using the membrane CDI configuration (at 1.6 V), resulting in stable SAC (~27.1 mg g-1) and Q_E (~100%) over 50 cycles. The low cost and high SAC and Q_E values suggested that the PGAC electrode could be considered a potential candidate for use in CDI desalination.

2.1   Introduction

The demand for freshwater has increased over the years, in order to meet the needs of agriculture, industry, and human consumption. Water insufficiency worldwide is expected to occur in the coming decades [1]. However, severe water scarcity is already a problem faced year-round by half a billion people [94]. For instance, water crises are suffered by populations in arid and semi-arid regions, where only brackish groundwater is usually available [7,95]. In this case, a strategy to provide freshwater is the development of new technologies for brackish water desalination, such as

capacitive deionization (CDI). This is a promising technology in which charged species are adsorbed in the electric double layer (EDL) formed when a pair of electrodes are polarized by applying an electric field. The mechanism is based on charging (electrosorption)/discharging (ion desorption) cycles. Once electrode saturation has been reached, a regeneration step consisting of short-circuiting or reversing the electric field is performed, in order to restore the ion sorption capacity.

Investigations of CDI performance have mainly used carbon-based electrodes, due to their suitable electrochemical and textural properties, since carbon materials have relatively high electric conductivity, high specific surface area, and tunable pore structure [96]. Carbon materials such as nitrogen-doped graphene [48], nanotubes [49], aerogel [50], and carbide-derived carbon [42] have been investigated as candidates for efficient CDI electrodes. Although these carbons are able to provide high electrosorption capacity, most of them are expensive or involve laborious syntheses, which imposes restrictions for large-scale applications [32,51,52].

The search for low-cost carbons for CDI electrodes should not only consider their effectiveness, but must also take sustainability aspects into account. These requirements can be met by preparing activated carbons from biowastes used as carbon precursors. Efforts have been made to obtain activated carbons from watermelon peel [53], jackfruit peel [57], waste coffee grounds [54], sugarcane bagasse fly ash [28], rice husk [55,56], lignin [33], and palm shell [58]. Overall, these electrodes have salt adsorption capacities (*SAC*) ranging from 3.3 to 22.8 mg g^{-1}, depending on the operational conditions. However, little attention has been paid to evaluating electrode performance and stability over cycles of electrosorption/desorption. In order to ensure robust desalination operation, it is essential to understand the stability of electrodes used for long-term desalination, as well as to develop new strategies to avoid carbon degradation and improve the *SAC*. Redox reactions occurring at the positive electrode can shift the potential of zero charge (E_{PZC}) to more positive potentials, due to modification of the functional groups on the carbon surface [29,43,45]. As a consequence, the carbon particles become more negatively charged and co-ion repulsion is increased, which negatively affects the charge efficiency and decreases the *SAC* over the cycles [33,97].

The present work demonstrates that a new sustainable activated carbon (AC) can be obtained from crude glycerol, a residual viscous liquid produced in large amounts as a byproduct of the biodiesel process. It is estimated that the production of 10 kg of biodiesel generates 1.0 kg of

glycerol [98]. The present search for renewable energy sources is expanding biodiesel production, so an oversupply of crude glycerol is expected [61]. For most industrial applications, the glycerol must be purified, since it contains impurities such as methanol, water, and fatty acids [61,70]. Double-vacuum distillation is usually employed for glycerol purification, but this process imposes high operational and capital costs. In this situation, a *sine qua non* condition to produce cost-competitive AC electrodes for CDI is the direct use of crude glycerol to obtain solid polyglycerol, which is then converted to the corresponding AC by carbonization and activation. The aim of this work was to develop a polyglycerol activated carbon (PGAC), using crude glycerol collected in biodiesel plants as the precursor. The as-synthesized PGACs were characterized and used to obtain electrodes for capacitive deionization. After electrochemical characterization, the electrodes were applied for brackish water desalination, using different cell configurations in order to achieve stability and high performance. The effect of the cell potential on process efficacy was evaluated using symmetric, asymmetric, and membrane (MCDI) setups, in order to maximize electrosorption capacity and avoid electrode oxidation. The desalination performance was evaluated in terms of electrosorption capacity, charge efficiency (Q_E), energy consumption (η), electrosorption/desorption rates, and stability during sequential cycles. This research shows the potential of polyglycerol activated carbon as a low-cost material for CDI electrodes applied for water desalination, besides providing a novel application for the crude glycerol.

2.2 Experimental

2.2.1 Materials

Crude glycerol (80% glycerol) was obtained from a glycerin bi-distillation plant located in Brotas, Brazil. Sulfuric acid (Sigma-Aldrich) was used as the catalyst for glycerol polymerization. KOH pellets (Sigma-Aldrich) were used for chemical activation to obtain the activated carbon from polyglycerol. HNO_3 (65%, Sigma-Aldrich) was used for the chemical modification of PGAC. Polyvinylidene fluoride (PVDF, Sigma-Aldrich) and n-methyl-pyrrolidone (99.5% NMP, Synth) were used for electrode preparation. NaCl (Synth) was used to prepare the electrolytes employed in the electrochemical characterization and desalination experiments. Deionized water was used to prepare all solutions.

2.2.2 Glycerol polymerization, PGAC synthesis, and electrode preparation

The polyglycerol was prepared according to an adaptation of the methodology reported by Medeiros and Lago [99]. The optimized synthesis conditions were established based on preliminary tests. Briefly, 20 mL of H_2SO_4 aqueous solution (5 mol%) were slowly added into a beaker containing the crude glycerol (100 g). The reaction was carried out under stirring for 7.5 h in a glycerin bath at 150 ℃, forming a viscous solution, which was then dried for 12 h at 150 ℃ in a conventional oven. The as-obtained polymer was labeled as PG. For comparison, another sample of polyglycerol was synthesized using analytical grade glycerol (Synth), following the same procedure, but conducting the polymerization reaction for 1 h and drying for 3 h.

The PG samples were carbonized at 600 ℃ for 1 h, under an atmosphere of N_2 (300 mL min^{-1}), in a tubular furnace (Lindberg Blue M, Thermo Scientific), applying a heating rate of 10 ℃ min^{-1}. The carbonized sample, labeled as PGC, was then activated by mixing it with KOH pellets in a ratio of 1:4 wt/wt (carbon:KOH) and leaving for 24 h. After this time, the sample was introduced into the tubular furnace and activated at 850 ℃ for 1.5 h, under an atmosphere of N_2 (150 mL min^{-1}), applying the same heating rate used in the carbonization step. The carbonized and activated conditions were based on the optimized conditions previously studied [27]. Subsequently, the sample was washed with 0.5 mol L^{-1} HCl and distilled water (60 ℃), until constant pH, and finally dried at 105 ℃ for 24 h. The as-synthesized polyglycerol activated carbon was labeled PGAC. The activated carbon from analytical grade glycerol, obtained following the same procedure was labeled as PGAC*.

For some samples, a chemical surface treatment using HNO_3 was performed with the aim of increasing the negative charge on the PGAC surface by introducing oxygen surface groups, in order to shift the E_{PZC} to more positive values [31]. This material was labeled as N-PGAC.

The electrodes were prepared by mixing 90 wt% of PGAC and 10 wt% of PVDF (binder) in NMP solvent. The slurry obtained was then spread onto a graphite foil substrate using a doctor blade machine and left to dry at 80 ℃, for 12 h, in a conventional oven. The thickness of the electroactive carbon film was ~400 µm.

2.2.3 Material and electrode characterization

Thermogravimetric analysis (TG) was performed using a TGA Q500 system (TA Instruments). The measurements were carried out by placing the sample in a platinum pan and heating to 900 ºC, at 10 ºC min^{-1}, under a flow of air (60 mL min^{-1}). The derivative TG (DTG) was calculated for identification of the combustion characteristics of the PG, PGC, and PGAC. Raman spectra were recorded using a Renishaw inVia microscope with a Nd-YAG laser (wavelength: 532 nm; grate: 600 x 50). The textural properties of the PGC, PGAC and PGAC electrode (PGACE) were characterized by N$_2$ adsorption-desorption, using an ASAP 2420 instrument (Micromeritics). The specific surface area was calculated from N$_2$ isotherms, using the Brunauer-Emmett-Teller equation (SSA_{BET}), considering relative pressure (P/P_0) between 0.05 and 0.20 (isotherm linear region). The pore size distribution (PSD) and total pore volume (V_T) were calculated by the 2D-NLDFT heterogeneous surface model, using SAIEUS software. The micropore volume (V_{mic}) was the volume of N$_2$ adsorbed by pores ≤2 nm, while the mesopore volume (V_{mes}) was calculated by the difference between V_T and V_{mic}. The average pore diameter (d_{50}) was determined considering the pore diameter for which the volume adsorbed was half of V_T.

The electrode wettability (hydrophobicity/hydrophilicity) was determined by contact angle measurement, according to the sessile drop method, in which a water droplet was deposited onto the surface of the carbon electrode. After 20 s, the angle between the line tangent to the liquid interface of the drop and the baseline was measured.

2.2.4 Electrochemical characterization

Cyclic voltammetry (CV), galvanostatic charge-discharge (GCD), and electrochemical impedance spectroscopy (EIS) were performed using an electrochemical workstation (Multi Autolab/M204) and a three-electrode cell filled with 1.0 mol L^{-1} NaCl. Ag/AgCl (saturated KCl) was used as the reference electrode. The PGAC electrodes were used as both working and counter electrodes.

The voltammograms were recorded with scanning of the potential between 0.1 and 0.6 V (*vs*. Ag/AgCl), at different scan rates (*v*): 1, 5, 10, 25, 50, 100, and 200 mV s^{-1}. The specific capacitance ($C_{S,CV}$) and total specific capacitance (C_{CV}), expressed in F per gram of the electroactive carbon film, were calculated using Eqs. (2.1) and (2.2), respectively. In these equations, I is the current (A), m is the mass of activated carbon in the working electrode (g), and E_1 (V) and E_2 (V)

are the lower and upper values of the potential window. GCD profiles were recorded at 0.1 A g^{-1} to evaluate the potential profile and the ohmic drop (IR_{drop}), considering the cut-off potentials of 0.6 and 0.1 V (*vs*. Ag/AgCl) for charging and discharging, respectively.

$$C_{S,CV} = \frac{I}{v\,m} \tag{2.1}$$

$$C_{CV} = \frac{\int_{E_1}^{E_2} I\,dV}{v\,m\,(E_2 - E_1)} \tag{2.2}$$

The EIS measurements were carried out applying frequencies ranging from 1 mHz to 100 kHz, 0.0 V *vs*. Ag/AgCl, and an alternating current amplitude of 10 mV. The EIS specific capacitance, $C_{S,EIS}$, was calculated using Eq. (2.3), where ω is the angular frequency and Z'' is the imaginary part of the impedance spectrum.

$$C_{S,EIS} = \frac{1}{|\omega\,Z''|} \tag{2.3}$$

The EIS measurements were also used to calculate the ohmic resistance (R_Ω), the charge-transfer resistance (R_{CT}), the admittance (A_0), the capacitance at the electrolyte/electrode interface (C_{INT}), and the capacitance inside the micropores (C_{EIS}). For estimation of these variables, the Nyquist plots were fitted to a modified Randles equivalent circuit. A constant phase element (CPE) was used to adjust the non-ideality of the semicircles, commonly assigned to surface roughness, surface inhomogeneities, and complexity of the double-layer structure present in this type of electrode. As shown in Eq. (2.4), the CPE impedance is related to the non-ideal capacitance (Q^0), the ideality factor (N) that ranges from 0 to 1, the imaginary number (j), and the angular frequency (ω) [100]. These variables were used to calculate the C_{INT} using Eq. (2.5).

$$CPE = \frac{1}{(j\omega)^N Q^0} \tag{2.4}$$

$$C_{INT} = \frac{(Q^0)^{\frac{1}{N}}(R_{CT})^{\frac{1-N}{N}}}{m} \tag{2.5}$$

The potential of zero charge (E_{PZC}) was determined using the EIS technique, but in this case, the spectra were recorded in 600 mg L^{-1} NaCl, at 10 mHz and 30 mV amplitude. A step potential (100 mV) was applied in a pre-established range of electrode potential. The capacitance at each potential was calculated using Eq. (2.3), with the values being normalized considering the lowest observed capacitance (C_{min}). The E_{PZC} was the potential that obtained the lowest capacitance (C/C_{min} = 1).

The anodic potential stability window (PSW) was determined by the method based on the Faradaic Fraction (R), proposed by Xu et al. [101]. Accordingly, cyclic voltammograms were recorded at 5 mV s^{-1}, in 1.0 mol L^{-1} NaCl, increasing the vertex by 50 mV. The scans started at 0.1 V (*vs*. Ag/AgCl), which was the equilibrium potential (E_{EQ}) determined previously, and finished at 1.2 V (*vs*. Ag/AgCl). The *R-value* was calculated by Eq. (2.6) for the anodic window (R_{pos}), where Q_{pos} and Q_{neg} correspond to the accumulated charge during the charging and discharging scans, respectively.

$$R_{pos} = \frac{Q_{pos}}{Q_{neg}} - 1 \qquad\qquad (2.6)$$

2.2.5   Electrosorption experiments

The electrosorption experiments were performed in a recirculating batch mode, using a desalination cell described elsewhere [102]. Briefly, the cell was composed of two acrylic plates attached to graphite current collectors. The PGAC, N-PGAC, or PGAC* electrode (2.5 cm x 2.5 cm) was positioned contacting the graphite and separated by two plastic meshes, which provided the gap necessary to avoid short circuit and allow the electrolyte flow. The cell was assembled using nuts and bolts, with rubber gaskets providing tight sealing.

For the desalination assays, 25 mL of 600 mg L^{-1} NaCl solution was recirculated through the CDI cell and electrolyte reservoir at a constant flow rate (26 mL min^{-1}), using a peristaltic pump (Masterflex L/S, Cole-Parmer). A potentiostat (PGStat 204, Autolab) was used to apply constant cell potentials during the electrosorption (1.1, 1.2, 1.4, or 1.6 V) and desorption (0.0 V) steps. The desalination was carried out over 50 electrosorption/desorption cycles, with half-cycles of 15 min, to ensure the steady-state condition and to enable evaluation of electrode stability. The conductivity, pH, and temperature were continuously monitored in the outlet stream of the CDI cell (Seven Excellence instrument, Mettler-Toledo). The conductivity value was corrected considering the pH and temperature fluctuations during the experiment, according to the methodology described by Lee et al. [103].

Firstly, the positive and negative electrodes were arranged in a symmetric configuration, using the PGAC carbon (so the two electrodes had the same E_{PZC}, mass of carbon, and thickness). In order to investigate the effect of co-ion repulsion, the asymmetric configuration was further

explored by using electrodes with different E_{PZC} values. Accordingly, based on the E_{PZC} determined previously, the PGAC and N-PGAC were used as the positive and negative electrodes, respectively.

With the aim of improving the removal capacity and charge efficiency, the desalination was also investigated using a membrane cell (MCDI). Accordingly, cationic (CMI-7000S) and anionic (AMI-7001S) membranes (Membranes International Inc.) were placed adjacent to the negative and positive electrodes, respectively. An additional experiment was carried out using solely the cation exchange membrane (C-MCDI), in order to determine whether it was sufficient to avoid co-ion repulsion at the negative electrode.

The desalination performance was evaluated in terms of salt adsorption capacity (SAC), charge efficiency (Q_E, no leakage current discount), and specific energy consumption (η), calculated using Eqs. (2.7), (2.8), and (2.9), respectively. In these equations, C_0 is the initial salt concentration (mg L^{-1}), C_t is the salt concentration (mg L^{-1}) at time t (s), V is the electrolyte volume (L), m_E is the total mass of the active material in both electrodes (g), z is the ion valence, F is the Faraday constant (96,485 C mol^{-1}), I is the current (A), M_{NaCl} is the molecular weight of NaCl (58,440 mg mol^{-1}), E_{cell} is the cell potential in the electrosorption step (V), and m_{rem} is the mass of ions removed from the solution (mg).

$$SAC = \frac{(C_0 - C_t) \cdot V}{m_E} \tag{2.7}$$

$$Q_E = 100 \frac{z.F.V.(C_0 - C_t)}{M_{NaCl} \int I dt} \tag{2.8}$$

$$\eta = \frac{E_{cell} \int I dt}{m_{rem}} \tag{2.9}$$

In order to evaluate the overall performance and effectively compare the different electrode configurations, the optimized salt removal (OSR) approach proposed by Zornitta and Ruotolo [41] was also applied. This performance metric allows a simultaneous analysis of the electrosorption capacity and adsorption/desorption kinetics. Such analysis is crucial for electrode evaluation, since the electrosorption and desorption times affect the number of cycles performed in a given operational time, thus influencing water productivity. The OSR value represents the amount of salt removed per gram of electrode material in a specified operational time (mg g^{-1} day^{-1}).

2.3   Results and discussion

The polymerization yield of polyglycerol was 52.5%, after elimination of the volatile compounds and impurities commonly found in the crude glycerol. After carbonization, the yield dropped to 16.4% of carbon, due to the release of volatile compounds from the polyglycerol at temperatures up to 600 ℃. After activation of the carbonized sample, the yield was 20.9%, which was similar to the yields observed for other materials carbonized at similar temperatures [27,56]. Considering the overall yield, it was possible to produce 34 mg of PGAC per g of PG. These results are summarized in Table 2.1.

Table 2.1 Mass yields: polymerization (Y_P), carbonization (Y_C), activation (Y_A), and overall (Y_O).

Y_P (%)[a]	Y_C (%)[b]	Y_A (%)[c]	Y_O (%)[d]
52.5 ± 1.2	16.4 ± 2.6	20.9 ± 2.0	3.4 ± 0.3

Note: [a] (g PG/g crude glycerol)*100; [b] (g PGC/g PG)*100; [c] (g PGCA/g PGC)*100; [d] (g PGCA/g PG)*100.

2.3.1 Material characterization

The TG and DTG profiles of PG, PGC, and PGAC are shown in Figures 2.1(a) and 2.1(b), respectively. The PG mass loss (~3.8%) from room temperature to 120 ℃, represented by the shallow peak in the DTG, was attributed to physically adsorbed water. As the temperature increased, substantial mass loss occurred between 180 and 550 ℃, which was similar to the profile observed by Zhao et al. [104]. For PG, the mass loss occurred in three thermal events (Figure 2.1(b)): 1) at 262 ℃, decomposition of carboxylic groups, probably originated from the free fatty acid impurities present in crude glycerol [70,105]; 2) at 416 ℃, thermal decomposition of unconverted glycerides, which are also impurities present in crude glycerol [61,106]; and 3) at 511 ℃, release of hydroxyls from the carbonized polyglycerol chains and carbon decomposition involving breaking of C–C bonds [107]. It is noteworthy that the thermogram of the carbonized sample (PGC) only presented mass loss between 400 and 600 ℃, providing further evidence that the mass loss in this temperature range was due to carbon decomposition.

For PGAC, a slight mass loss was observed above 210 ℃ (Figure 2.1(a)), which could be attributed to the decomposition of surface oxygen groups (SOG) generated during the activation step with KOH [32]. In contrast, PGC showed no mass loss up to 400 ℃, indicating the absence of

SOG, since this material underwent a carbonization step at 600 ºC, under a nitrogen atmosphere, which caused SOG decomposition [105,108]. Finally, the TG results showed sharp mass losses in the ranges 400-600 ºC and 500-700 ºC for PGC and PGAC, respectively, which were assigned to carbon combustion reactions involving breaking of C–C bonds [109,110]. The mass remaining after 700 ºC corresponded to the fraction of ash in the samples, with values of 10.6, 41.6, and 44.9% for PG, PGC, and PGAC, respectively.
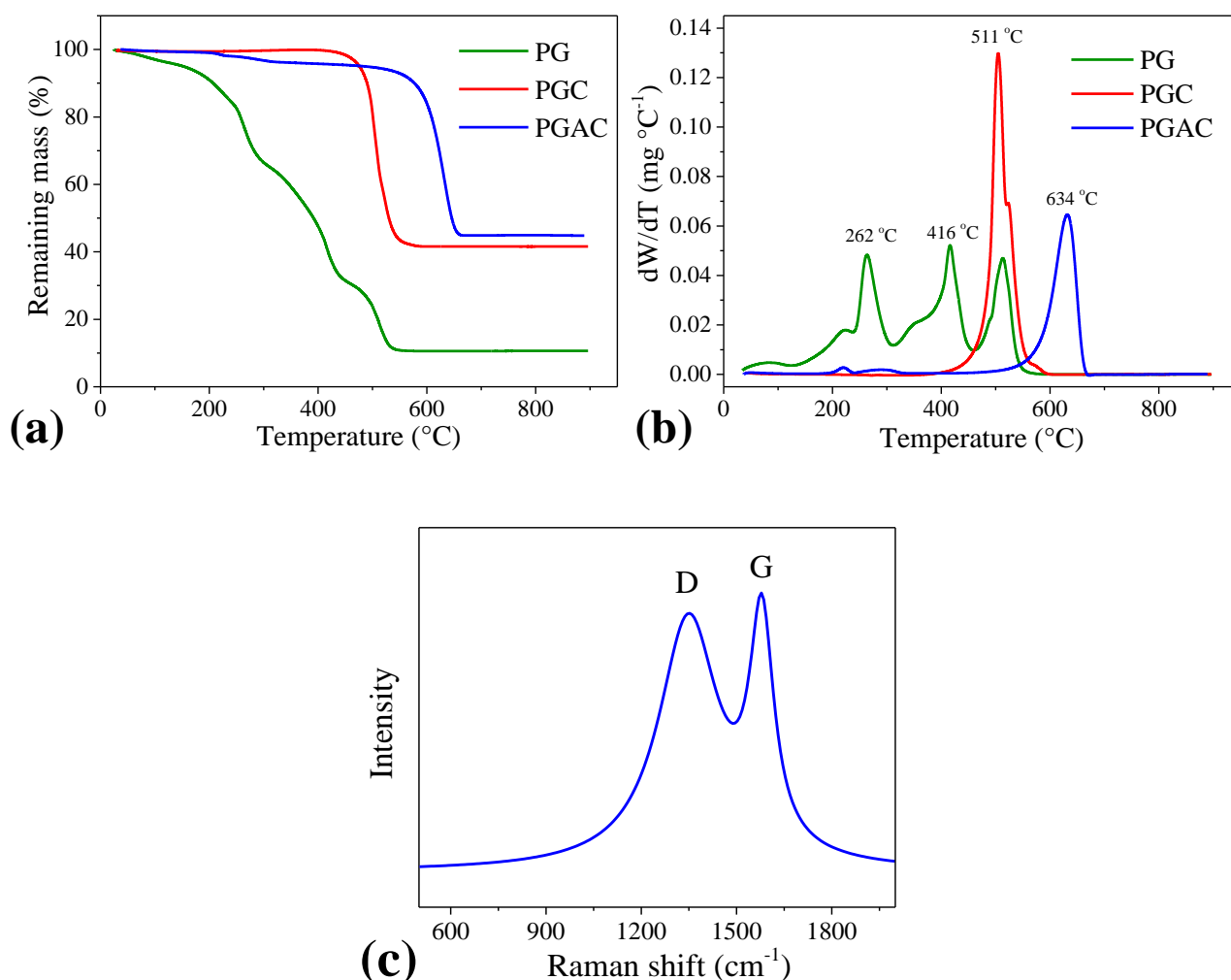
Figure 2.1. **(a)** TG and **(b)** DTG curves for PG, PGC, and PGAC, obtained under an air atmosphere; **(c)** Raman spectrum for PGAC.

The Raman spectrum of the PGAC is presented in Figure 2.1(c). The D mode at 1349 cm^{-1} indicated a disordered carbon structure, while the G mode at 1580 cm^{-1} was related to the presence of sp^2-hybridized C=C in the graphitic layers. The Raman peak intensity ratio (I_D/I_G) is commonly used to estimate the degree of defects in graphitic materials [111,112]. The I_D/I_G value for PGAC was ~0.85, revealing that the carbon layer was primarily composed of graphitic structures that favor

electronic conductivity [113]. The disorder could be ascribed to the oxygen surface groups produced by the activation reactions of KOH with carbon, as well as the turbostratic structure promoted by carbonization at temperatures ≤600 ºC [27].

The N_2 adsorption-desorption isotherms were used to determine the textural properties of PGC, PGAC, and PGAC electrode (PGACE) (Figure 2.2(a), Table 2.2.) According to the IUPAC classification, PGC, PGAC, and PGACE presented type II isotherms with H4-type hysteresis loop, indicating the existence of mesopores, typical of micro/mesoporous carbons [27,114]. As expected, the isotherms showed that the volume adsorbed by PGC was low and increased significantly after activation. Likewise, the specific surface area (SSA) was improved from 116 to 1684 m^2 g^{-1}, confirming the effectiveness of the activation step to increase SSA and pore volume. The pore size distribution (Figure 2.2(b)) revealed that the polyglycerol precursor led to carbons composed of micropores and a large percentage of mesopores (Table 2.2). A high percentage of mesopores is desirable, since they facilitate the access of ions to the micropores, consequently improving the kinetics. It is important to highlight that after the electrode preparation step, the SSA of the PGACE decreased by ~20%, due to pore clogging by the binder [102].
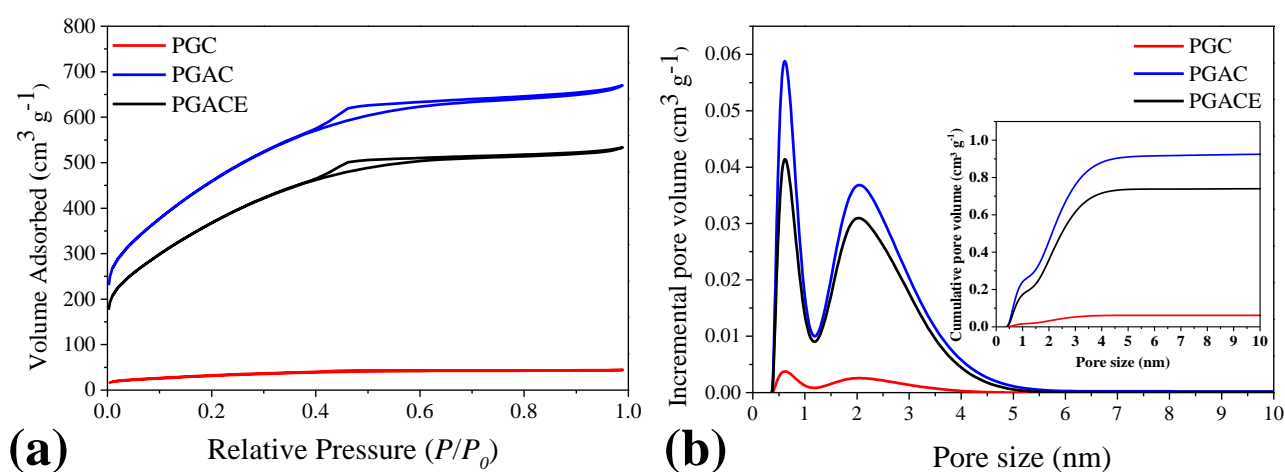
Figure 2.2 (a) Nitrogen adsorption-desorption isotherms and **(b)** pore size distributions (inset: cumulative pore volumes) for PGC, PGAC, and the PGAC electrode.

Table 2.2 Textural properties of polyglycerol after carbonization, activation, and electrode preparation.

	SSA_{BET} (m^2 g^{-1})	V_T (cm^3 g^{-1})	V_{mic} (cm^3 g^{-1})	V_{mes} (cm^3 g^{-1})	$\%V_{mes}$	d_{50} (nm)
PGC	116	0.06	0.03	0.03	50.2	1.98
PGAC	1684	0.95	0.45	0.50	52.7	2.02
PGACE	1355	0.76	0.35	0.40	53.4	2.07

PGACE: polyglycerol activated carbon electrode; SSA_{BET}: specific surface area; V_T: total volume of pores; V_{mic}: volume of micropores; V_{mes}: volume of mesopores; $\%V_{mes}$: percentage of mesopores; d_{50}: average pore size.

2.3.2 Electrochemical characterizations

Cyclic voltammetry characterization at different scan rates was carried out to investigate the electrode capacitance, resistivity, and mass transfer effects. As shown in Figure 2.3(a), the voltammograms for the PGAC electrode presented a quasi-rectangular shape at 1 mV s^{-1}, indicating its capacitive and conductive behavior. When the scan rate was increased to 5 and 10 mV s^{-1}, the voltammograms showed a leaf-shaped curve, related to increased resistivity. The total specific capacitance decreased by ~52% when the scan rate was increased from 1 to 10 mV s^{-1}. The same trend can be seen in Figure 2.3(b), which compares the C_{CV} decay of the electrode before and after 50 cycles of electrosorption (1.2 V)/desorption (0.0 V). As the scan rate decreased, the capacitance increased, indicating that at slow scan rates, the time was sufficient to allow the migration of ions into the inner pores, favoring complete charging of the EDL [115]. Contrary to the observations of Lado et al. [28], although the PGAC electrode presented a remarkable quantity of mesopores (53.4%), facilitating ion migration, this condition was not sufficient to prevent a rapid capacitance decrease (Figure 2.3(b)). Similar capacitance decay was observed for the electrode after use in desalination, except at 1 mV s^{-1} (Table 2.3). These features suggested that rather than mass transfer, charging resistance was the main factor affecting the performance of the PGAC electrode, which was further investigated using EIS analysis (discussed further).
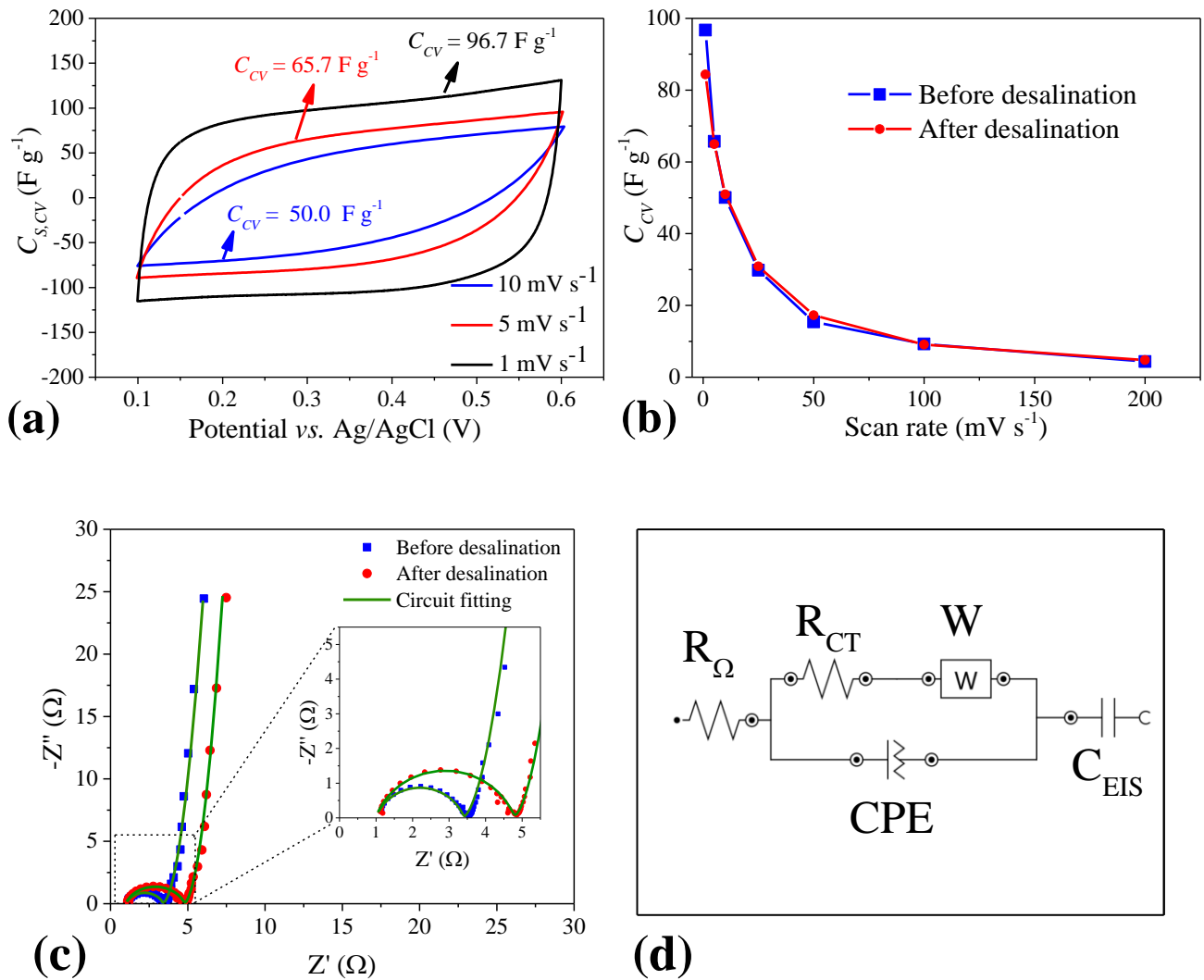
Figure 2.3 (a) Specific capacitance from cyclic voltammograms recorded at different scan rates, before desalination; **(b)** Total specific capacitance, as a function of scan rate, before and after desalination applying 1.2 V; **(c)** Nyquist plots before and after desalination applying 1.2 V; **(d)** Modified Randle equivalent circuit. Working and counter electrodes: PGAC. Electrolyte: 1 mol L^{-1} NaCl.

Table 2.3 Capacitance determined using the CV and EIS parameters obtained from fitting the Nyquist plots with a modified Randle equivalent circuit, for the PGAC electrode.

	Before desalination	After desalination (1.2 V)
C_{CV} (F g^{-1}) *	96.7	84.3
C_{EIS} (F g^{-1})	117	114
C_{INT} (mF g^{-1})	0.44	0.70
R_{Ω} (Ω)	1.00	0.99
R_{CT} (Ω)	2.40	3.79
A_0 (S s$^{1/2}$)	2.38	2.47

*At a scan rate of 1 mV s^{-1}.

Additional characterization of the electrochemical behavior of the PGAC electrode was performed using galvanostatic charge-discharge (Figure 2.4). The GCD curves presented an almost symmetric triangular shape, reinforcing the reversibility and capacitive behavior of the electrode. In addition, the GCD profiles showed an increase of IR_{drop} after desalination. This ohmic drop was a combination of resistances in series, including solution resistance, contact resistance, and ion diffusion resistance. The IR_{drop} enhancement could be ascribed to the emergence of resistive SOG on the positive electrode. It is well known that the presence of polar groups can improve electrode wettability. Hence, the decrease of the contact angle (Figure 2.5) from 76º to 0º after desalination also suggested that the electrode became more hydrophilic, due to the increase of SOG generated during the desalination cycles [32,52].
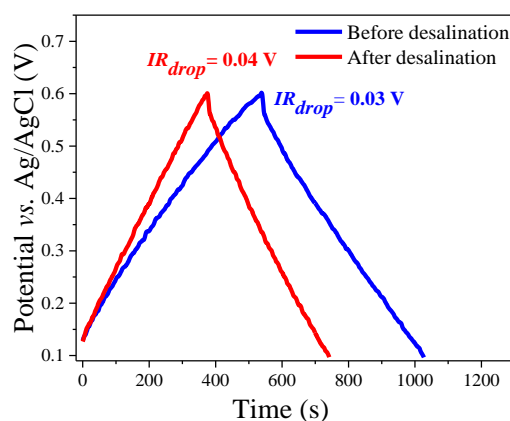
Figure 2.4 GCD profiles obtained at 0.1 A g^{-1}. Electrolyte: 1 mol L^{-1} NaCl.
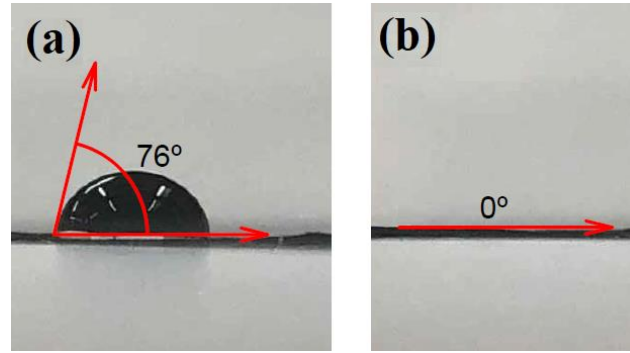
Figure 2.5 Contact angles before **(a)** and after **(b)** desalination at 1.2 V.
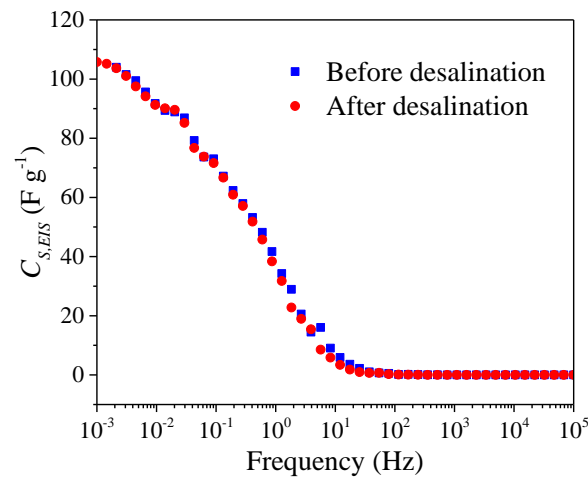
Figure 2.6 Specific capacitance determined from EIS ($C_{S,EIS}$) as a function of frequency. Electrolyte: 1 mol L^{-1} NaCl.

EIS was performed to investigate the capacitance and series resistances of the PGAC electrodes. The Nyquist plots (Figure 2.3(c)) were typical of electrochemical supercapacitors, with the semi-circle at high frequencies representing the charge-transfer region, while the linear region at low frequencies was related to the mass-transfer region [57,116]. In addition, the plot of $C_{S,EIS}$ as a function of frequency (Figure 2.6) showed that high capacitance was obtained at low frequencies, since this condition increased the time available for the ions to migrate to the micropores and be stored in the EDL. It is also noteworthy that the EIS analysis showed similar $C_{S,EIS}$ values before and after desalination, independent of the frequency.

The modified Randle equivalent circuit (Figure 2.3(d)) effectively fitted the Nyquist plots, enabling determination of the values of the resistances (R_Ω and R_{CT}), admittance (A_0), and capacitances (C_{INT} and C_{EIS}), shown in Table 2.4. Considering that R_Ω is related to the contact (current collector) and electrolyte resistances, it can be concluded that the desalination process did

not affect R_Ω during the cycles. On the other hand, R_{CT} is affected by the intrinsic properties of the carbon electrode, such as surface chemistry and polarization resistance. The R_{CT} of PGAC was high, compared to the values reported for other electrodes used for CDI (Table 2.4), which reinforced that the sharp capacitance decrease observed in Figure 2.3(b) was not related to mesoporosity, but rather to charging resistances that could be ascribed to SOG. These, in turn, affected the electrode polarization, as demonstrated by Lado et al. [117].

Table 2.4 Values of R_{CT} and A_0 reported in the CDI literature.

Electrode	R_{CT} (Ω)	A_0 (S s$^{1/2}$ cm^{-2})	Reference
AC600	0.37	-	Silva et al. [56]
AWCG700	0.83	-	Qian et al. [54]
sPAC/PTS	0.66	0.74	Barcelos et al. [45]
MMM-3DG	0.34	-	Kang et al. [118]
PCT$_{1.75}$-N	2.42	0.23	Zhao et al. [119]
PCT$_{1.5}$-N	5.10	0.18	Zhao et al. [119]
PGAC	2.40	0.38	This work

Note: AC600: rice husk activated carbon carbonized at 600 ºC; AWCG700: waste coffee grounds activated at 700 ºC; sPAC/PTS: activated carbon derived from p-toluenesulfonate chemically modified by silanization; MMM-3DG: micro-meso-macroporous three-dimensional graphene; PCT$_{1.75}$-N: nitrogen-doped porous carbon tubes composite with 1.75:1 mass ratio of Zn(Ac)$_2$·2H$_2$O to polyacrylonitrile; PCT$_{1.5}$-N: nitrogen-doped porous carbon tubes composite with 1.5:1 mass ratio of Zn(Ac)$_2$·2H$_2$O to polyacrylonitrile.

After desalination, R_{CT} increased by ~58% (Table 2.3), suggesting that carbon oxidation occurred during the desalination, generating more SOG. Confirmation of this hypothesis employed analysis of E_{PZC}. As shown in Figure 2.7(a), there was a shift of E_{PZC} to positive potentials after desalination, indicating that the surface became more negative, attributed to the presence of more SOG, as reported elsewhere [29,120]. These results indicated that further efforts are required to decrease the R_{CT} of the PGAC electrodes, in order to achieve faster electrosorption kinetics.

The admittance, which is the inverse of the Warburg element, describes the effect of ion diffusion in the inner pores. There was only a slight increase of A_0 after desalination, indicating that

the textural properties of the electrode affecting the mass transfer did not change over the cycles. The PGAC electrode presented A_0 values similar to those for other electrodes reported in the literature (Table 2.4).
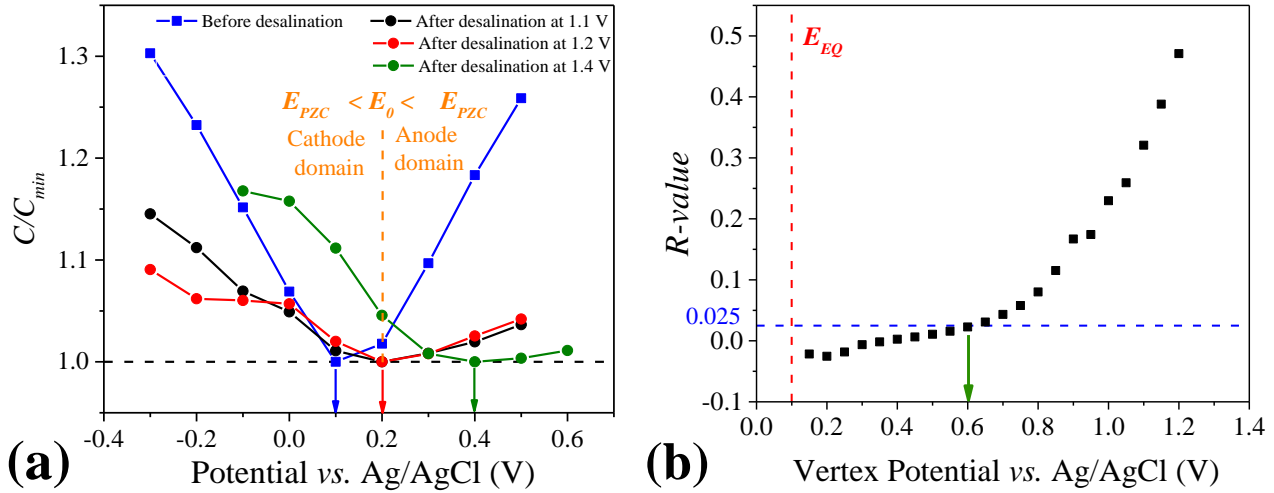
Figure 2.7. (a) Normalized capacitance, according to electrode potential, for the PGAC anode electrode. **(b)** *R-value*, according to vertex potential, in the anodic regime. E_{EQ}: equilibrium potential.

In order to ensure an energy-efficient process, CDI desalination is usually performed under potentiostatic conditions, typically applying 1.2 V to avoid water electrolysis [121]. However, even at lower cell potentials, unexpected electrode degradation can occur [33,120], since each carbon electrode has its own electrochemical stability potential limit. Therefore, determination of the electrochemical potential stability window (PSW) is essential for elucidation of the optimum working potential at which the electrode presents reversible behavior, avoiding electrode degradation and ensuring its stable performance during desalination. Hence, the PSW for the PGAC electrode was investigated considering the anodic regime, which is responsible for the main reactions affecting E_{PZC} and stability [45]. Firstly, cyclic voltammograms were recorded, at 5 mV s^{-1}, from the equilibrium potential (0.1 V *vs.* Ag/AgCl) up to different vertex potentials (Figure 2.8). The *R-value*s were then calculated for each potential (Figure 2.7(b)). The anodic potential limit (E_{pw}^{+}) adopted for the PGAC electrode was 0.6 V *vs.* Ag/AgCl, considering an *R-value* of 0.025 as a stability criterion, based on preliminary tests. In order to avoid degradation reactions caused by carbon electrode oxidation and other parasitic Faradaic reactions, the positive electrode potential should not exceed the E_{pw}^{+} value [120].
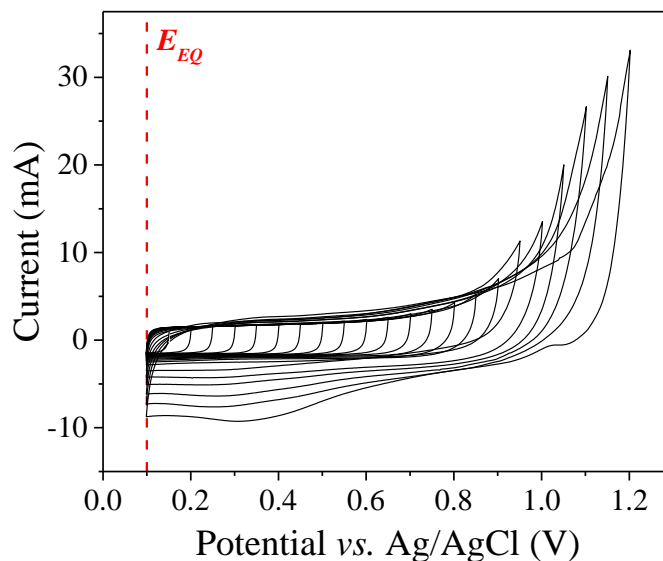
Figure 2.8. Cyclic voltammograms recorded at 5 mV s^{-1} in the anodic regime for the PGAC electrode. Electrolyte: 1 mol L^{-1} NaCl. E_{EQ}: equilibrium potential.

2.3.3 Desalination performance

The effects of different E_{cell} values and cell configurations on the electrochemical desalination performance of the PGAC electrode were investigated in desalination experiments applying different cell potentials and cell configurations. Figures 2.9(a), 2.9(c), and 2.9(d) show the desalination performance in terms of *SAC* and charge efficiency over 50 cycles. For the symmetric configuration (Figure 2.9(a)), the PGAC electrode presented stable desalination performance, maintaining the average *SAC* values constant throughout the cycles at 1.1 V (~10.8 mg g^{-1}) and 1.2 V (~14.2 mg g^{-1}). The higher *SAC* value obtained at 1.2 V could be attributed to greater electrostatic interaction, which enhanced the electrosorption of counterions. It is also notable that higher stability was obtained using the symmetric PGAC configuration, compared to the other electrodes that did not remain stable at 1.2 V [28,33]. Nevertheless, although *SAC* increased by ~31% when E_{cell} was increased from 1.1 V to 1.2 V, the specific energy consumption also increased by ~11% (Table 2.5). At 1.4 V, the *SAC* dropped by ~45% over the 50 cycles, resulting in the highest value of η, which could be ascribed to parasitic reactions [29,45]. In order to investigate this outcome, the electrode potentials were measured during the cycles.
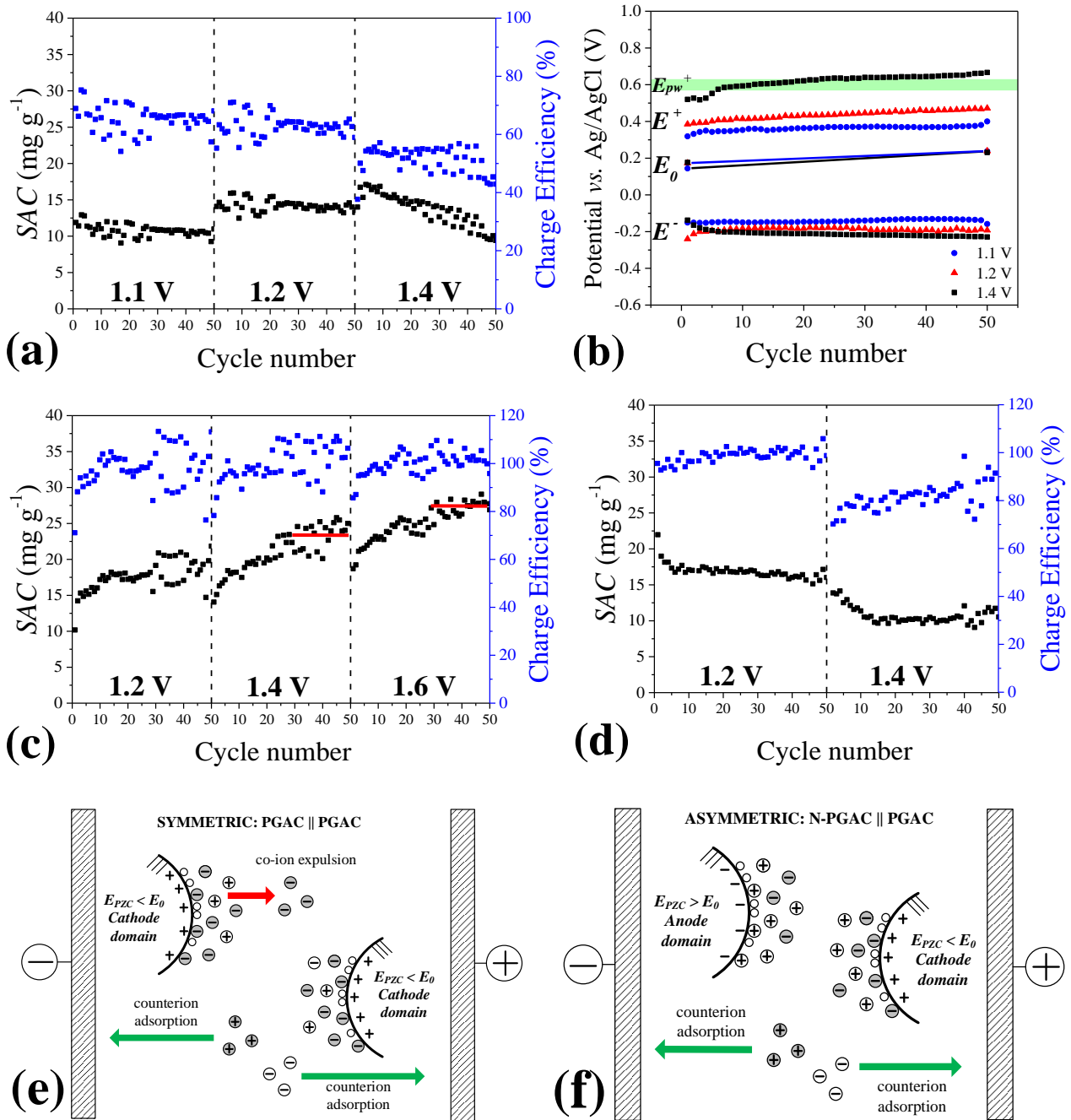
Figure 2.9. *SAC* and charge efficiency for the symmetric **(a)**, MCDI **(c),** and C-MCDI **(d)** configurations. Electrode potential profiles over the cycles for the symmetric configuration **(b)**. *E⁻* and *E⁺* indicate the potential in the cathode and anode, respectively. *E₀* is the short-circuit potential. *Epw⁺* is the anodic potential stability limit (standard deviation of 5%). Schematic representation of co-ion repulsion and counterion adsorption for symmetric (**e**) and asymmetric (**f**) configurations.

Table 2.5 Average values of the salt adsorption capacity (*SAC*), charge efficiency (*QE*), and specific energy consumption (*η*) for the desalination processes.

Electrode configurations	E_{cell} (V)	SAC (mg g^{-1})	Q_E (%)	η (J mg^{-1})
Symmetric	1.1	10.8 ± 0.8	65.4 ± 4.3	2.8 ± 0.2
Symmetric	1.2	14.2 ± 0.8	62.9 ± 3.6	3.1 ± 0.2
Symmetric	1.4	13.7 ± 2.1	51.2 ± 4.4	4.6 ± 0.4
Asymmetric	1.2	11.5 ± 0.5	88.4 ± 6.9	2.2 ± 0.2
MCDI	1.2	17.6 ± 2.1	97.9 ± 8.4	2.0 ± 0.2
MCDI	1.4	$23.4 \pm 1.8^{*}$	$102.9 \pm 7.2^{*}$	$2.3 \pm 0.2^{*}$
MCDI	1.6	$27.1 \pm 1.0^{*}$	$102.2 \pm 3.4^{*}$	$2.6 \pm 0.1^{*}$
C-MCDI	1.2	16.8 ± 0.7	98.9 ± 2.7	2.0 ± 0.1
C-MCDI	1.4	10.8 ± 1.1	81.6 ± 5.5	2.8 ± 0.2

*Average value considering the steady state.

The electrode potential profiles for the three different values of E_{cell} investigated for the symmetric configuration are displayed in Figure 2.9(b). The analysis of these profiles, considering the previously determined anodic stability window, revealed that at 1.4 V, the symmetric PGAC electrodes operated at potentials above the stability limit ($E^{+} > E_{pw}^{+}$). It is known that potentials beyond the stability window can result in oxidation of the carbon surface, forming surface oxygen groups with negative charge that can shift E_{PZC} to more positive values [120,121]. In order to address this issue, the E_{PZC} values were measured before and after the 50 desalination cycles. As shown in Table 2.6, at 1.4 V there was an E_{PZC} shift of 0.3 V *vs.* Ag/AgCl (from 0.1 to 0.4 V *vs.* Ag/AgCl) for the anode, confirming that the surface charge of the PGAC became more negative. As a consequence, as shown in Figure 2.7(a), the E_{PZC} moved from the cathode to the anode domain in which part of the applied potential was diverted for co-ion repulsion [29,33], causing the *SAC* to decrease. Accordingly, the worst values of Q_E and η were observed at 1.4 V (Table 2.5), due to the deviation of part of the applied potential intended for electrosorption to (i) oxidation reactions and

(ii) co-ion repulsion. In contrast, applying 1.1 or 1.2 V, the potential shift was not sufficient to displace the E_{PZC} to the anode domain, so the *SAC* remained stable. It is also notable that for the negative electrode, no E_{PZC} displacement was observed (Figure 2.10), so its value remained in the cathode domain. Hence, the stability of the PGAC was dictated by the positive electrode behavior.

Table 2.6 Potential of zero charge (E_{PZC}) and E_{PZC} shifts obtained for the PGAC anode electrodes before and after the desalination cycles.

Electrode configurations	E_{cell} (V)	$E_{PZC,0}$ (V *vs.* Ag/AgCl)[a]	$E_{PZC,50c}$ (V *vs.* Ag/AgCl)[b]	E_{PZC} shift (V *vs.* Ag/AgCl)
Symmetric	1.1	0.1	0.2	0.1
Symmetric	1.2	0.1	0.2	0.1
Symmetric	1.4	0.1	0.4	0.3
Asymmetric	1.2	0.1	0.2	0.1
MCDI	1.6	0.1	0.1	0.0
C-MCDI	1.4	0.1	0.3	0.2

[a] $E_{PZC,0}$: E_{PZC} of the pristine electrodes; [b] $E_{PZC,50c}$: E_{PZC} after 50 electrosorption/desorption cycles; $E_0 \sim 0.2$ V *vs.* Ag/AgCl.
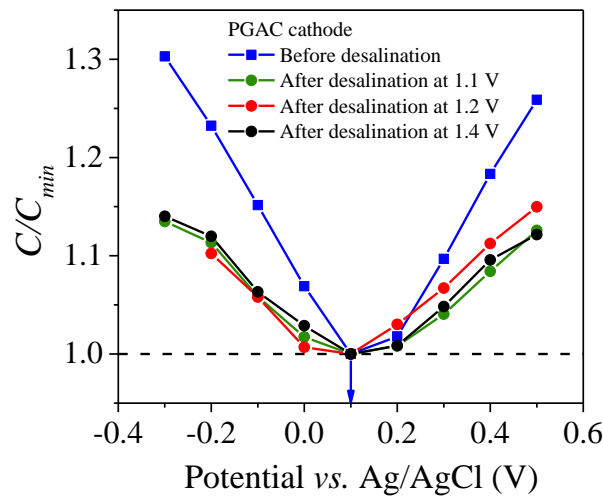
Figure 2.10. E_{PZC} values for the cathode before and after the desalination process using the symmetric configuration with PGAC electrodes.

In an attempt to increase the charge efficiency of the CDI system, an asymmetric configuration was proposed, based on the E_{PZC} values, in order to obtain a better arrangement where

the electrodes could operate in their respective working domains, avoiding co-ion repulsion, as shown in Figs. 2.9(e) and 2.9(f) [29,33]. The electrodes with E_{PZC} values outside their working domains corresponded to the best configuration, due to the minimization of co-ion repulsion and improvement of the charge efficiency. Since the E_{PZC} of PGAC was 0.1 V *vs.* Ag/AgCl, this electrode was in the cathode working domain (Figure 2.7(a)), given that E_0 was ~0.2 V *vs.* Ag/AgCl. In the symmetric configuration, even at 1.1 or 1.2 V, co-ion repulsion was expected at the negative electrode (Figure 2.9(e)), which was confirmed by the low values of Q_E (Table 2.5). Therefore, for the asymmetric configuration, PGAC was chosen as the positive electrode. In order to avoid co-ion repulsion at the cathode, by creating negative surface charges, the PGAC was submitted to a surface treatment using HNO_3, with the aim of shifting the E_{PZC} outside the cathode domain. Accordingly, the E_{PZC} of this electrode, labeled as N-PGAC, was 0.3 V *vs.* Ag/AgCl (Figure 2.11), demonstrating the effectiveness of this chemical treatment for shifting the E_{PZC} to a more positive value, due to the introduction of negative oxygen functional groups [29,121]. Therefore, the PGAC and N-PGAC electrodes were used as anode and cathode, respectively, so both values of E_{PZC} were outside their respective electrode domains (Figure 2.11), enabling the applied potential to be mostly used for counterion electrosorption, according to the scheme shown in Figure 2.9(f).
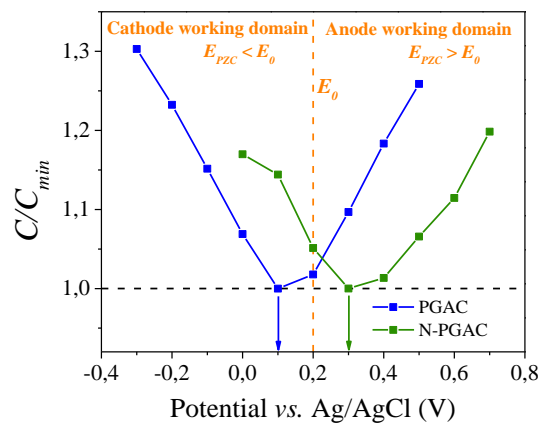
Figure 2.11. E_{PZC} values for the electrodes PGAC and PGAC treated with nitric acid (N-PGAC).

When the asymmetric configuration (Figure 2.12(a)) was used in the desalination cycles, there was a substantial increase of Q_E from 62.9 to 88.4%, together with a decrease of η (29%), compared to the symmetric configuration at 1.2 V (Table 2.5). This confirmed the effectiveness of using asymmetry to minimize the co-ion repulsion and increase the portion of the potential effectively applied for counterion adsorption. However, the *SAC* decreased by 19%, compared to

the symmetric configuration, which could be explained by reduction of the specific surface area after the HNO$_3$ treatment, as reported previously by Wu et al. [122]. The asymmetric electrodes presented stability over the cycles, with the E^+ values remaining below E_{pw}^+ (Figure 2.12(b)). The anode presented an E_{PZC} shift of 0.1 V *vs.* Ag/AgCl (Figure 2.12(c)), but the E_{PZC} was not displaced to the anode domain, while the E_{PZC} of the N-PGAC cathode remained constant (Figure 2.12(d)).
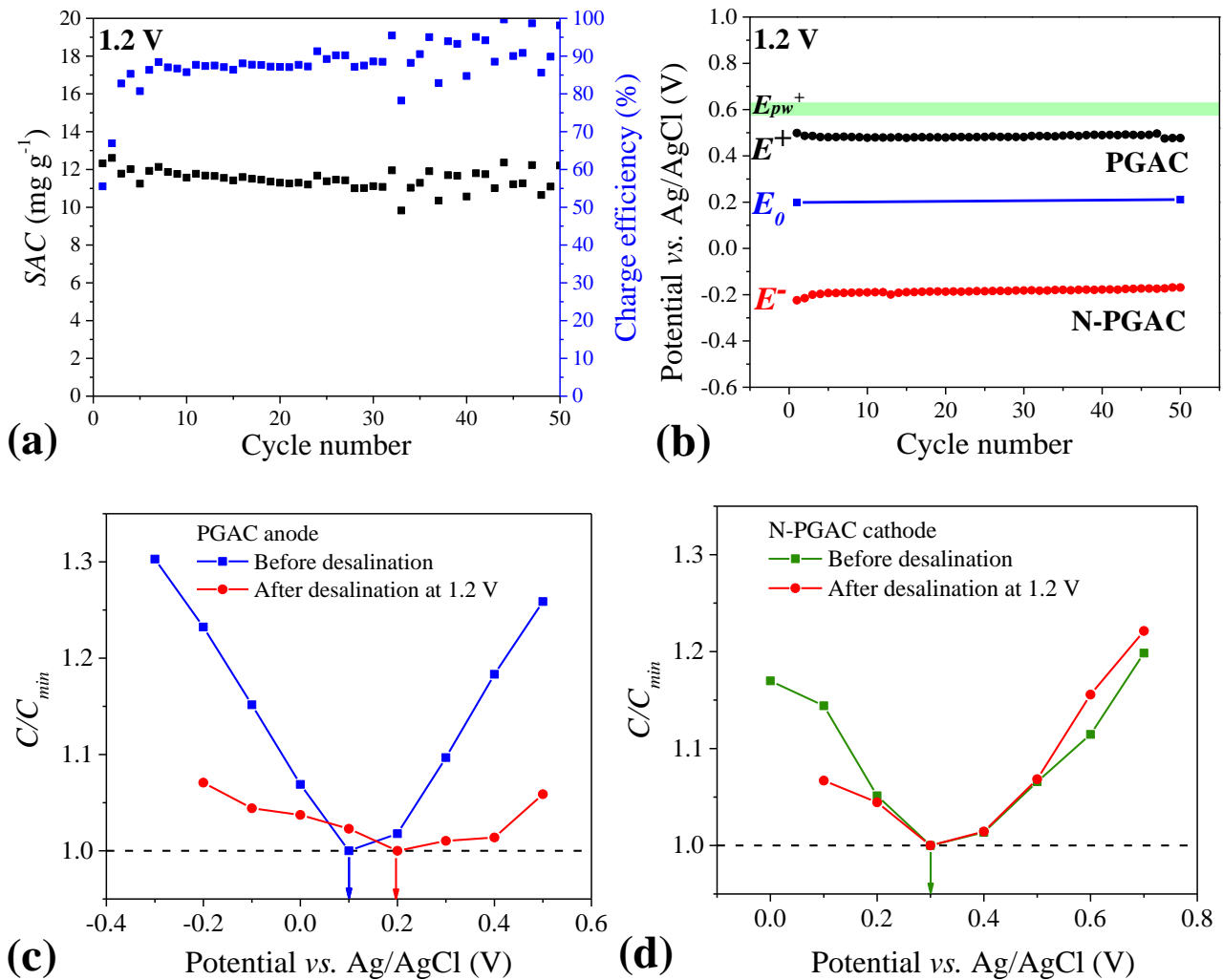
Figure 2.12. *SAC* and Q_E **(a)**, and electrode potential profiles over the desalination cycles **(b)**, using the asymmetric configuration. E_{PZC} values for the anode **(c)** and the cathode **(d)**, before and after the desalination process using the asymmetric configuration.

Another strategy to improve the electrosorption performance was using MCDI. The use of ion exchange membranes (IEMs) clearly increased *SAC* and charge efficiency (Figure 2.9(c)). For instance, at 1.2 V, *SAC* and Q_E increased by 24 and 56%, respectively (Table 2.5). This improvement could be mainly attributed to the presence of co-ions that were repelled from the

micropores and remained in the macropores, providing an additional driving force for the electrosorption of counterions, since electroneutrality must be maintained [26,40,45].

Considering that membranes introduce an additional electric resistance, the desalination experiments were also carried out applying 1.4 and 1.6 V, leading to *SAC* enhancements to 23.4 and 27.1 mg g^{-1}, respectively, while maintaining the charge efficiency close to 100%. In both cases, steady-state was achieved after ~25 cycles, but no decay of *SAC* was observed over the cycles. In order to determine whether any significant changes occurred in the electrodes, E_{PZC} was measured at the end of 50 cycles, for the process carried out at 1.6 V (Figure 2.13). It was found that E_{PZC} remained constant, suggesting that part of the voltage was used to overcome the ohmic drop associated with the membranes [29,123].
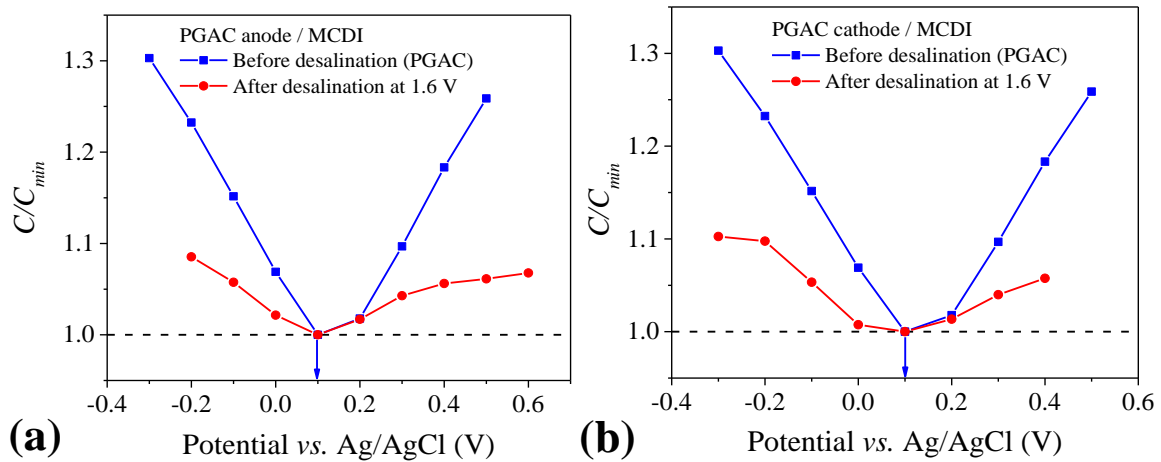
Figure 2.13. E_{PZC} values for the anode **(a)** and cathode **(b)**, before and after desalination using the MCDI configuration.

One of the drawbacks of the use of IEMs is their high cost, which constitutes the main contribution to the total cost of a CDI plant [124]. Therefore, considering that PGAC could be used directly as the positive electrode (since its E_{PZC} was in the cathode working domain), it was decided to perform MCDI using only the cationic exchange membrane (C-MCDI), in order to prevent co-ion repulsion at the PGAC cathode, given that the electrode E_{PZC} (0.1 V *vs.* Ag/AgCl) was within the cathode domain ($E_{PZC} < E_0$). Increases of 18% and 57% were observed for *SAC* and Q_E, respectively, while η decreased by 35%, compared to the symmetric configuration (1.2 V, Figure 2.9(d)). These values were also very close to those observed using both cationic and anionic membranes (1.2 V, Table 2.5), indicating that the strategy of using only the cationic exchange membrane was effective for avoiding co-ion repulsion at the cathode.

Increasing the voltage to 1.4 V resulted in decreases of Q_E and *SAC*, although E^+ remained below E_{pw}^+ (Figure 2.14(a)). As shown in Figure 2.9(d), at the beginning of the process, *SAC* was similar to that observed for the symmetric configuration, but the values diminished consistently up to the 15th cycle, reaching a constant value of 10.8 mg g^{-1} up until the 50th cycle. In order to investigate this pattern, the anode E_{PZC} was measured after the 50 cycles (Figure 2.14(b)), revealing a shift of 0.2 V *vs.* Ag/AgCl (Table 2.6), shifting the electrode operation to the anode working domain, so the *SAC* decrease could be explained by the co-ion repulsion effect. No change of E_{PZC} was detected for the cathode (Figure 2.14(c)).
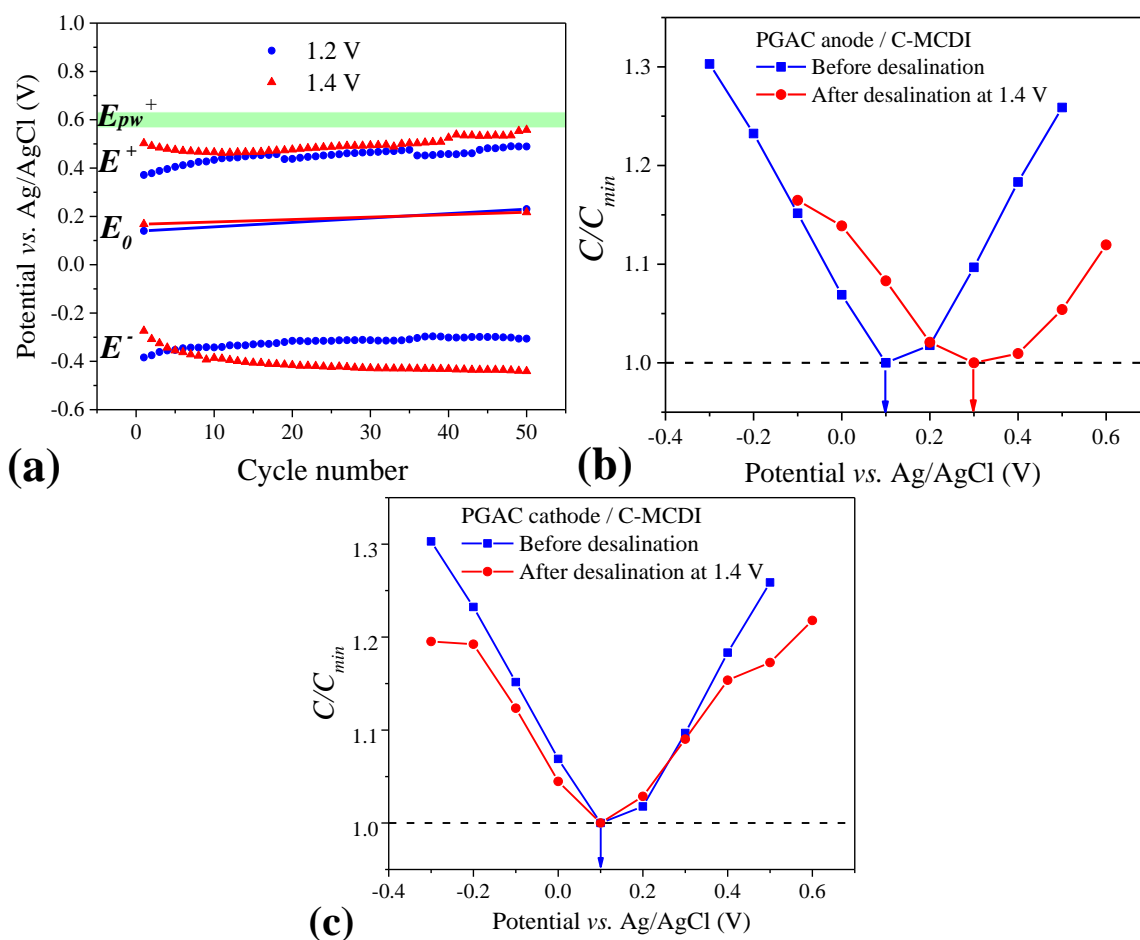
Figure 2.14. Electrode potential profiles over the desalination cycles using the C-MCDI configuration **(a)**; E_{PZC} values for the anode **(b)** and cathode **(c)**, before and after the desalination process using the C-MCDI configuration.

For comparison, electrosorption was also performed using the PGAC electrodes prepared from analytical grade glycerol (PGAC*), applying 1.2 V and using the symmetric configuration (Figure 2.15). Although higher Q_E (82.8%) and lower η (2.4 J mg^{-1}) were achieved (compared to

62.9% and 3.1 J mg^{-1}, respectively), the desalination using the PGAC* electrodes resulted in slightly lower *SAC* (12.8 mg g^{-1}), compared to the PGAC electrodes. In terms of stability, the performances of the electrodes over the cycles were similar. In conclusion, the use of PGAC* as an electrode did not seem to be feasible, since the use of purified glycerol as AC precursor would incur additional cost, without any significant advantage in terms of desalination performance. The findings confirmed that crude residual glycerol is an attractive option for use as an inexpensive and sustainable source of carbon for the preparation of electrodes employed in CDI.
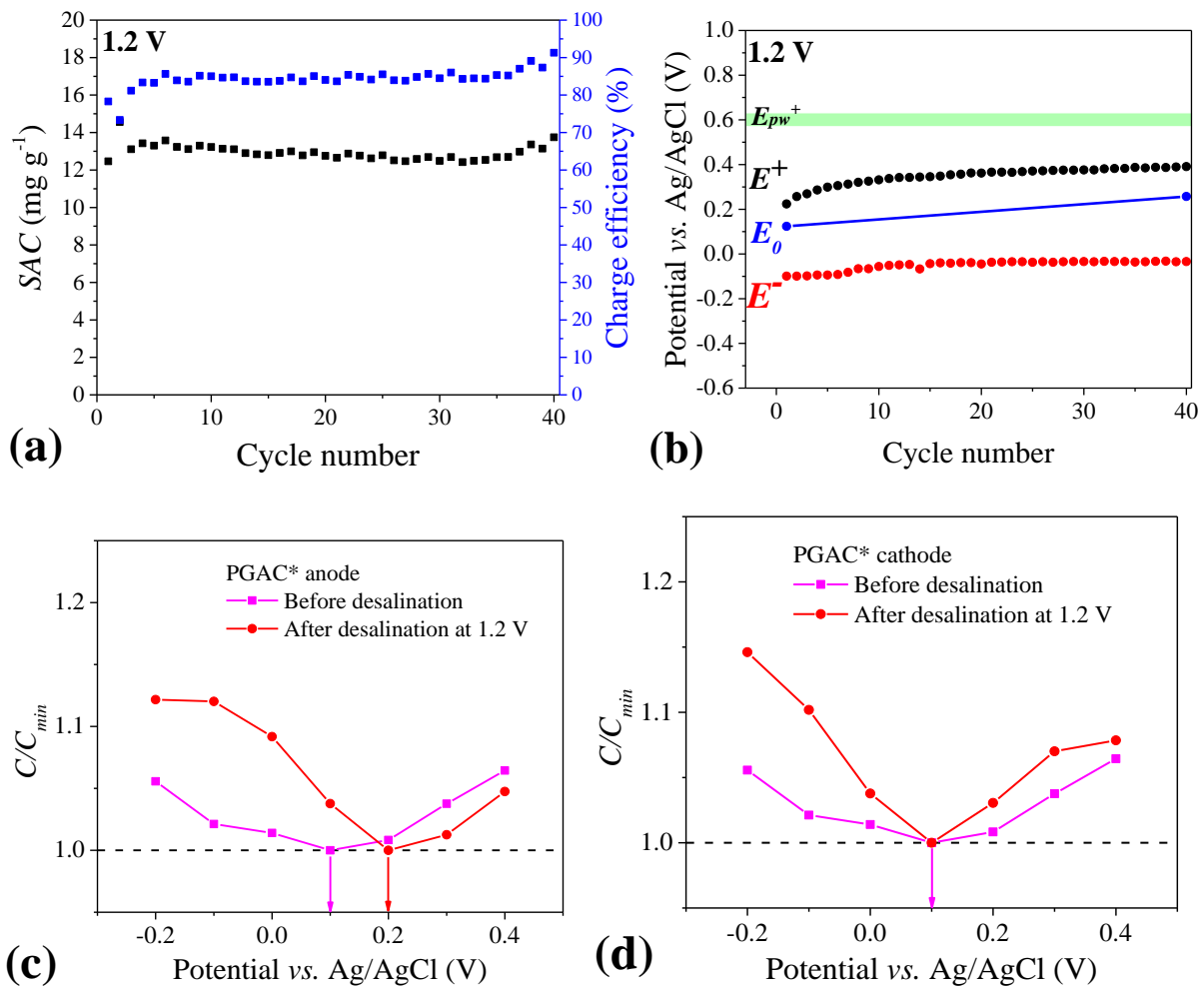
Figure 2.15. (a) *SAC* and Q_E for the PGAC* electrode (symmetric), and **(b)** electrode potential profile over the desalination cycles using the PGAC* electrode. E_{PZC} values for the anode **(c)** and cathode **(d)**, before and after the desalination process using PGAC* electrodes.

For evaluation of the electrosorption and desorption kinetics, the experimental data were successfully fitted using a pseudo-first order model ($R^2 > 0.98$). The pseudo-first order constants

(Table 2.7) depended on the configuration and the applied voltage. Desorption was faster than electrosorption and both were affected by the presence of the membrane, which made the overall process slow, since the membrane acted as a physical barrier for ion diffusion. Using the *OSR* methodology proposed by Zornitta and Ruotolo [41], simultaneous analyses of the electrosorption capacity and the adsorption/desorption kinetics were performed, in order to identify the best electrode setup.

Table 2.7 Values obtained for the optimized salt removal (*OSR*).

Electrode configurations	E_{cell} (V)	k_e x 10^3 (s^{-1})	k_d x 10^3 (s^{-1})	$t_{e\text{-}opt}$ (s)	t_d (s)	N_{cycles}	SAC (mg g^{-1})	OSR (mg g^{-1} day^{-1})
Symmetric	1.1	3.2	4.6	556	994	56	10.8	502
Symmetric	1.2	3.4	4.8	533	961	58	14.2	685
Asymmetric	1.2	4.4	4.8	444	951	62	11.5	613
MCDI	1.2	3.2	4.0	591	1145	50	17.6	741
MCDI	1.4	2.8	4.1	630	1131	49	23.4	957
MCDI	1.6	2.8	3.9	643	1192	47	27.1	1070
C-MCDI	1.2	3.0	3.7	628	1245	46	16.8	659

k_e and k_d are the pseudo-first order kinetic constants for electrosorption and desorption, respectively; $t_{e\text{-}opt}$ and t_d are the optimized electrosorption and desorption times, respectively; N_{cycles} is the number of cycles.

The results are presented in Table 2.7. The optimized electrosorption ($t_{e\text{-}opt}$) and desorption times were determined, based on maximizing the amount of salt removed and considering 99% desorption, respectively. The number of cycles was determined assuming an operation time of 24 h. Despite the slow kinetics, the best result in terms of *OSR* (1070 mg g^{-1} day^{-1}) was obtained for MCDI at 1.6 V, indicating that the highest *SAC* observed for this condition was the most relevant parameter. On the other hand, the simpler use of symmetric CDI also led to an attractive *OSR* value at 1.2 V (685 mg g^{-1} day^{-1}), although account should be taken of the higher specific energy consumption (3.1 J mg^{-1}). In conclusion, there was a tradeoff between the operational (energy) and capital (membrane) costs in determining the best CDI configuration. For example, for a small-scale desalination plant, the simplicity and low cost of the symmetric CDI would probably be the best

choice, while for a large-scale system, the operational cost could indicate the use of membranes to minimize the energy consumption. Despite the attempt to reduce the membrane cost using C-MCDI, the *OSR* was similar to that obtained using the symmetric CDI configuration, although it was notable that the lowest specific energy consumption (2.0 J mg^{-1}) was achieved using the C-MCDI configuration at 1.2 V.

Finally, comparison was made of the highest *SAC* values obtained using the PGAC electrodes in symmetric and MCDI configurations with those observed using activated carbon electrodes from other biowastes (Table 2.8). The value obtained for PGAC/CDI was higher than reported for most of the carbon electrodes derived from biomasses such as jackfruit peels, palm shells, peanut shells, waste coffee grounds, wheat straw, and woody biomass. In the case of MCDI, the *SAC* achieved using PGAC (27.1 mg g^{-1}) was higher than obtained using rice husk or sugarcane fly ash precursors.

Table 2.8 *SAC* values reported in the literature for activated carbons derived from industrial wastes or byproducts and used as electrodes for CDI.

Precursor material	NaCl concentration (mg L^{-1})	Configuration	E_{cell} (V)	*SAC* (mg g^{-1})	Reference
Citrus peel	500	Symmetric	1.5	16.2	Xie et al. [116]
Jackfruit peel	500	Symmetric	2.0	5.74	Elisadiki et al. [57]
Waste coffee grounds	292	Symmetric	1.2	12.5	Qian et al. [54]
Watermelon peel	500	Symmetric	1.2	17.4	Zhao et al. [53]
Wheat straw	30	Symmetric	-	2.67	Quan et al. [125]
Woody biomass	500	Symmetric	1.2	5.39	Dehkhoda et al. [126]
Palm shell	1000	Symmetric	1.2	3.3	Chen et al. [58]
Peanut shell	20	Symmetric	1.2	1.96	Quan et al. [127]
Lignin	585	Asymmetric	1.2	15.3	Zornitta et al. [33]
Rice husk	100	MCDI	1.5	8.09	Kim et al. [55]
Sugarcane fly ash	600	MCDI	1.2	22.8	Lado et al. [28]
Crude glycerol	600	Symmetric	1.2	14.2	This work
Crude glycerol	600	MCDI	1.6	27.1	This work

2.4   Conclusions

Maintaining electrode stability over the electrosorption/desorption cycles is essential for ensuring robust CDI operation. In this work, a new sustainable low-cost activated carbon was obtained using crude glycerol from biodiesel production. After polymerization, carbonization, and activation, the polyglycerol activated carbon was successfully employed in electrodes for the desalination of brackish water. The electrodes remained stable over 50 desalination/regeneration cycles applying potentials lower than 1.2 V, ensuring that the anode potential was below the anodic stability limit. It was also shown how the displacement of E_{PZC} over the cycles could influence SAC, due to the effect of co-ion repulsion. In order to minimize co-ion repulsion, PGAC was used as the positive electrode, while the negative electrode was the modified N-PGAC ($E_{PZC} > E_0$). This strategy succeeded in improving Q_E to 100%, but no improvement of SAC was observed. In an attempt to further improve the CDI performance, MCDI was used to increase SAC, Q_E, and OSR. A substantial improvement was observed, mainly due to charge balance in the macropores. The best cell configuration should be selected considering the tradeoff between the operational (energy) and capital (membrane) costs, depending on the scale of the desalination plant. In addition to developing an innovative application for crude glycerol, the findings also help in understanding the role of E_{PZC} and cell configurations in obtaining stable and optimized operational conditions using the PGAC electrodes.

3   CHAPTER

ROLES OF MASS TRANSFER AND CELL ARCHITECTURE IN ELECTROCHEMICAL DESALINATION PERFORMANCE USING POLYGLYCEROL ACTIVATED CARBON ELECTRODES

Capacitive deionization (CDI) has emerged as a viable alternative for brackish water desalination. Despite the remarkable advances in salt adsorption capacity (*SAC*) and charge efficiency (Q_E), improvements in cell architectures regarding the mass transfer aspects are still needed to boost electrode performance. In this work, we report a comprehensive study of flow-by (FBC), flow-through (FTC), and a percolation flow (PFC) cell architectures for brackish water desalination. It was observed that the electrode thickness was a crucial parameter influencing the desalination performance using the FBC, since the concentration gradient decreased towards the substrate interface, due to mass transfer limitations in the interstitial pores, so thin electrodes were recommended. Although the mass transfer and electrode thickness did not impose restrictions for the FTC, the short residence time limited the *SAC*, which also dramatically decreased after milling the PGAC particles, due to changes in the textural properties of the electrode, despite the fast desalination rates promoted by the mass transfer rate enhancement. Taking advantage of the beneficial aspects of the FBC and FTC designs, the desalination carried out using the PFC was enhanced by 170%. With the flow direction perpendicular to the electric field, together with electrolyte percolation, the substantial improvement of the desalination rate provided by the PFC was also observed under more realistic conditions (single-pass and galvanostatic mode). Compared to batch potentiostatic operation, the PFC presented a remarkable desalination rate of 1661 mg g^{-1} day^{-1} at 1.0 mA cm^{-2} and 7.0 mL min^{-1}. These findings enable a better understanding of the mass transfer aspects involved in CDI desalination, revealing the paramount importance of optimization not only of operational parameters, but also of the cell design.

3.1   Introduction

The global demand for fresh water is continuously increasing, due to population growth, since water is an indispensable resource for living organisms and industry. This demand has encouraged the treatment, maintenance, and conservation of water resources, as well as the development of new technologies for desalination of brackish and saline water. For this purpose,

capacitive deionization (CDI) has emerged as an environment-friendly technology that is a viable option for supplying water for consumption, since it enables the removal of ions from aqueous media [2,3,128]. The interest of the scientific community in the development of this technology has grown exponentially, due to the advantages of CDI including low energy consumption, low pressure, ease of operation and maintenance, and the possibility of energy recovery [17,129].

CDI is based on the removal of ions by electrostatic attraction and their storage in the electrical double layer (EDL) formed when two electrodes are polarized. The voltage applied across a pair of electrodes in parallel promotes formation of the EDL on the surface of an electroactive material, with the imbalance of charges driving the migration of ions to the oppositely charged electrode. Accordingly, cations and anions are captured by the negatively and positively polarized electrodes, respectively. Once saturated, the electrodes can easily be regenerated for use in another electrosorption cycle by applying a reverse potential or short-circuit. Therefore, the desalination process includes two sequential steps, namely electrosorption and desorption.

CDI is a dynamic and complex process that depends on the textural properties (specific surface area and pore size distribution) of the electroactive material, as well as its surface chemistry. Furthermore, the architecture and flow patterns inside the CDI cell can also influence operational parameters, such as the kinetics and salt removal capacity, that are important in determining the process performance. The most studied CDI cell architecture is the flow-by cell, also known as the flow-between cell, which consists of a pair of oppositely charged electrodes, separated by a gap through which the electrolyte flows. In this configuration, the electric field is perpendicular to the flow direction. Another cell architecture is the flow-through cell, in which the electrolyte flows in parallel to the electric field and permeates the pores of the electroactive film, with beneficial advantages in terms of mass transfer. Few studies have compared cell architectures and their effects on electrode performance, especially regarding mass transfer aspects [34,130–133]. A good understanding of the mass transfer fundamentals involved is essential not only for suitable design of an electrochemical cell, but also for process optimization.

A promising opportunity for a new low-cost sustainable activated carbon for CDI was recently identified in our previous study [134]. This activated carbon was prepared using crude glycerol from the biodiesel production process. Tons of this residual viscous liquid are produced every day, so a current challenge is to search for new products that can be obtained from it [61]. For industrial use, crude glycerol often needs purification (vacuum distillation, ion exchange, and nanofiltration), which is an expensive process [59,64]. Therefore, we have developed a simple and

low-cost procedure to prepare polyglycerol activated carbon (PGAC) using crude glycerol, without any requirement for purification or pretreatment. The application of PGAC in CDI has already been successfully tested, providing promising results in terms of electrosorption capacity, especially when compared with carbon materials with similar salt adsorption capacity and that involve the use of expensive precursors or laborious syntheses [32,51,135]. Therefore, given the potential of PGAC for CDI, together with the concept of water-waste-energy nexus, environmental concerns, and economic appeal, PGAC electrodes were employed in this study.

The aim of the present work was to understand how hydrodynamic aspects influence the mass transfer phenomena and kinetics of the desalination process, considering the CDI cell architecture. Therefore, the flow-by (FBC) and flow-through (FTC) cell architectures were compared in terms of electrosorption performance and kinetics. Evaluation was made of the effects of the PGAC thickness and particle diameter on the electrode properties and the desalination process. Considering the results obtained for the FBC and FTC, a new cell architecture called the percolation flow cell (PFC) was proposed, combining the beneficial aspects of each cell regarding the electrochemical and mass transfer aspects. Desalination using the PFC was investigated considering the operational conditions that would be found in a real CDI process, employing the galvanostatic mode and single-pass flow.

3.2   Experimental

3.2.1   Materials

Crude glycerol (~80% glycerol) was obtained from a glycerol purification plant located in Brotas, São Paulo State, Brazil. For glycerol polymerization, sulfuric acid (Sigma-Aldrich) was used as catalyst. Potassium hydroxide pellets (Sigma-Aldrich) were used for chemical activation, hydrochloric acid (37%, Neon) was the neutralization reagent in the washing step, and hydrofluoric acid (40%, Nuclear) was used in the leaching process. The electrodes were prepared using polyvinylidene fluoride (PVDF, Sigma-Aldrich) and polytetrafluoroethylene (PTFE, 60 wt%, Sigma-Aldrich) as binders, and n-methyl-pyrrolidone (NMP, 99.5%, Synth) and ethyl alcohol (99.8%, Neon) as solvents. Carbon black (CB) (VXC72, Cabot, Brazil) was tested to improve the electrode conductivity. All the solutions were prepared using deionized water. Sodium chloride (Synth) was used to prepare the electrolytes for the characterization and desalination experiments.

3.2.2   Glycerol polymerization and preparation of the activated carbon and electrode

The glycerol polymerization procedure was adapted from Medeiros and Lago [99]. Briefly, 100 g of crude glycerol was added to a beaker and stirred and heated in a glycerin bath at 150 $^\circ$C. Then, 20 mL of H_2SO_4 aqueous solution (5% mol) was slowly added to the beaker to start the polymerization. The reaction was left for 7.5 h, after which the viscous solution formed was dried for 12 h in an oven at 150 $^\circ$C, to obtain the polyglycerol (PG). The material was carbonized and activated in a tubular furnace (Lindberg Blue M, Thermo Scientific), in an N_2 atmosphere, according to the optimized conditions described previously [27]. The carbonization was carried out for 1 h at 600 $^\circ$C, with heating at a rate of 10 $^\circ$C min^{-1}, under a 300 mL min^{-1} flow of N_2. The carbonized samples were mixed with KOH pellets (1:4 wt/wt carbon:KOH) and left for 24 h. After this, they were activated for 1.5 h at 850 $^\circ$C, with heating at 10 $^\circ$C min^{-1}, under a 150 mL min^{-1} flow of N_2. The carbon was washed with HCl (0.5 mol L^{-1}) and copious distilled water until reaching a constant pH. Finally, the polyglycerol activated carbon (PGAC) was dried at 105 $^\circ$C, during 24 h, prior to electrode preparation.

The electrodes were prepared following two procedures: blade-casting (BC) and free-standing (FS). The BC electrodes were prepared using different percentages of binder (10 wt% or 5 wt%) and carbon black. Firstly, the PGAC was crushed and the particles passing through a 325-mesh sieve (diameter lower than 43 µm) were collected to prepare the electrode. The PVDF dissolved in NMP was then added to the PGAC (90 wt% or 95 wt%) to form a slurry, which was poured onto a graphite sheet substrate and spread out using a doctor-blade machine to obtain carbon films with a thickness of 477 µm. These electrodes were labeled as PGAC95 and PGAC90. Aiming to remove residual inorganics present in the PGAC, such as silicon, a further treatment was tested by leaching it with an aqueous HF solution (40%), for 12 h [55]. The sample was washed with distilled water until constant pH, followed by drying for 24 h in an oven at 105 $^\circ$C. This sample was labeled HF-PGAC and the electrode was denoted HF-PGAC90. Another electrode was also prepared, adding CB in an attempt to improve the conductivity and increase the electrosorption capacity. This electrode was composed of 85 wt% PGAC, 5 wt% PVDF, and 10 wt% CB, and was labeled as HF-PGAC85CB10.

In the second part of this work, focused on comparison of the FBC and FTC, FS electrodes were prepared for use in the flow-through configuration. In this case, the crushed PGAC particles (<43 µm) and 5 wt% PTFE binder were used to prepare the electrodes. The type and amount of binder were previously optimized considering the mechanical stability of the electrode. The activated carbon was mixed with ethanol to obtain a homogeneous slurry. Subsequently, PTFE was

added and the mixture was kneaded and then rolled out using a rolling machine (Atlas 150, Marcato), to obtain free-standing electrodes with different thicknesses (ξ, 387 μm and 562 μm), in order to investigate the influence of this parameter on the desalination performance. The electrodes were dried for 24 h in an oven at 120 °C. Another parameter evaluated was the particle size. In this case, the PGAC was crushed in a ball mill (SL 38, Solab) for 40 min, in order to obtain smaller particles. The FS electrode was prepared following the same procedure described above, but with a thickness of 344 μm.

3.2.3 Material characterization

Thermogravimetric (TG) analyses of the PGAC and HF-PGAC were performed using a TGA Q500 analyzer (TA Instruments). The sample was heated in a platinum pan from room temperature to 900 °C, under an air atmosphere (60 mL min^{-1}), applying a heating rate of 10 °C min^{-1}. In order to evaluate the efficacy of particle milling, the PGAC particles were suspended in distilled water and analyzed using a laser diffraction particle size analyzer (Mastersizer Micro Plus, Malvern Instruments). The particle size distributions showed that after milling, the median particle diameter (D_{50}) decreased from 34.2 μm to 8.84 μm. Nitrogen physisorption measurements were carried out using a Micromeritics ASAP 2420 instrument. Before the measurements, the samples were first degassed at 90 °C (1 h) and then at 150 °C (12 h). The specific surface area was calculated from N$_2$ isotherms using the Brunauer-Emmett-Teller equation (SSA_{BET}), considering the relative pressure (P/P$_0$) interval 0.05-0.20 (linear isotherm region). The pore size distribution (PSD) and total pore volume (V_T) were calculated using the 2D-NLDFT heterogeneous surface model, performed with SAIEUS software. The micropore volume (V_{mic}) was the volume of N$_2$ adsorbed for pores ≤2 nm, while the mesopore volume (V_{mes}) was calculated as the difference between V_T and V_{mic}. The average pore diameter (d_{50}) was determined considering the pore diameter at which the volume adsorbed was half of V_T. The electrode wettability (hydrophobicity/hydrophilicity) was determined from contact angle measurements, according to the sessile drop method. Briefly, a water droplet was deposited onto the surface of the electrode; after 20 s, the angle between the line tangent to the drop liquid interface and the baseline was measured.

3.2.4 Electrochemical characterizations

Cyclic voltammetry (CV), galvanostatic charge-discharge (GCD), and electrochemical impedance spectroscopy (EIS) measurements were performed using a three-electrode Swagelok

cell, a potentiostat (PGSTAT204, Autolab), and Ag/AgCl (saturated KCl) as the reference electrode. The same electrodes were used as both working and counter electrodes. All the characterizations were performed in 1.0 mol L^{-1} NaCl solution, except for EIS analyses for determination of the potential of zero charge (E_{PZC}), which used the same concentration employed in the electrosorption experiments (600 mg L^{-1}).

The CV was carried out at two different scan-rates (v), 1 mV s^{-1} and 10 mV s^{-1}, in a potential window between 0.1 V and 0.6 V $vs.$ Ag/AgCl, as determined previously [134]. The specific capacitance ($C_{S,CV}$) and total specific capacitance (C_{CV}), expressed in F per gram of electroactive carbon, were calculated using Eqs. (3.1) and (3.2), respectively, where I is the current (A), m is the mass of the working electrode (g), and E_1 and E_2 are the lower and upper values of the potential window, respectively.

$$C_{S,CV} = \frac{I}{v\,m} \tag{3.1}$$

$$C_{CV} = \frac{\int_{E_1}^{E_2} I\,dV}{v\,m\,(E_2 - E_1)} \tag{3.2}$$

For GCD, a current density of 0.1 A g^{-1} was applied, considering cut-off potentials of 0.6 and 0.1 V ($vs.$ Ag/AgCl) for charging and discharging, respectively. The GCD specific capacitance ($C_{S,GCD}$) was calculated from the slope of the discharging curve, using Eq. (3.3), in which I_d is the discharging current (A), Δt is the discharging time (s), and ΔE is the potential drop observed during the discharge (V $vs.$ Ag/AgCl), subtracting the ohmic drop (IR_{drop}).

$$C_{S,GCD} = \frac{I_d\,\Delta t}{m\,\Delta E} \tag{3.3}$$

The EIS was also performed using the CDI cell to investigate the electric elements associated with the different cell architectures. In this case, a potential of 0.0 V $vs.$ Ag/AgCl was applied, with an amplitude of 10 mV, from 1 mHz to 100 kHz. The specific capacitance obtained from the EIS ($C_{S,EIS}$) was calculated using Eq. (3.4), in which ω is the angular frequency and Z'' is the imaginary component of the impedance spectrum.

$$C_{S,EIS} = \frac{1}{|\omega Z''|} \tag{3.4}$$

In order to determine the ohmic resistance (R_Ω), charge-transfer resistance (R_{CT}), admittance (A_0), capacitance at the electrolyte/electrode interface (C_{INT}), and the capacitance inside the micropores (C_{EIS}), the EIS Nyquist plots were fitted to a modified Randle equivalent circuit, using Metrohm Autolab NOVA software. A constant phase element (CPE) was used to adjust the nonideality of the semicircles, commonly assigned to surface roughness, surface inhomogeneities,

and complexity of the double-layer structure present in this type of electrode. As shown in Eq. (3.5), the CPE impedance is related to the non-ideal capacitance (Q^0), the ideality factor (N), which ranges from 0 to 1, the imaginary number (j), and the angular frequency (ω) [100]. These variables were used to estimate C_{INT} using Eq. (3.6).

$$CPE = \frac{1}{(j\omega)^N Q^0} \tag{3.5}$$

$$C_{INT} = \frac{(Q^0)^{\frac{1}{N}}(R_{CT})^{\frac{1-N}{N}}}{m} \tag{3.6}$$

For E_{PZC} determination, fixed frequency, amplitude, and potential step (10 mHz, 30 mV, and 100 mV, respectively) were applied. At each potential, $C_{S,EIS}$ was calculated using Eq. (3.4) and the values were normalized considering the lowest capacitance value (C_{min}). The E_{PZC} value corresponded to the potential at $C/C_{min} = 1$.

3.2.5   Electrosorption experiments

The preliminary electrosorption experiments were performed in a recirculating bath mode, using three desalination cell architectures: flow-by (FBC), flow-through (FTC), and percolation flow (PFC), shown schematically in Figure 3.1. The cells consisted of two acrylic plates attached to current collectors. In the FBC and PFC configurations, the pair of electrodes were 2.5 x 2.5 cm^2, with graphite plates used as electric contactors, while the electrodes in the FTC configuration had a diameter of 2.82 cm, ensuring a similar electrode area (6.25 cm^2), for comparison purposes, with a titanium mesh used as electric contactor. In the FBC and FTC, the gap between the electrodes (2.0 mm) was filled with a plastic mesh to promote hydrodynamic turbulence and also to avoid short circuit. Differently, the electrodes in the PFC were separated by a piece of filter paper. The cells were assembled using nuts and bolts, with rubber gaskets providing tight sealing.

For the desalination assays, the NaCl electrolyte (600 mg L^{-1}) was pumped at a constant flow rate (26 mL min^{-1}) from a 25 mL reservoir to the recirculating bath system, using a peristaltic pump (Masterflex L/S, Cole-Parmer). A potentiostat (PGSTAT204, Autolab) provided constant cell potentials of 1.2 V and 0.0 V during the electrosorption and desorption steps, respectively. The desalination was carried out up to electrode saturation, with 15 electrosorption/desorption cycles to ensure the steady-state condition. The solution conductivity and pH were measured at the exit of the cell using a Seven Excellence instrument (Mettler Toledo). The conductivity value was corrected considering the pH and

temperature fluctuations during the experiment, according to the methodology described by Lee et al. [103].

The desalination performance of the electrode was evaluated considering the salt adsorption capacity (SAC), charge efficiency (Q_E, no leakage current discount), and specific energy consumption (η), calculated using Eqs. (3.7), (3.8), and (3.9), respectively. In these equations, C_0 is the initial salt concentration (mg L^{-1}), C_t is the salt concentration (mg L^{-1}) at time t (s), V is the electrolyte volume (L), m_E is the mass of active material in both electrodes (g), z is the ion valence, F is the Faraday constant (96,485 C mol^{-1}), M_{NaCl} is the molecular weight of NaCl (58,440 mg mol^{-1}), I is the total current applied to the cell (A), E_{cell} is the cell potential in the electrosorption step (V), m_{rem} is the quantity of ions removed from the solution (mg), and t_1 and t_2 are the times at which the electrosorption step started and finished, respectively.

1) Bolt
2) Acrylic Plate
3) Rubber Gasket
4) Current Collector
5) Electrode
6) Plastic Mesh
7) Nut
8) Filter Paper
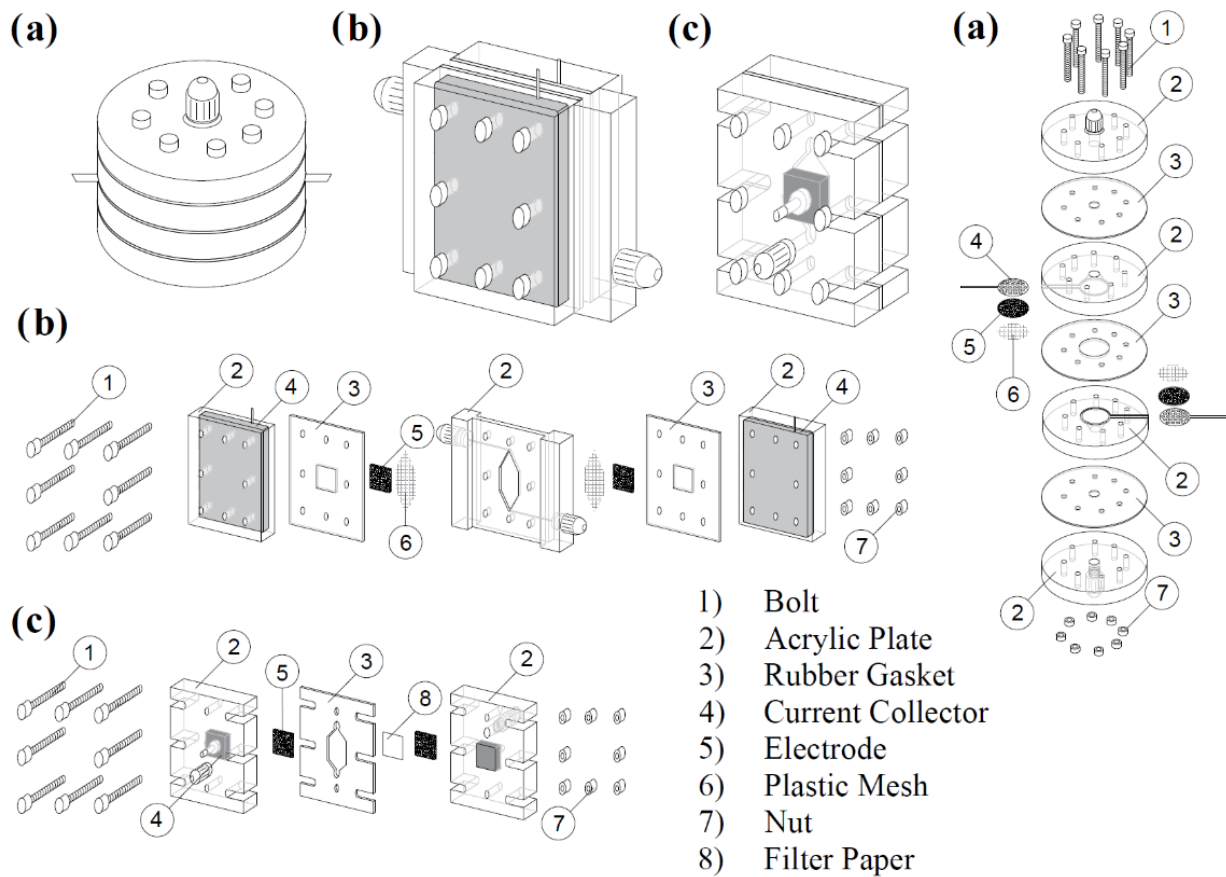
Figure 3.1. Schematic illustrations of the CDI cells and their components: **(a)** FTC, **(b)** FBC, and **(c)** PFC.

$$SAC = \frac{(C_0 - C_t)\, V}{m_E} \tag{3.7}$$

$$Q_E = 100 \frac{z\,F\,m_E\,SAC}{M_{NaCl} \int_{t_1}^{t_2} I dt} \tag{3.8}$$

$$\eta = \frac{\int_{t_1}^{t_2} E_{cell}\,I\,dt}{m_{rem}} \tag{3.9}$$

The overall performance was investigated with simultaneous analysis of the electrosorption capacity and the adsorption/desorption kinetics, according to the optimized salt removal (*OSR*) approach proposed by Zornitta and Ruotolo [41]. The *OSR* value represents the amount of salt removed per gram of electrode material in a pre-determined operational time (mg g^{-1} day^{-1}). Since the *SAC* and the kinetics influence the number of cycles and, consequently, the capacity for removing salt, a separate analysis of these parameters can lead to incorrect conclusions concerning the best electrode and operational conditions.

Finally, for the electrode and cell architecture displaying the best desalination performance, the desalination was carried out in single-pass mode and applying a constant current, which are conditions that reproduce a real desalination operation. In these experiments, the NaCl electrolyte (1000 mg L^{-1}) was pumped by the peristaltic pump from a reservoir (2 L) to the reactor, at a constant flow rate (7, 10, or 13 mL min^{-1}). For comparison, a potentiostatic desalination was performed applying 1.2 V and 0.0 V during the electrosorption and desorption steps, respectively. In the galvanostatic desalination, a constant current density (0.5, 1.0, or 1.5 mA cm^{-2}) was applied during the electrosorption, up to the cutting cell potential (*E$_{cc}$*) of 1.2 V, with electrode regeneration performed by inversing the electrode polarization (-0.5, -1.0, or -1.5 mA cm^{-2}), until reaching *E$_{cc}$* of 0.0 V. The galvanostatic mode was investigated because it has been identified as being the most energy-efficient for CDI [136]. In this case, the *SAC* was calculated according to Eq. (3.10), where $\dot{V}$ is the volumetric flow rate (L min^{-1}).

$$SAC = \frac{\dot{V} \int_{t_1}^{t_2} C(t)\,dt}{m_E} \tag{3.10}$$

3.3   Results and discussion

In a previous work, we developed a new sustainable activated carbon (AC) electrode using crude residual glycerol as raw material. After full carbon and electrode characterizations, the best cell configuration to obtain fast kinetics and high electrosorption capacity was established as being the symmetric one, operating at 1.2 V. Although the focus of the present work was to investigate different cell configurations, considering the flow and electric field directions, it was evident that

some aspects regarding electrode preparation should be first addressed, in order to further improve the desalination capacity and kinetics of the electrodes. Therefore, as an attempt to remove the inorganics remaining in the AC after activation (12.5%), a leaching with aqueous HF was tested. In addition, the amount of binder used to confer mechanical stability to the carbon film was minimized, since it affected the electrical resistance, and CB was added to improve the electrode conductivity.

The overall yield (*g* AC / *g* polyglycerol) for HF-PGAC was lower than that observed for PGAC (Table 3.1), indicating that the inorganics had been successfully leached from the carbon samples. This was confirmed by the TG analysis (Figure 3.2(a)), which demonstrated the effectiveness of the inorganics leaching, since the ash (the mass remaining at temperatures higher than 700 ^{o}C) in the activated carbon was reduced by 56% after HF treatment, leaving only 5.7% of inorganics that were not solubilized. The DTG results (Figure 3.2(b)) showed similar profiles for PGAC and HF-PGAC, with high thermal stability up to 500 ^{o}C, followed by substantial weight loss as the temperature increased further, due to the release of volatiles not eliminated during the carbonization step. Two thermal events were observed in the DTG curves, with the first attributed to the release of oxygen functional groups, while the second was related to carbon decomposition reactions involving the breaking of C–C bonds [109,110].

Table 3.1. Mass yields: polyglycerol polymerization (Y_P), carbonization (Y_C), activation (Y_A), treatment with HF (Y_T), and overall (Y_O).

	Y_P (%)[a]	Y_C (%)[b]	Y_A (%)[c]	Y_T (%)[d]	Y_O (%)
PGAC	47.5 ± 1.8	20.2 ± 1.3	32.2 ± 3.6	-	6.5 ± 0.7[e]
HF-PGAC	47.5 ± 1.8	20.2 ± 1.3	32.2 ± 3.6	79.6 ± 0.0	5.2 ± 0.0[f]

[a] g glycerol/g polyglycerol; [b] g PGC/g polyglycerol; [c] g PGAC/g PGC; [d] g HF-PGAC/g PGAC; [e] g PGAC/g polyglycerol; [f] g HF-PGAC/g polyglycerol.
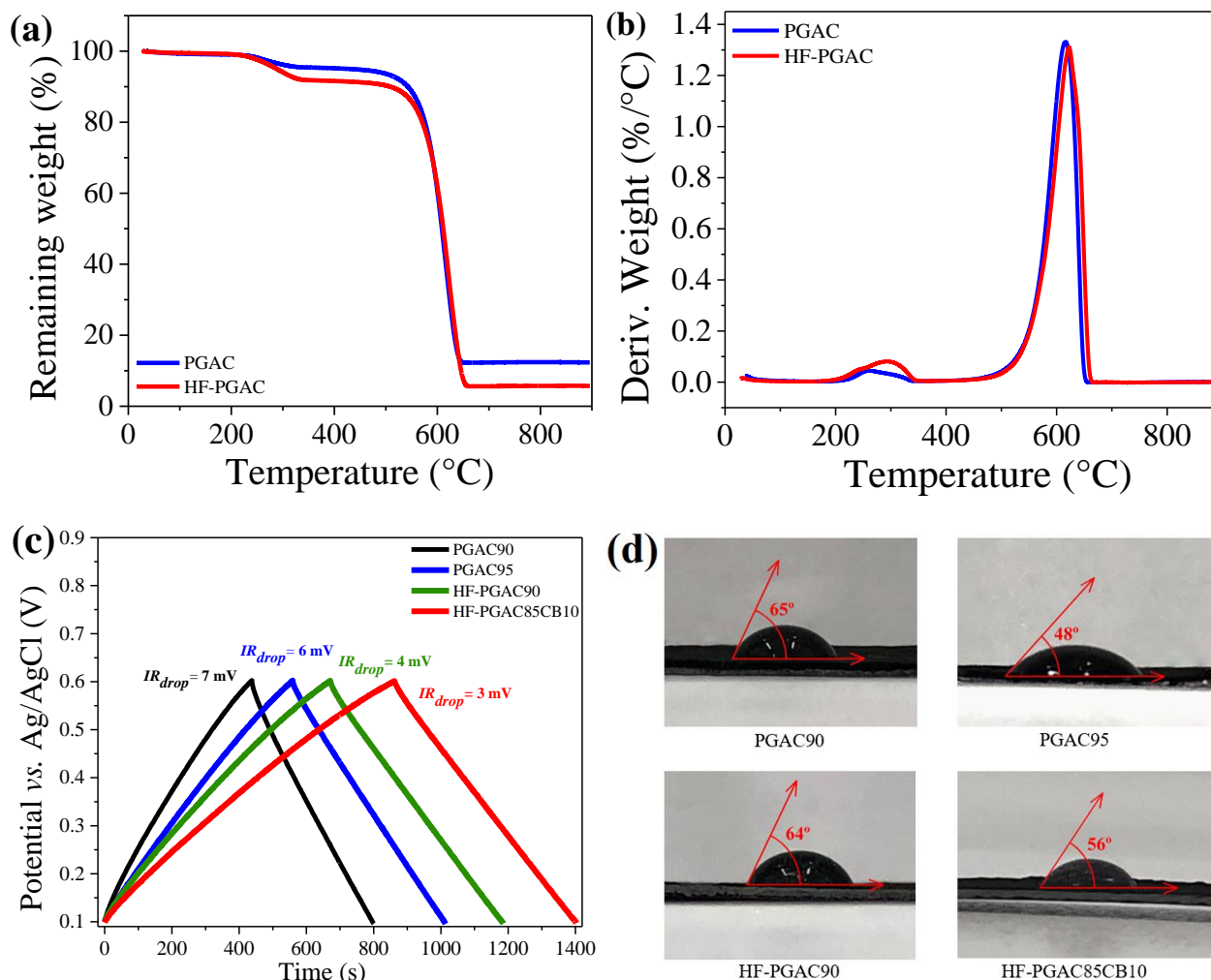
Figure 3.2. (a) TG and **(b)** DTG profiles for PGAC and HF-PGAC, obtained under an air atmosphere; **(c)** galvanostatic charge-discharge (GCD) profiles, recorded at 0.1 A g⁻¹ (NaCl 1.0 mol L⁻¹); **(d)** contact angles of the electrodes.

The electrodes were electrochemically characterized using cyclic voltammetry (Figure 3.3), which revealed the quasi-rectangular shape typical of electrochemical double layer capacitive behavior. The capacitance values observed from the CV (C_{CV}) and GCD (C_{GDC}, Figure 3.2(c)) analyses indicated the same trend in the charge storage capacity: HF-PGAC90 $\approx$ HF-PGAC85CB10 > PGAC95 > PGAC90. This same trend was observed for the *SAC* values, summarized in Table 3.2, revealing the effects of the HF treatment, binder, and CB addition on the electrode performance.
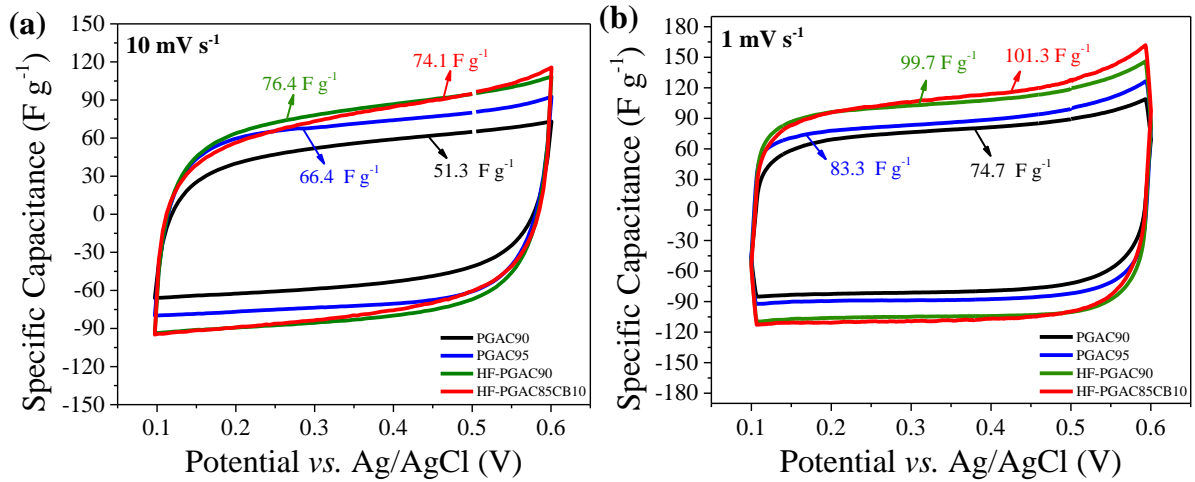
Figure 3.3. Specific capacitance from cyclic voltammograms recorded at **(a)** 10 mV s^{-1} and **(b)** 1 mV s^{-1} for all the electrodes evaluated, and their respective total specific capacitance. Electrolyte: 1 mol L^{-1} NaCl.

Table 3.2 Desalination results (*SAC*, Q_E, and η) obtained using the different electrodes.

Electrode	*SAC* (mg g^{-1})	Q_E (%)	η (J mg^{-1})
PGAC90	10.0 ± 0.3	58.5 ± 2.4	3.4 ± 0.1
PGAC95	12.4 ± 0.6	58.7 ± 2.8	3.4 ± 0.1
HF-PGAC90	13.5 ± 0.9	61.7 ± 2.4	3.2 ± 0.1
HF-PGAC85CB10	13.5 ± 0.9	56.9 ± 3.7	3.2 ± 0.2

*Note: Batch desalination using 600 mg L^{-1} NaCl.

Comparing the PGAC90 and HF-PGAC90 electrodes, a 35% improvement of *SAC* was observed after HF treatment. This enhancement could be attributed to the higher carbon content in HF-PGAC, resulting from the removal of inorganics, making this electrode more effective for electrosorption. With the aim of improving the electrode conductivity, while ensuring mechanical stability, the amount of binder was reduced to 5% in the PGAC95 electrode. Although the impact on *IR$_{drop}$* was negligible (Figure 3.2(c)), a 24% increase of *SAC* was observed, which could be explained by higher *SSA* available for electrosorption, due to reduced pore clogging by the binder [134,137], as well as the higher hydrophilicity (lower contact angle) of PGAC95 (Figure 3.2(d)),

which improved the access of aqueous electrolytes to the pores, favoring electrosorption and the kinetics of the process [96,138].

Considering the beneficial effects of HF leaching and binder reduction, the HF-PGAC85CB10 electrode was prepared in an attempt to further improve the electrode conductivity and *SAC*. As shown in Figure 3.2(c), CB addition led to a negligible decrease of IR_{drop} and no *SAC* enhancement, compared to HF-PGAC90. Similar results were found elsewhere [14]. Interestingly, the removal of the inorganics from the PGAC samples had a greater effect than CB on decreasing IR_{drop}, since the carbon matrix had a higher content of heteroatoms that could act as electron barriers in microcrystalline units [139].

Finally, from an engineering point of view, although the HF treatment increased the *SAC* by 8.9%, the overall yield (Y_O) decreased by 20% (Table 3.1), so for a practical application, the increase of the electrode preparation cost would be unattractive. Furthermore, there were no substantial differences for Q_E and η (Table 3.2). In view of all these aspects, the PGAC95 electrode was selected for use in the study of the cell configurations.

3.3.1 Cell architectures and electrode configurations

Considering that the relative directions of the flow velocity and the electric fields can influence the electrosorption process, investigation was made of the electrochemical desalination performance using three CDI cell architectures: flow-by (FBC), flow-through (FTC), and percolation flow cell (PFC). In the FBC and PFC, the flow velocity and electric field directions are perpendicular to each other, while they are parallel in the FTC. Furthermore, in the FBC configuration, the electrolyte flows tangentially to the outer surface of the electrode, while in the FTC and PFC, the electrolyte is forced to permeate through the interstitial pores of the electrode. Firstly, the FBC and FTC architectures were investigated and, in both cases, the mass transfer and electrode charging led to significant differences in desalination performance in terms of *SAC*, Q_E, and η, as shown in Figure 3.4, for two electrode thicknesses. The thinner electrode in the FBC configuration (Figure 3.4(a)) displayed superior electrosorption performance, with the highest *SAC* and Q_E. This could be attributed to the lower R_{CT} and higher A_0 (Table 3.3), which facilitated electrode charging and mass transfer diffusion in the micropores, respectively. This same trend has been observed elsewhere in comparison of the FBC and FTC for desalination [131], where poor performance of the FTC was attributed to faradaic side reactions, in agreement with the lower Q_E values displayed in Figure 3.4(a). Interestingly, the high external particle mass transfer promoted by

using the FTC configuration was not sufficient to improve its performance, probably due to the short residence time, compared to the FBC architecture.
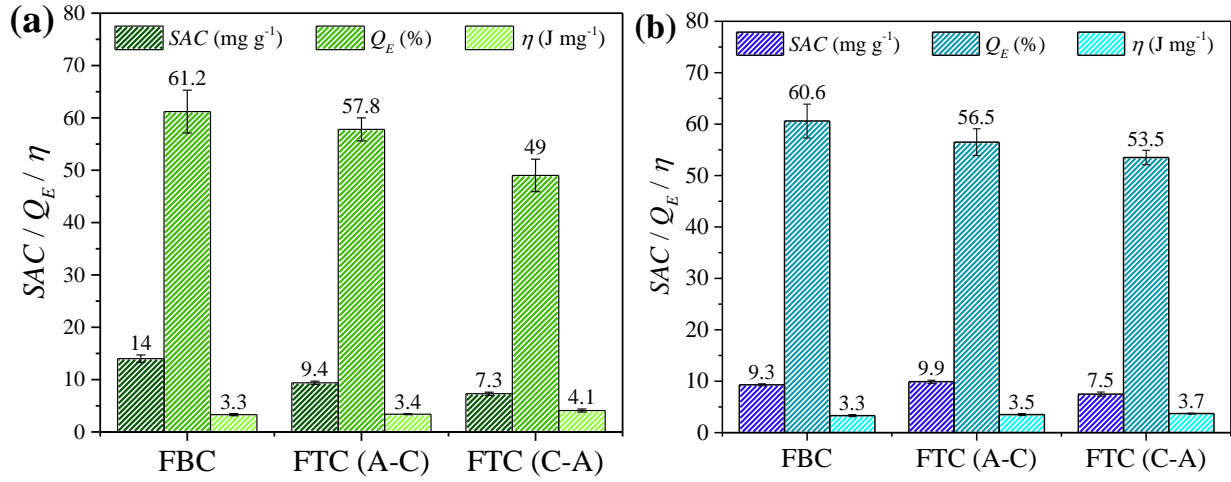
Figure 3.4. Batch desalination performance for different cell architectures: **(a)** $\xi = 387$ μm and **(b)** $\xi = 562$ μm. $D_{50} = 34.2$ μm, 600 mg L^{-1} NaCl, 1.2 V (electrosorption), and 0.0 V (desorption).

Table 3.3 Capacitance and EIS parameters obtained from fitting the Nyquist plots with a modified Randle equivalent circuit (Fitting results in Figure 3.5)

Cell	ξ (μm)	D_{50} (μm)	R_Ω (Ω)	R_{CT} (Ω)	C_{INT} (mF g^{-1})	A_0 (S s$^{1/2}$)	C_{EIS} (F g^{-1})
FBC	387	34.2	0.57	0.95	231	11	138
FBC	562	34.2	0.26	0.83	109	49	119
FBC	344	8.84	0.13	1.40	141	14	97
FTC	387	34.2	0.06	36.7	5	2	126
FTC	562	34.2	0.06	6.58	2	5	127
FTC	344	8.84	0.49	15.8	1	3	159

(g)
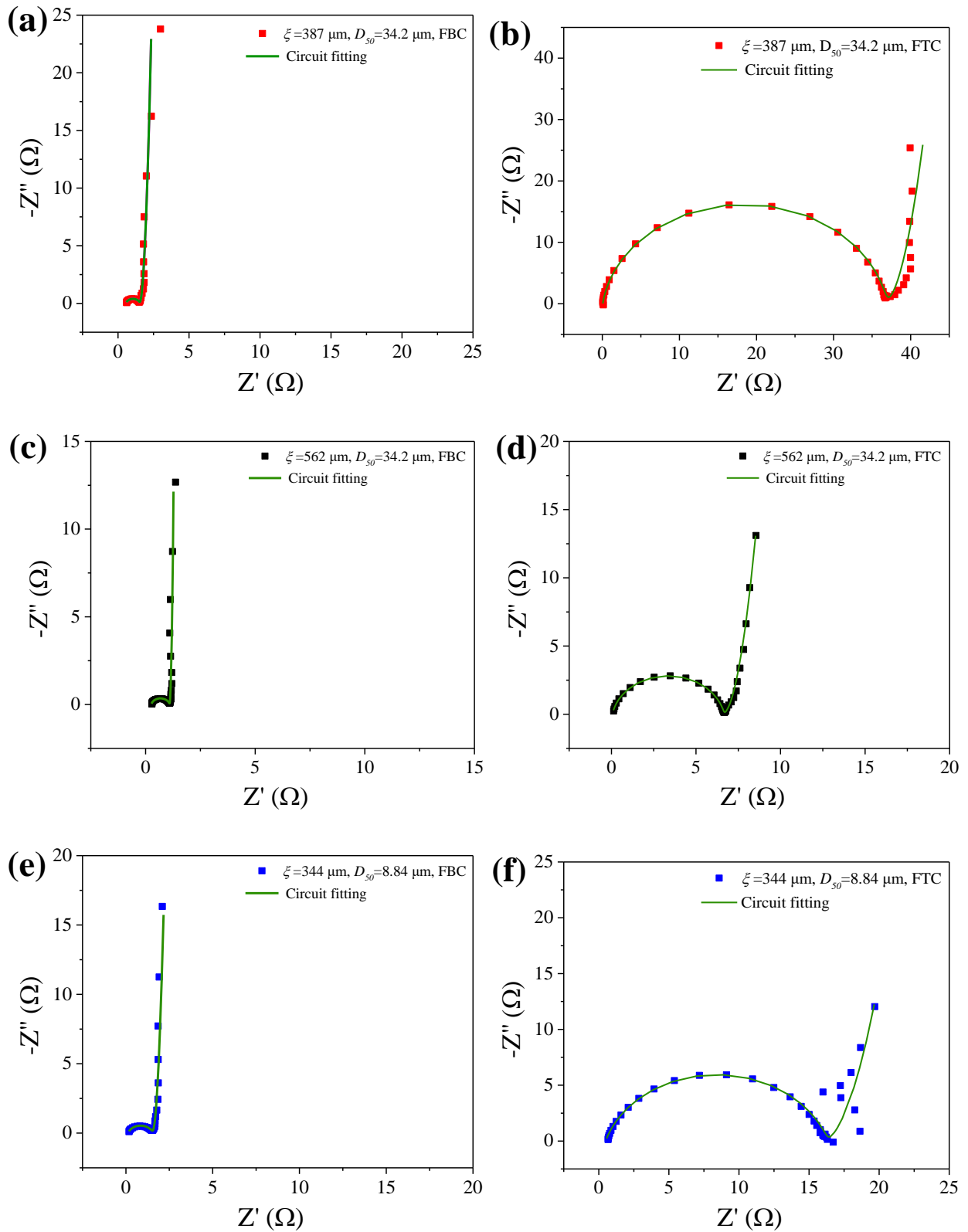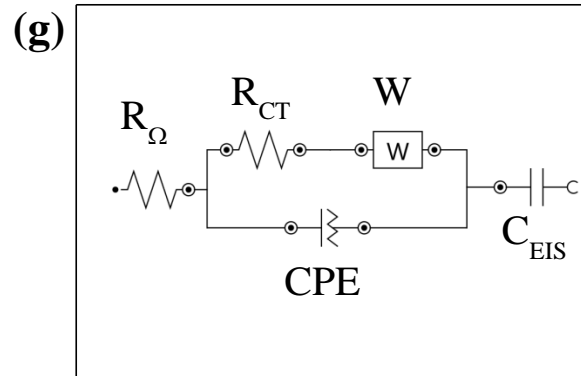
Figure 3.5. (a-f) EIS spectra and modified Randle equivalent circuit fitting for each electrode and cell design; **(g)** modified Randle equivalent circuit. Electrolyte: 1 mol L^{-1} NaCl.

In the FTC, the electrolyte can flow from the anode to the cathode (A-C), or contrariwise (C-A). As shown in Figure 3.4, the different arrangements presented differences in desalination performance. The FTC(C-A) showed lower *SAC* than the FTC(A-C), irrespective of electrode thickness. In order to investigate this outcome, the E_{PZC} was measured before and after the desalination cycles (Figure 3.6). The pristine electrode had E_{PZC} of 0.1 V *vs.* Ag/AgCl and, unlike the cathode, E_{PZC} shifts were observed for the anode after desalination. The highest E_{PZC} anode shift was 0.2 V *vs.* AgCl for FTC(C-A), indicating that in this configuration, the anode was more susceptible to oxidation of the carbon surface, since oxygen functional groups have negative charges, causing the E_{PZC} to shift to more positive values [120,121]. The E_{PZC} displacement can directly affect electrosorption performance. Considering that the short-circuit potential (E_0) for the FTC was 0.16 V *vs.* Ag/AgCl, the E_{PZC} of the anode was displaced from the cathode to the anode domain (Figure 3.6(a and c)). Consequently, part of the applied potential was deviated to co-ion repulsion [134], explaining the lower Q_E values observed for FTC(C-A) and the poor electrosorption performance.
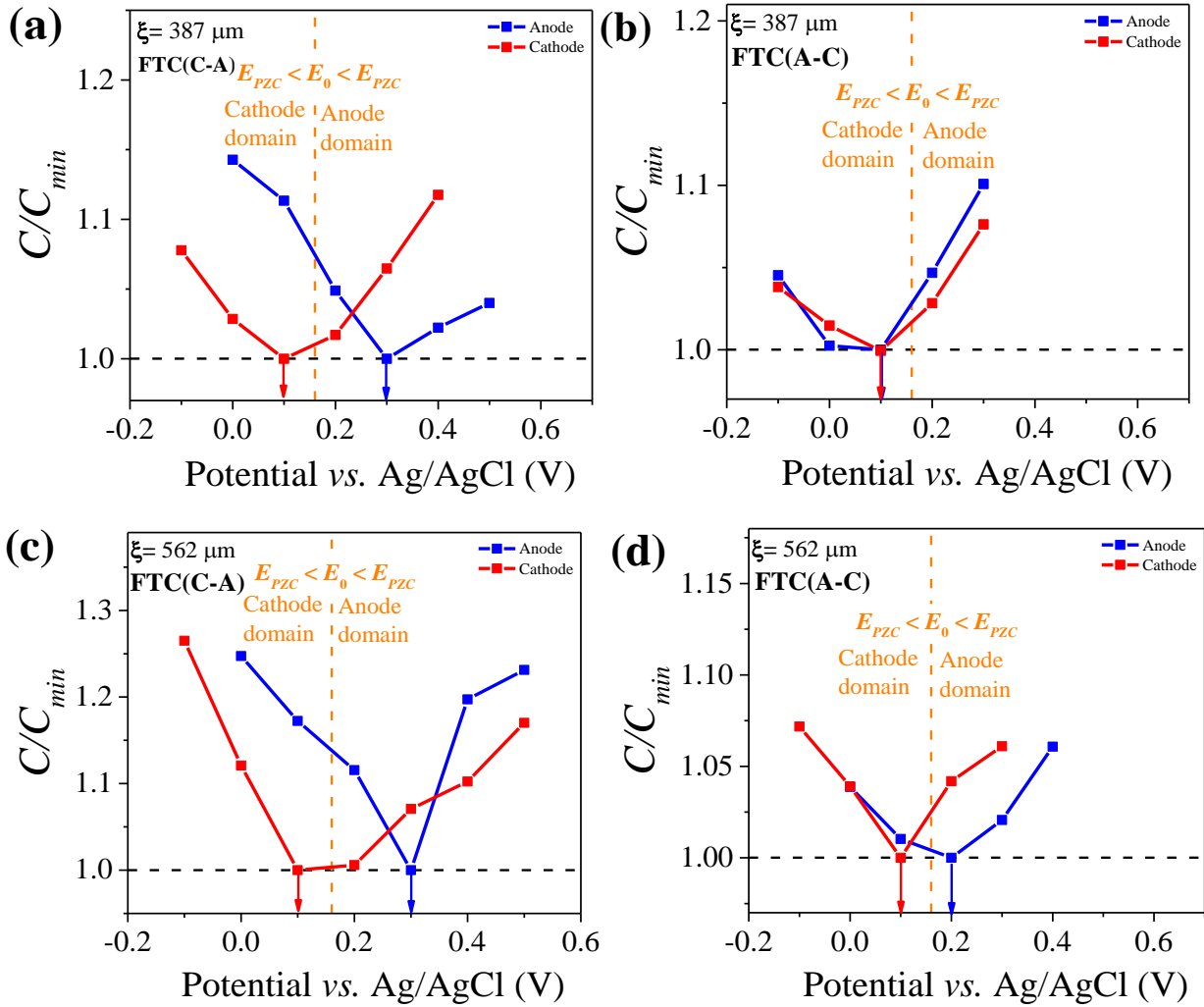
Figure 3.6. E_{PZC} values for anode and cathode after the desalination process for the FTC(C-A) and FTC(A-C) configurations with ξ = 387 µm (**a** and **b**) and ξ = 562 µm (**c** and **d**). Electrolyte: 600 mg L^{-1} NaCl.

Investigation of the effect of thickness (Figure 3.4(a)-(b)) showed that for the FBC, increase of the thickness had a substantial impact, with a 34% decrease of *SAC*, while the electrodes in the FTC were less susceptible to thickness variations. The CV and GCD patterns of the electrodes (Figure 3.7) did not show any clear evidence that thickness influenced the capacitance (C_{CV}) or the ohmic drop (IR_{drop}), indicating that the main phenomenon affecting the electrode performance, related to electrode thickness, was mass transfer limitation from the outer surface of the electrodes to the particles close to the current collector. In the FBC cell, the electrode particles close to the electrolyte flow channel experience a high concentration gradient, while the gradient close to the substrate depends on ion migration in the interstitial pores of the electrode, involving slow diffusive transport. The filled pores accumulating ions in the carbon film can act as an ion barrier to the

deepest pores close to the substrate [34], making them less accessible, or even inaccessible, for ion electrosorption; consequently, the *SAC* decreases as the thickness increases [14]. In contrast, in the FTC cell, the electrode is less liable to mass transfer limitations, since the ions in the interstitial pores are constantly renewed by convective mass transfer promoted by forcing the electrolyte to flow through the pores. In summary, in the case of the FTC architecture, it was possible to overcome the mass transfer limitations observed for thick electrodes in the FBC.
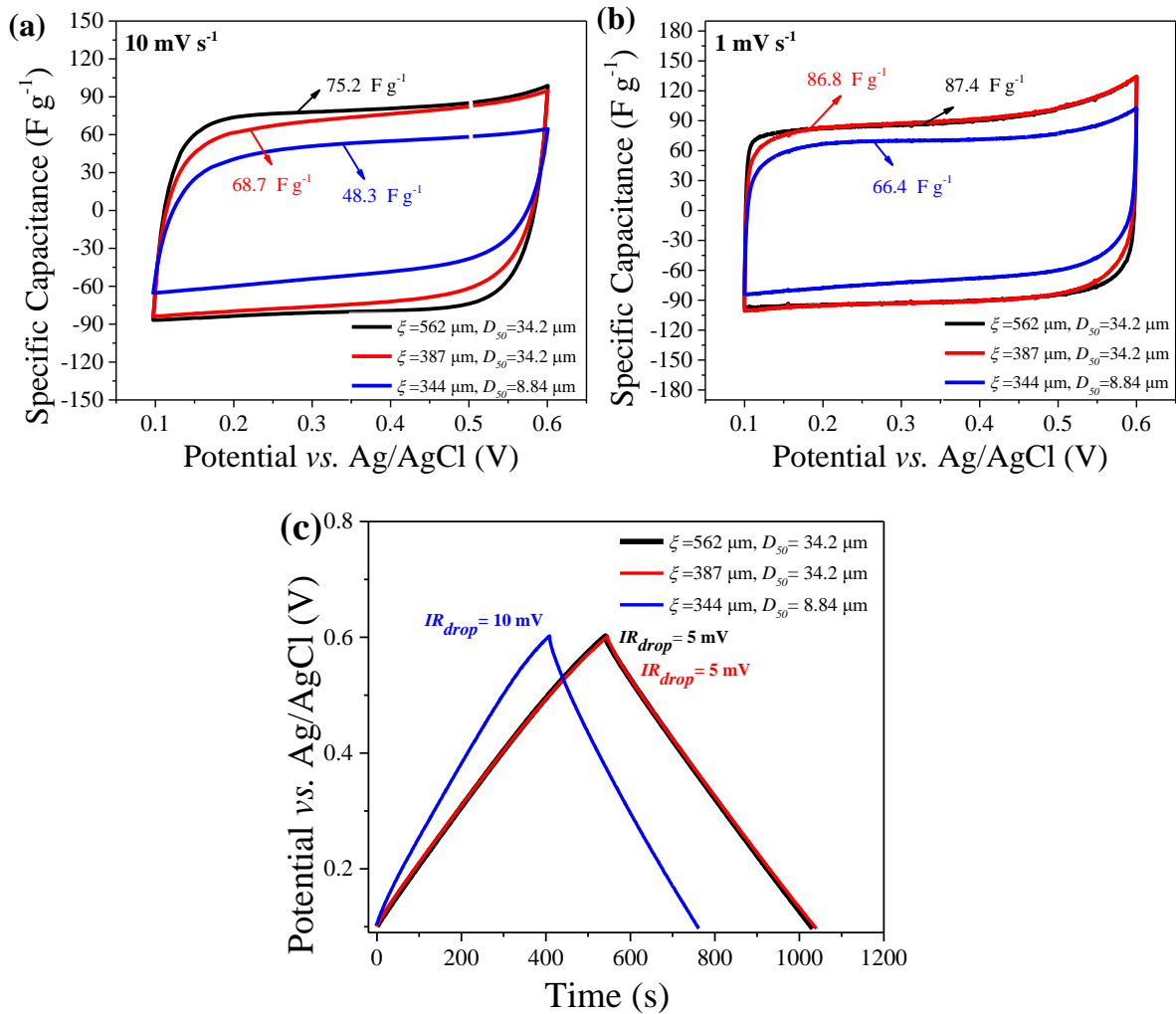
Figure 3.7. Specific capacitance from cyclic voltammograms related to potential and C_{CV} recorded at **(a)** 10 mV s^{-1} and **(b)** 1 mV s^{-1}; **(c)** Galvanostatic charge-discharge (GCD) profiles obtained at 0.1 A g^{-1} (electrolyte: 1 mol L^{-1} NaCl).

The cell architecture and electrode thickness also influenced the electrosorption kinetics, as shown in Table 3.4. Comparing the cell architectures for the electrodes with the same thickness, k_e and k_d were higher for the FTC than for the FBC, regardless of the anode and cathode positions. This outcome could be attributed to the lower mass transfer resistance in the FTC. Using the FBC,

the electrosorption on the thicker electrode was slower, due to the concentration gradient decrease in the inner interstitial pores. An unexpected trend was the slow kinetics observed for the FTC with the thicker electrode, which was ascribed to its lower wettability, since the contact angle ($\theta = 57°$, Figure 3.8) was 87% higher than observed for the thin electrode ($\theta = 31°$). This trend, which was also observed by Barcelos et al. [102], confirmed that the thickness of the electroactive carbon film could also influence the electrode wettability. Furthermore, in the FBC, the electrode hydrophobicity could contribute to slow kinetics by hindering electrolyte percolation and access into the interstitial pores. In conclusion, although the FTC configuration could promote faster kinetics, as in the case of FTC(C-A) (387 μm), the lower *SAC* led to poor performance in terms of *OSR*, when compared with the FBC (421 mg g^{-1} day^{-1}), as shown in Table 3.4.

Table 3.4 Optimized salt removal (*OSR*) for the FBC, FTC(A-C), and FTC(C-A) architectures and different electrode thicknesses. Conditions: batch mode, 600 mg L^{-1} NaCl, $D_{50} = 34.2$ μm.

Cell configuration	ξ (μm)	k_e x 10^3 (s^{-1})	k_d x 10^3 (s^{-1})	$t_{e\text{-}opt}$ (s)	t_d (s)	N_{cycles}	SAC (mg g^{-1})	OSR (mg g^{-1} day^{-1})
FBC	387	2.68	2.64	762	1742	35	14.0	421
FBC	562	1.90	2.15	1025	2145	27	9.3	218
FTC (A-C)	387	2.72	4.29	636	1074	51	9.4	391
FTC (A-C)	562	2.01	3.43	836	1341	40	9.9	320
FTC (C-A)	387	3.10	4.02	600	1146	50	7.3	305
FTC (C-A)	562	2.03	2.88	885	1597	35	7.5	218

k_e and k_d are the pseudo-first order kinetic constants for electrosorption and desorption, respectively; $t_{e\text{-}opt}$ and t_d are the optimized electrosorption and desorption times, respectively; N_{cycles} is the number of cycles.
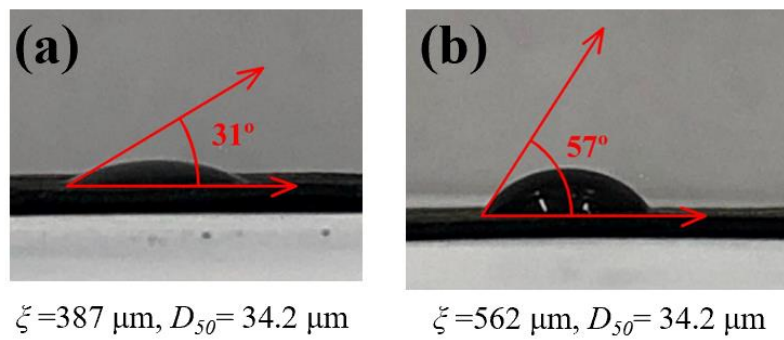
Figure 3.8. Contact angles for PGAC95 electrodes with different thicknesses.

The thin electrodes (ξ = 387 μm) presented higher *OSR*, mainly due to their faster kinetics, except for the FBC, for which the *SAC* value was of crucial importance for achieving the highest *OSR* among all the electrodes and configurations. Considering the substantial influence of mass transfer inside the interstitial pores on the desalination performance, the effect of the diameter of the particles composing the PGAC electrode was investigated, with the aim of improving the mass transfer and, consequently, the electrosorption rate.

The particle size distributions (Figure 3.9) showed that after milling, the median particle diameter (D_{50}) decreased from 34.2 μm to 8.84 μm.
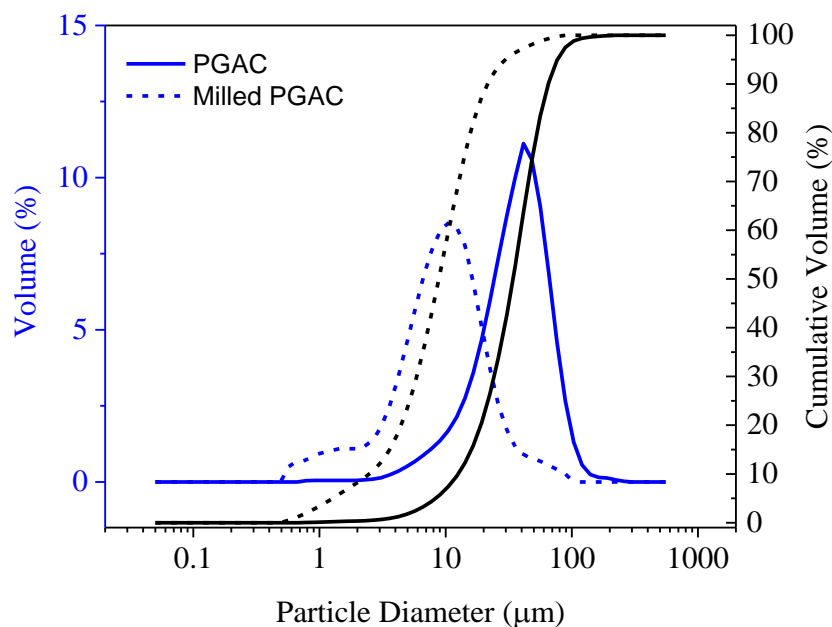
Figure 3.9. Particle size distributions of PGAC (D_{50} = 34.2 μm) and milled PGAC (D_{50} = 8.84 μm).

Figure 3.10(a) shows the performance of the electrodes prepared using different median particle diameters (D_{50}). It can be seen that the particle size affected the desalination performance, with a significant decrease of the *SAC* when the thin particles were used in the FBC and FTC.
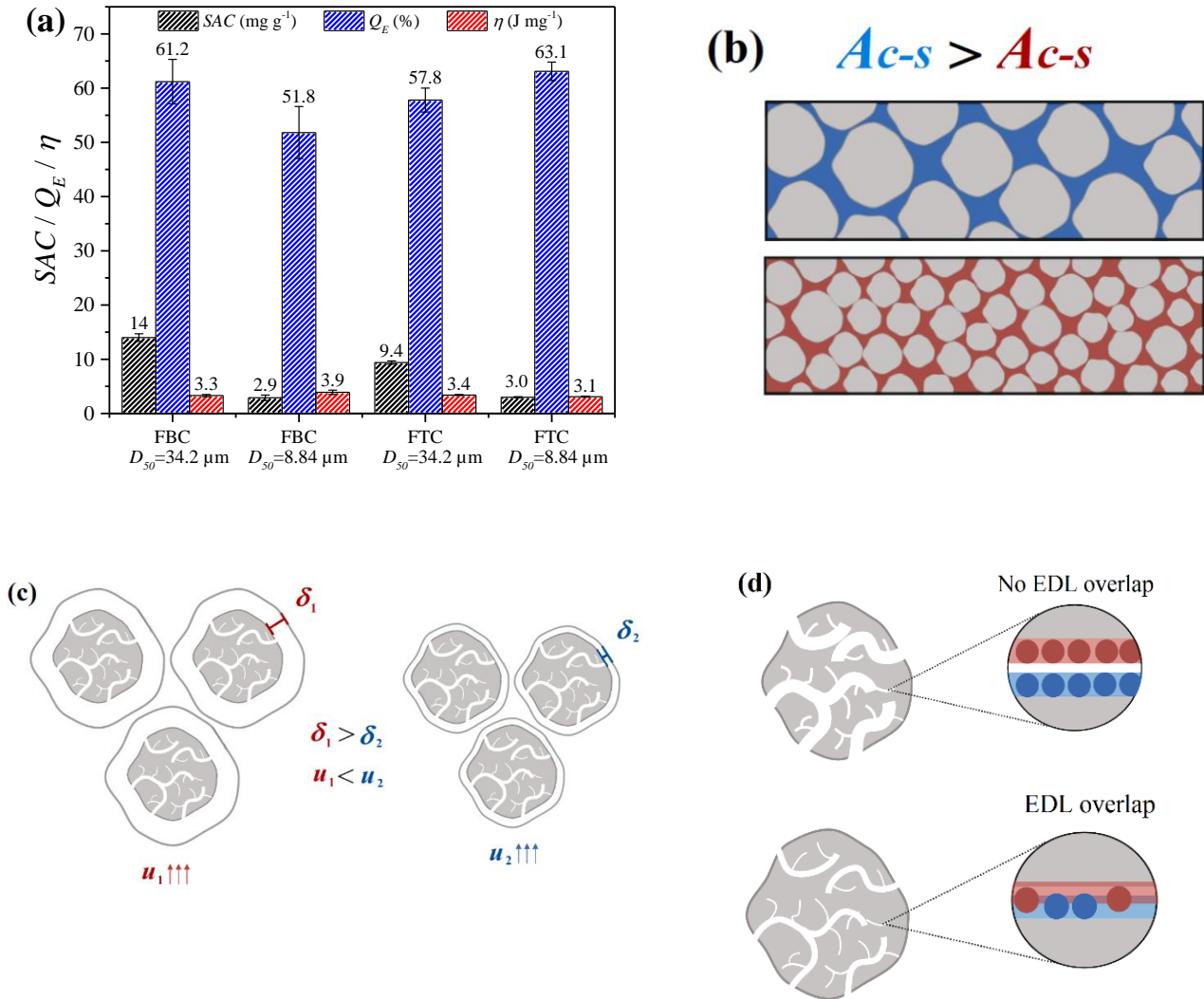
Figure 3.10. (a) Effect of particle diameter on electrode performance using the FBC and the FTC(A-C). Conditions: Batch desalination, 600 mg L^{-1} NaCl. Schematic representations of **(b)** the electrode void and interstitial porosity, **(c)** the effect of flow velocity on the diffusion layer thickness, and **(d)** the EDL overlap inside narrow micropores.

As shown in Table 3.5, the use of thin particles (D_{50} = 8.84 µm) in the FBC and FTC configurations increased the values of k_e and k_d, accelerating the electrosorption and desorption. The smaller particles provided better compaction, decreasing the electrode voids and the interstitial porosity [102]. Consequently, the cross-sectional area available for the electrolyte flow (A_{c-s})

decreased (Figure 3.10(b)), increasing the flow velocity (u) in the interstitial pores and enhancing the inertial forces, promoting turbulence that contributed to improving the external particle mass transfer. Hence, the kinetic improvement could be explained by reduced thickness (δ) of the diffusion film layer [140] in the macropores, shown schematically in Figure 3.10(c), which facilitated mass transfer from the bulk to the mouths of the pores, increasing the concentration gradient at the particle interface, which also enhanced diffusion in the meso- and micropores of the PGAC.

Table 3.5 Effect of particle diameter on desalination kinetics and *OSR*.

D_{50} (μm)	Cell configuration	k_e x 10^3 (s^{-1})	k_d x 10^3 (s^{-1})	$t_{e\text{-}opt}$ (s)	t_d (s)	N_{cycles}	*SAC* (mg g^{-1})	*OSR* (mg g^{-1} day^{-1})
34.2	FBC	2.68	2.64	762	1742	35	14.0	421
8.84	FBC	3.23	4.01	584	1148	50	2.9	123
34.2	FTC (A-C)	2.72	4.29	636	1074	51	9.4	391
8.84	FTC (A-C)	5.80	5.72	352	805	75	3.0	195

Note: k_e and k_d are the pseudo-first order kinetic constants for electrosorption and desorption, respectively; $t_{e\text{-}opt}$ and t_d are the optimized electrosorption and desorption times, respectively; N_{cycles} is the number of cycles.

Despite the faster kinetics using smaller particles, the *SAC* was dramatically reduced by 74% and 68% for the FBC and FTC, respectively, in agreement with the electrochemical characterizations (Figure 3.7) showing their lower capacitance (C_{CV}) and the distinct behavior of these electrodes regarding the ohmic drop (higher IR_{drop}). In order to obtain an explanation for these results, nitrogen physisorption analysis was carried out to investigate whether the milling affected the textural properties of the PGAC (Table 3.6). The adsorption/desorption isotherms (Figure 3.11(a)) showed that the volume adsorbed by the PGAC decreased by 38% after milling; accordingly, the *SSA* was reduced from 1684 to 1465 m^2 g^{-1} (13%). There was also a significant change of the pore size distribution (Figure 3.11(b)), with the percentage of mesopores decreasing from 52.7% to 31.7% after milling (Table 3.6), indicating that the activated carbon became more microporous, which was confirmed by the d_{50} reduction of 23%, from 2.02 nm to 1.55 nm. Hence, besides the *SSA* reduction, the considerable decrease of *SAC* observed using smaller particles could be attributed to both steric hindrance of access of the hydrated ions to subnanometric micropores

and the effect of the electrical double layer overlapping, with the electrostatic layers inside the pores overlapping and losing their electrical capacities [141–143], as illustrated in Figure 3.10(d). In summary, it could be understood from these results that there was an optimum particle diameter that balanced the positive effects of improving the mass transfer rates in the interstitial pores and the negative effects on the textural aspects of the particles, particularly in order to avoid narrow micropores. In this work, the coarse PGAC particles (34.2 μm) were found to be more suitable for preparing the electrodes used for electrosorption.

Table 3.6 Textural properties of PGAC with different median particle diameter (D_{50}).

D_{50} (μm)	SSA_{BET} (m^2 g^{-1})	V_T (cm^3 g^{-1})	V_{mic} (cm^3 g^{-1})	V_{mes} (cm^3 g^{-1})	$\%V_{mes}$	d_{50} (nm)
34.2	1684	0.95	0.45	0.50	52.7	2.02
8.84	1465	0.69	0.47	0.22	31.7	1.55

SSA_{BET}: specific surface area; V_T: total volume of pores; V_{mic}: volume of micropores; V_{mes}: volume of mesopores; $\%V_{mes}$: percentage of mesopores; d_{50}: average pore diameter.
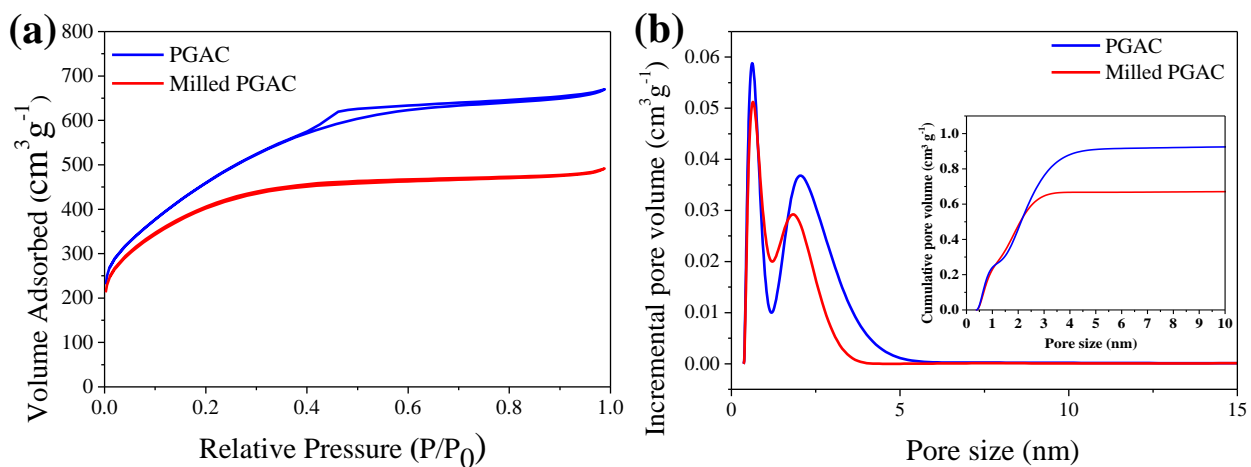
Figure 3.11. Nitrogen adsorption-desorption isotherms **(a)**, and pore size distributions (inset: cumulative pore volumes) **(b)** of PGAC and milled PGAC.

Considering the high *SAC* and Q_E and low η obtained using the FBC, and the fast kinetics provided by the FTC, the investigation of a new cell architecture was proposed, denoted the percolation flow cell (PFC), with the aim of combining the beneficial aspects of the two cell architectures studied previously. Similar to the FBC, in the PFC the flow direction is perpendicular to the electric field, but the electrolyte is forced to percolate through the carbon film, similarly to

the FTC, but with a longer contact time with the electrode, as shown in Figure 3.12(a). The results obtained using the PFC are displayed in Figure 3.12(b), together with the performance obtained using the FBC and FTC, for comparison. Use of the PFC resulted in an increase of the *SAC*, while Q_E and η remained similar to the values observed for the FBC and FTC, respectively. Together with the *SAC* enhancement, the greatest improvement was observed for the *OSR* (1135 mg g^{-1} day^{-1}), which could be attributed to the faster mass transfer promoted by the permeation of the electrolyte through the carbon film, which mainly enhanced the desorption kinetics (Table 3.7).
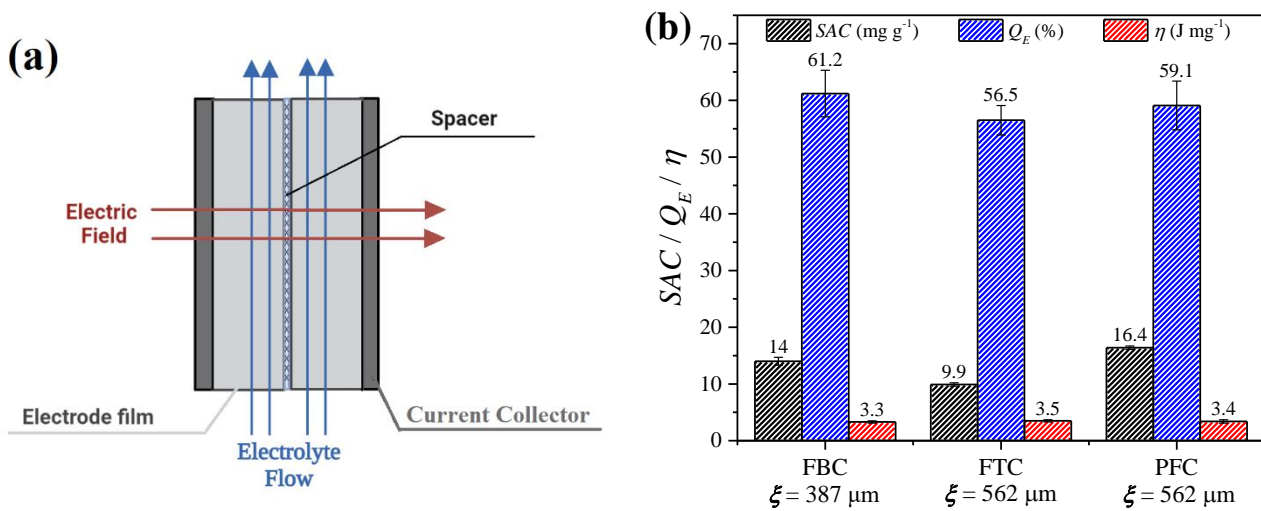
Figure 3.12. (a) Schematic representation of the electrolyte flow and electric field directions in the PFC. **(b)** Comparison of the best desalination performances for the FBC, FTC(A-C), and PFC architectures. Conditions: batch desalination, 600 mg L^{-1} NaCl, and $D_{50} = 34.2$ μm.

Table 3.7 Optimized salt removal (*OSR*) for the different cell configurations. Conditions: batch desalination, 600 mg L^{-1} NaCl, and $D_{50} = 34.2$ μm.

Cell configuration	ξ (μm)	k_e x 10^3 (s^{-1})	k_d x 10^3 (s^{-1})	$t_{e\text{-}opt}$ (s)	t_d (s)	N_{cycles}	SAC (mg g^{-1})	OSR (mg g^{-1} day^{-1})
FBC	387	2.68	2.64	762	1742	35	14.0	421
FTC(A-C)	562	2.01	3.43	836	1341	40	9.9	320
PFC	562	2.61	10.9	457	421	98	16.6	1135

k_e and k_d are the pseudo-first order kinetic constants for electrosorption and desorption, respectively; $t_{e\text{-}opt}$ and t_d are the optimized electrosorption and desorption times, respectively; N_{cycles} is the number of cycles.

3.3.2 Percolation cell: single-pass desalination under galvanostatic conditions

In order to investigate the PFC under more realistic conditions, in single-pass and galvanostatic mode, the desalination was performed using the best electrode configuration found previously (ξ = 562 μm, D_{50} = 34.2 μm). As shown in Figure 3.13(a), under the single-pass condition, the performance obtained for potentiostatic operation of the PFC greatly exceeded that achieved under batch conditions, exhibiting *SAC* of 27.8 mg g^{-1} and Q_E of 74.0%, at 1.2 V, which were approximately 70% and 25% higher, respectively, than observed for batch operation (Figure 3.12(b)). Besides the increases of the concentration gradient and the mass transfer rate achieved with the PFC configuration, the high *SAC* obtained could be attributed to the increase of Q_E due to the slow volumetric flow rate, leading to a longer retention time and sufficient time for the diffusion of ions into the micropores, consequently improving the electrosorption. This was evidenced by the longer time of 900 s required for desorption, compared to the desorption time of only 421 s in the batch mode, suggesting that the micropores had been filled.
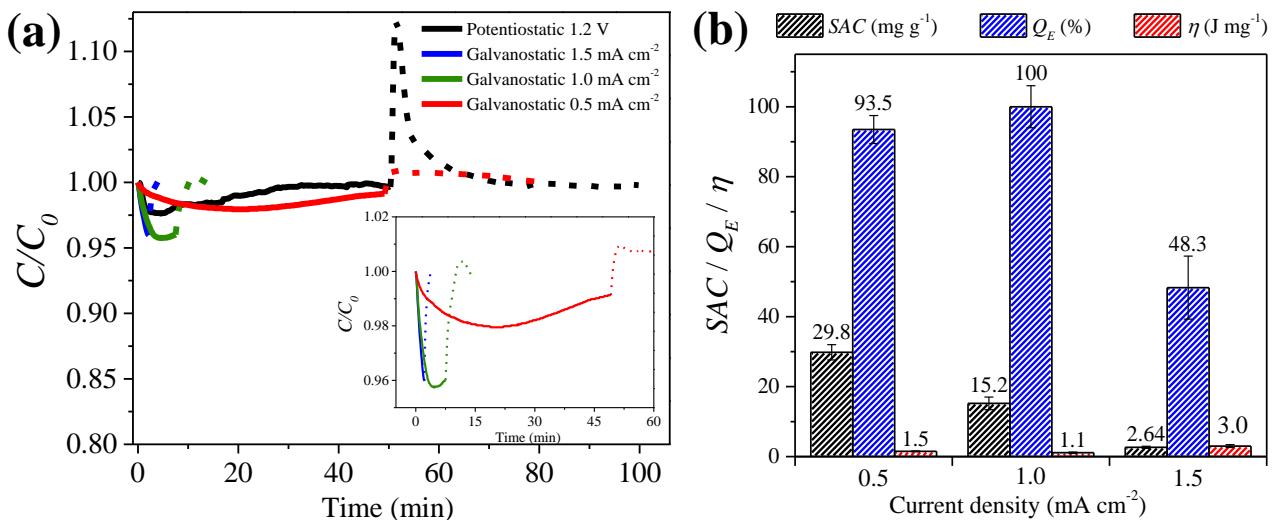
Figure 3.13. **(a)** Normalized concentration plotted against time for the potentiostatic and galvanostatic desalination processes, where the solid and dashed lines represent the electrosorption and desorption steps, respectively. The inset shows the effect of current density. **(b)** Desalination performance applying different current densities. Conditions: 1000 mg L^{-1} NaCl; flow rate of 10 mL min^{-1}; E_{cc} of 1.2 V and 0.0 V for electrosorption and desorption, respectively. The electrosorption and desorption current densities had the same values, but opposite sign.

The galvanostatic mode has been identified as being most energy-efficient for electrochemical desalination, although with lower *SAC* than observed for potentiostatic operation

[136,144,145]. As shown in Figure 3.13(b), except for 0.5 mA cm^{-2}, the values of *SAC* and η were lower than obtained under the potentiostatic condition (16.6 mg g^{-1}, 3.4 J mg^{-1}), which could be explained by the lower cell voltage and reduced energy dissipation through the resistive components of the cell [136,145]. The typical potentiostatic operational profile obtained (Figure 3.13(a)) showed an initial rapid concentration depletion, followed by slow uptake until electrode saturation. When the polarization was reversed in the desorption step, fast release of the ions was observed. On the other hand, use of the galvanostatic mode enabled a constant outlet concentration to be maintained up to the E_{cc}, which would be an advantage in the continuous production of desalinated water.

The effect of current density on the electrosorption/desorption profile is detailed in the inset of Figure 3.13(a). Due to the strong electrostatic force, a higher current density is associated with faster electrosorption and desorption rates. The E_{cc} is also reached more rapidly, due to the fast EDL charging, leading to short desalination cycles, which could in principle be attractive in terms of *OSR*. However, for galvanostatic operation (Table 3.8), consideration should be given to the tradeoff between N_{cycle} and *SAC*, as in the case of the desalination at 1.5 mA cm^{-2}, where despite the 343 cycles, the *SAC* was only 2.64 mg g^{-1} and, consequently, the *OSR* was 906 mg g^{-1} day^{-1}. The lower *SAC* obtained at high current densities could be explained by the slow kinetics of mass transfer in the micropores, which hindered the electrosorption because E_{cc} was reached rapidly, leading to poor charging efficiency and, consequently, high values of η (Figure 3.13(b)). In contrast, the use of low current densities would lead to slow charging of the EDL and higher *SAC* would be expected. Accordingly, the application of 0.5 mA cm^{-2} resulted in Q_E of 93.5% and achievement of high *SAC* (29.8 mg g^{-1}). However, the cycle time was greatly extended and N_{cycle} was significantly reduced, resulting in the lowest observed *OSR* (507 mg g^{-1} day^{-1}). This reinforces the importance of simultaneous analysis of the kinetics and the electrosorption/desorption capacity, in order to establish not only the best material for CDI [45,56], but also the best condition for operation of the CDI device. In the present case, 1.0 mA cm^{-2} was the best current density for operation of the PFC, since 100% charging efficiency and the lowest value of η (1.1 J mg^{-1}) were achieved, despite the fact that the *SAC* (15.2 mg g^{-1}) was not the highest observed.

Table 3.8 Optimized salt removal (*OSR*) for desalination using potentiostatic and galvanostatic modes.

Mode	Cell potential (V) or current density (mA cm^{-2})	Flow rate (mL min^{-1})	t_e' (min)	t_d' (min)	N_{cycle}	SAC (mg g^{-1})	OSR (mg g^{-1} day^{-1})
Potentiostatic	1.2	10	19.2*	12.3*	46	27.8	1279
Galvanostatic	0.5	10	50.2	32.9	17	29.8	507
Galvanostatic	1.0	10	7.90	6.78	98	15.2	1490
Galvanostatic	1.5	10	2.20	2.00	343	2.64	906
Galvanostatic	1.0	7	11.1	9.04	71	23.4	1661
Galvanostatic	1.0	13	5.80	4.80	136	9.6	1306

*Time required to achieve C/C_0 of 0.99 (electrosorption) or 1.01 (desorption).

In order to further improve the *SAC* and provide a longer residence time for electrosorption, the effect of flow rate was investigated. The results (Figure 3.14(a)) showed the effect of the flow rate on the concentration depletion and the operational time. A faster flow rate shortened the cycle time, but the quantity of ions removed decreased, due to mass transfer restrictions, especially regarding the access of the ions to the micropores. On the other hand, a low flow rate could be a good strategy for improving the desalination performance. As shown in Figure 3.14(b), the *SAC* increased from 15.2 mg g^{-1} at 10 mL min^{-1} to 23.4 mg g^{-1} at 7.0 mL min^{-1}, with a simultaneous decrease of η, which are remarkable outcomes for a membrane-less cell. It is also worth noting that in all cases, the charging efficiency at 1.0 mA cm^{-2} was 100%, so the *SAC* enhancement could not be attributed to the EDL charging improvements, but solely to the more effective access of the ions into the micropores, due to the longer retention times. Despite the remarkable *SAC*, the use of slow flow rates had a major impact on the cycle time, so in order to establish the best operational condition, the electrosorption and desorption times (Table 3.8) must be taken into account in the analysis.
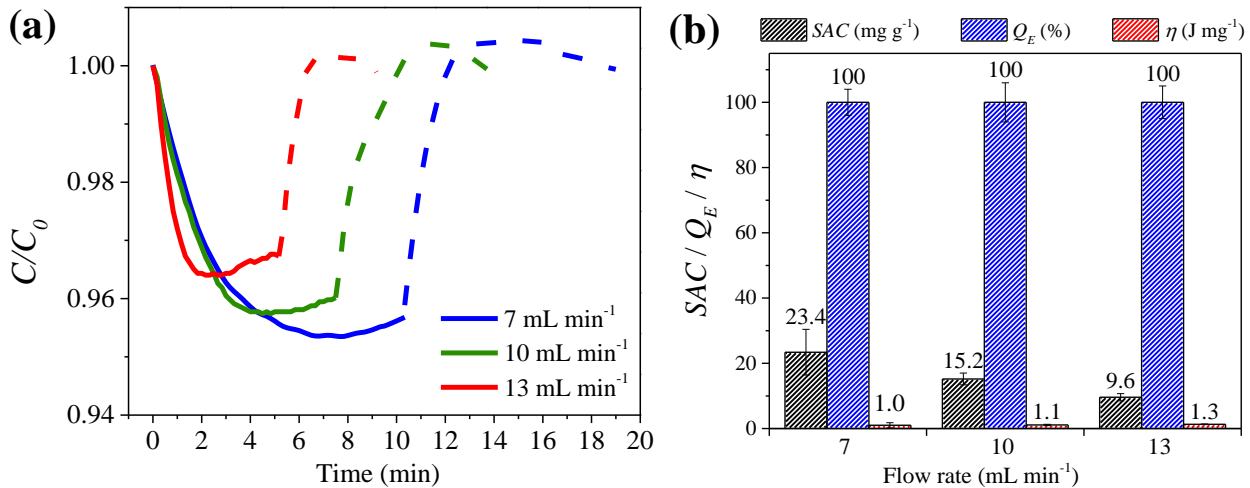
Figure 3.14. Plots of **(a)** normalized concentration against time, and **(b)** desalination performance, for different volumetric flow rates. The solid and dashed lines represent the electrosorption and desorption steps, respectively. Conditions: 1000 mg L^{-1} NaCl; electrosorption and desorption current densities of 1.0 and -1.0 mA cm^{-2}, respectively; E_{cc} of 1.2 V and 0.0 V for electrosorption and desorption, respectively.

The *OSR* values (Table 3.8), calculated considering the time required to reach E_{cc} of 1.2 V and 0.0 V during the electrosorption (t_e') and desorption (t_d'), respectively, revealed that the best desalination rate was 1661 mg g^{-1} day^{-1}, achieved applying 1.0 mA cm^{-2} and 7 mL min^{-1}. In this case, the lower N_{cycle} obtained at 7 mL min^{-1} was compensated by the higher *SAC*. This highlighted that although desalination is faster using high current density and flow rate, such conditions would not be recommended for obtaining high productivity of desalinated water. In summary, the optimum operational condition must be established by simultaneous analysis of both *SAC* and cycle time.

Regarding the flow conditions, a high pressure drop of 0.12 bar cm^{-1} (at 7 mL min^{-1}) was measured along the flow path in the PFC, which would be a challenge in scale-up of this cell configuration.

Finally, a comparison of *OSR* using the PGAC electrodes in the PFC with other activated carbon electrodes operating under similar conditions is presented in Table 3.9. The value obtained for PGAC/CDI (1661 mg g^{-1} day^{-1}) was higher than reported for most of the carbon electrodes, except for the value obtained by Choi and Yoon [18] (2072 mg g^{-1} day^{-1}) using MCDI, for which the use of membranes imposes an additional investment cost.

Table 3.9 *OSR* for CDI desalination using carbon electrodes.

Electrode material	NaCl (mg L^{-1})	Current density (mA cm^{-2})	Flow rate (mL min^{-1})	SAC (mg g^{-1})	OSR (mg g^{-1} day^{-1})	Reference
Activated carbons (GF-AC)	2045	0.67	70	1.8	37.8	Lado et al. [146]
Activated carbons (GF-AC)	2045	0.67	130	2.2	41.8	Lado et al. [146]
Activated carbons (GF-AC)	2045	0.67	200	4.2	50.4	Lado et al. [146]
Activated carbon fiber+PVDF	585	0.375	10	3.45	100	Chen et al. [147]
Activated carbon powder	1000	1.43	30	15.7	2072*	Choi and Yoon [18]
MSP20 carbon	585	2.5	10	11.2	1401	Kang et al. [145]
PGAC	1000	1.0	7	23.4	1661	This study

Note: Galvanostatic and single pass operation. *MCDI.

3.4 Conclusions

The CDI cell architecture and flow pattern can influence operational parameters that are crucial in determining desalination performance. The hydrodynamics influences the mass transfer phenomena and the kinetics of the desalination process, depending on the cell architecture regarding the flow and electric field directions. For thin electrodes, the FBC outperforms the FTC, due to the lower R_{CT} and higher A_0. On the other hand, use of the FTC is an effective strategy for overcoming the mass transfer limitations observed in the FBC, especially for thicker electrodes that impose sharp concentration gradients within the porous PGAC film, due to the slow mass transfer rates. Despite the fast kinetics, the desalination performance observed for the FTC did not exceed that of the FBC. The findings of this study also provide insights into the role of electrode particle size. Although small particles improve the desalination rate by promoting faster mass transfer in the pore interstices, due to increased interstitial flow velocity and turbulence, a substantial reduction of the *SAC* occurs as a consequence of the changes in the textural properties of the PGAC (reductions of *SSA*, *%V$_{mes}$*, and *d$_{50}$*). The pore shrinkage leads to steric hindrance of the transfer of hydrated ions to

sub-nanometric micropores, as well as electrical double layer overlapping, resulting in poor electrosorption capacity.

In an attempt to improve CDI performance, a new PFC architecture was investigated under batch conditions, resulting in an *OSR* (1135 mg g^{-1} day^{-1}) approximately 170% superior to that obtained with the FBC (421 mg g^{-1} day^{-1}), which was mainly a consequence of the higher mass transfer rates related to the hydrodynamics of this cell. Given this promising outcome, the PFC was also investigated using single-pass mode, which provided a further increase of the *OSR* (1279 mg g^{-1} day^{-1}), since single-pass operation led to longer retention times, allowing sufficient time for the ions to diffuse and fill the inner micropores.

In order to evaluate the desalination process under more realistic conditions, investigation was made of single-pass and galvanostatic operation. It was found that the optimum current density should be selected considering the tradeoff between the *SAC* and the cycle time. The results also evidenced that although high current density and flow rate make desalination faster, such conditions would not be recommended for obtaining high productivity of desalinated water. The best desalination rate was 1661 mg g^{-1} day^{-1}, achieved applying 1.0 mA cm^{-2} and 7.0 mL min^{-1}. Despite all the beneficial features of the PFC, the pressure drop in this cell design remains an important challenge to be addressed in future work.

4 CHAPTER
CONCLUSIONS AND SUGGESTIONS FOR FUTURE WORKS

This study showed that is possible to prepare activated carbon electrodes using the polymer from residual glycerol as a precursor. This material showed to be a promising low-cost sustainable material for CDI, since high value of *SAC* and stable performance over 50 electrosorption/desorption cycles were obtained. Long-term stability is a paramount parameter for the effective application of activated carbons in CDI. The control of E_{cell} to avoid anode surpassing the oxidation potential limit revealed to be crucial for stable desalination performance over long-term desalination. Moreover, maintaining the potential of zero charge of the negative and positive electrodes outside their working domains during the cycles demonstrated to be an efficient strategy to minimize the deleterious effect of co-ion repulsion, resulting in enhanced desalination performance. The PGAC use with symmetrical configuration (1.2 V) and MCDI (1.6 V), which provided *SAC* values of 14.2 and 27.1 mg g^{-1}, respectively, could enable a low-cost water treatment system using the CDI technology.

The importance of cell architecture and flow patterns to improve the mass transfer, and consequently, *OSR* value was also evidenced. Regarding the thinner electrode, the lower R_{CT} and higher A_0 of FBC boosted the electrosorption performance compared to FTC. However, for the thicker electrode, the FTC avoids the *SAC* decrease observed for FBC since the convective flow in the interstitial pores can minimize the external mass transfer resistance, thus promoting faster electrosorption kinetics. The particle size showed to be crucial for electrochemical desalination. The small particles obtained after milling enhance the electrode mass transfer and, consequently, the desalination kinetics, in agreement with the mass transfer film theory, the lower *SSA* and the presence of narrow micropores reduced dramatically the *SAC*, probably due to the steric hindrance of the hydrated ions to the subnanometric micropores and the effect of electrical double-layer overlapping. Therefore, an optimum particle diameter must be taken into account to achieve faster kinetics and high *SAC* values. The results encouraged the investigation of a new cell, the PFC, which demonstrated a remarkable improvement of the *OSR* value, an outcome attributed to the combination of enhanced mass transfer, promoted by the permeation of the electrolyte through the electrode, and longer contact time between electrolyte and electrode. Under more realistic conditions (quasi single-pass and galvanostatic mode) the PFC was applied, and the results showed

the importance of the tradeoff between the *SAC* and the cycle time since the higher current density and flow rate obtained fast kinetics but decreased the cycle time, which diminish the *OSR*. The results showed the optimum conditions to obtain high productivity of desalinated water is 1.0 mA cm^{-2} and 7.0 mL min^{-1}, conditions where it was possible to achieve the higher value of *OSR* (1661 mg g^{-1} day^{-1}) than the values reported in CDI literature. This study revealed the effects of the cell design on mass transfer phenomena, bringing insights into the role of particle size, electrode thickness, and operational conditions.

4.1 Suggestions for future works

Novel low-cost PGAC and the effects of the cell design on mass transfer phenomena were investigated in this study, and new insights on the electrode stability, role of particle size, electrode thickness, and operational conditions have been achieved in this thesis. However, other studies must be carried out to further improve and optimize the CDI technology, especially for large-scale applications. In this regard, the following suggestions are proposed for future works:

- Explore other applications for PGAC electrodes, such as water softening, heavy metal removal, and nutrient recovery;
- A systematic study to identify the optimized particle size of activated carbon to be applied in the electrode preparation considering the effects of mass transfer rates in the interstitial pores and the effects on the textural aspects;
- Development of a larger scale percolation flow cell aiming for high production of brackish water;
- Study of the effects of pressure drop for a larger scale percolation flow cell;
- Better understanding of how ions competition influences water softening and desalination processes considering a multi-component solution;
- Investigation of techniques to optimize water-recovery;
- Technical-economic feasibility study of PGAC application in CDI desalination;

5   REFERENCES

[1]   M.A. Shannon, P.W. Bohn, M. Elimelech, J.G. Georgiadis, B.J. Marĩas, A.M. Mayes, Science and technology for water purification in the coming decades, Nature. 452 (2008) 301–310. doi:10.1038/nature06599.

[2]   S. Porada, R. Zhao, A. Van Der Wal, V. Presser, P.M. Biesheuvel, Review on the science and technology of water desalination by capacitive deionization, Prog. Mater. Sci. 58 (2013) 1388–1442. doi:10.1016/j.pmatsci.2013.03.005.

[3]   M.A. Anderson, A.L. Cudero, J. Palma, Capacitive deionization as an electrochemical means of saving energy and delivering clean water. Comparison to present desalination practices: Will it compete?, Electrochim. Acta. 55 (2010) 3845–3856. doi:10.1016/j.electacta.2010.02.012.

[4]   M. Mossad, W. Zhang, L. Zou, Using capacitive deionisation for inland brackish groundwater desalination in a remote location, Desalination. 308 (2013) 154–160. doi:10.1016/j.desal.2012.05.021.

[5]   J.R. Du, X. Zhang, X. Feng, Y. Wu, F. Cheng, M.E.A. Ali, Desalination of high salinity brackish water by an NF-RO hybrid system, Desalination. 491 (2020) 114445. doi:10.1016/j.desal.2020.114445.

[6]   V.B. Brião, J. Magoga, M. Hemkemeier, E.B. Brião, L. Girardelli, L. Sbeghen, D.P.C. Favaretto, Reverse osmosis for desalination of water from the Guarani Aquifer System to produce drinking water in southern Brazil, Desalination. 344 (2014) 402–411. doi:10.1016/j.desal.2014.04.008.

[7]   G.D.P. da Silva, M.H. Sharqawy, Techno-economic analysis of low impact solar brackish water desalination system in the Brazilian Semiarid region, J. Clean. Prod. 248 (2020) 119255. doi:10.1016/j.jclepro.2019.119255.

[8]   E. Jones, M. Qadir, M.T.H. van Vliet, V. Smakhtin, S. mu Kang, The state of desalination and brine production: A global outlook, Sci. Total Environ. 657 (2019) 1343–1356.

doi:10.1016/j.scitotenv.2018.12.076.

[9]   B. Van der Bruggen, C. Vandecasteele, Distillation vs. membrane filtration: Overview of process evolutions in seawater desalination, Desalination. 143 (2002) 207–218. doi:10.1016/S0011-9164(02)00259-X.

[10]   R. Semiat, Critical Review Energy Issues in Desalination Processes, Am. Chem. Soc. 42 (2008) 8193–8201.

[11]   T. Younos, K.E. Tulou, Overview of Desalination Techniques, J. Contemp. Water Res. Educ. 132 (2005) 3–10. doi:10.1111/j.1936-704x.2005.mp132001002.x.

[12]   K.P. Lee, T.C. Arnot, D. Mattia, A review of reverse osmosis membrane materials for desalination-Development to date and future potential, J. Memb. Sci. 370 (2011) 1–22. doi:10.1016/j.memsci.2010.12.036.

[13]   A. Al-Karaghouli, L.L. Kazmerski, Energy consumption and water production cost of conventional and renewable-energy-powered desalination processes, Renew. Sustain. Energy Rev. 24 (2013) 343–356. doi:10.1016/j.rser.2012.12.064.

[14]   R.L. Zornitta, J.J. Lado, M.A. Anderson, L.A.M. Ruotolo, Effect of electrode properties and operational parameters on capacitive deionization using low-cost commercial carbons, Sep. Purif. Technol. 158 (2016) 39–52. doi:10.1016/j.seppur.2015.11.043.

[15]   E. García-Quismondo, C. Santos, J. Lado, J. Palma, M.A. Anderson, Optimizing the energy efficiency of capacitive deionization reactors working under real-world conditions, Environ. Sci. Technol. 47 (2013) 11866–11872. doi:10.1021/es4021603.

[16]   C. Tan, C. He, J. Fletcher, T.D. Waite, Energy recovery in pilot scale membrane CDI treatment of brackish waters, Water Res. 168 (2020) 115146. doi:10.1016/j.watres.2019.115146.

[17]   W. Zhang, M. Mossad, L. Zou, A study of the long-term operation of capacitive deionisation in inland brackish water desalination, Desalination. 320 (2013) 80–85. doi:10.1016/j.desal.2013.04.010.

[18]   J.H. Choi, D.J. Yoon, A stable operation method for membrane capacitive deionization

systems without electrode reactions at high cell potentials, Water Res. 157 (2019) 167–174. doi:10.1016/j.watres.2019.03.083.

[19] W. Tang, J. Liang, D. He, J. Gong, L. Tang, Z. Liu, Various cell architectures of capacitive deionization : Recent advances and future trends, Water Res. 150 (2019) 225e251 Contents. doi:10.1016/j.watres.2018.11.064.

[20] J.W. Blair, G.W. Murphy, Electrochemical Demineralization of Water with Porous Electrodes of Large Surface Area, Am. Chem. Soc. (1960) 206–223. doi:10.1021/ba-1960-0027.ch020.

[21] Johnson A.M., Venolia A.W., Wilbourne, Newman, Wong, Gillam, Jonhson, Horowitz, The Electrosorb Process for Desalting Water, Washingt. U.S. Dept. Inter. (1970).

[22] A.M. Johnson, J. Newman, Desalting by Means of Porous Carbon Electrodes, J. Electrochem. Soc. 118 (1971) 510–517. doi:10.1149/1.2408094.

[23] X. Su, A. Kushima, C. Halliday, J. Zhou, J. Li, T.A. Hatton, Electrochemically-mediated selective capture of heavy metal chromium and arsenic oxyanions from water, Nat. Commun. 9 (2018). doi:10.1038/s41467-018-07159-0.

[24] Z. Du, W. Tian, K. Qiao, J. Zhao, L. Wang, W. Xie, M. Chu, T. Song, Improved chlorine and chromium ion removal from leather processing wastewater by biocharcoal-based capacitive deionization, Sep. Purif. Technol. 233 (2020) 116024. doi:10.1016/j.seppur.2019.116024.

[25] E. Liu, L.Y. Lee, S.L. Ong, H.Y. Ng, Treatment of industrial brine using capacitive deionization (CDI) towards zero liquid discharge – challenges and optimization, Water Res. 183 (2020) 116059. doi:10.1016/j.watres.2020.116059.

[26] P.M. Biesheuvel, R. Zhao, S. Porada, A. van der Wal, Theory of membrane capacitive deionization including the effect of the electrode pore space, J. Colloid Interface Sci. 360 (2011) 239–248. doi:10.1016/j.jcis.2011.04.049.

[27] R.L. Zornitta, K.M. Barcelos, F.G.E. Nogueira, L.A.M. Ruotolo, Understanding the mechanism of carbonization and KOH activation of polyaniline leading to enhanced electrosorption performance, Carbon N. Y. 156 (2020) 346–358. doi:10.1016/j.carbon.2019.09.058.

[28] J.J. Lado, R.L. Zornitta, I.V. Rodríguez, K.M. Barcelos, L.A.M. Ruotolo, Sugarcane Biowaste-Derived Biochars as Capacitive Deionization Electrodes for Brackish Water Desalination and Water-Softening Applications, ACS Sustain. Chem. Eng. 7 (2019) 18992−19004 Research. doi:10.1021/acssuschemeng.9b04504.

[29] A. Omosebi, X. Gao, J. Landon, K. Liu, Asymmetric electrode configuration for enhanced membrane capacitive deionization, ACS Appl. Mater. Interfaces. 6 (2014) 12640–12649. doi:10.1021/am5026209.

[30] X. Gao, A. Omosebi, J. Landon, K. Liu, Enhanced Salt Removal in an Inverted Capacitive Deionization Cell Using Amine Modified Microporous Carbon Cathodes, Environ. Sci. Technol. 49 (2015) 10920–10926. doi:10.1021/acs.est.5b02320.

[31] X. Gao, S. Porada, A. Omosebi, K.L. Liu, P.M. Biesheuvel, J. Landon, Complementary surface charge for enhanced capacitive deionization, Water Res. 92 (2016) 275–282. doi:10.1016/j.watres.2016.01.048.

[32] J.J. Lado, R.L. Zornitta, F.A. Calvi, M. Martins, M.A. Anderson, F.G.E. Nogueira, L.A.M. Ruotolo, Enhanced capacitive deionization desalination provided by chemical activation of sugar cane bagasse fly ash electrodes, J. Anal. Appl. Pyrolysis. 126 (2017) 143–153. doi:10.1016/j.jaap.2017.06.014.

[33] R.L. Zornitta, P. Srimuk, J. Lee, B. Krener, M. Aslan, L.A.M. Ruotolo, V. Presser, Charge and Potential Balancing for Optimized Capacitive Deionization Using Lignin-Derived , Low-Cost Activated Carbon Electrodes, ChemSusChem. 11 (2018) 2101–2113. doi:10.1002/cssc.201800689.

[34] C. Zhang, D. He, J. Ma, W. Tang, T.D. Waite, Comparison of faradaic reactions in fl ow-through and fl ow-by capacitive deionization (CDI) systems, Electrochim. Acta. 299 (2019) 727–735. doi:10.1016/j.electacta.2019.01.058.

[35] Y. Algurainy, D.F. Call, Asymmetrical removal of sodium and chloride in flow-through capacitive deionization, Water Res. 183 (2020) 116044. doi:10.1016/j.watres.2020.116044.

[36] F. Duan, X. Du, Y. Li, H. Cao, Y. Zhang, Desalination stability of capacitive deionization using ordered mesoporous carbon: Effect of oxygen-containing surface groups and pore

properties, Desalination. 376 (2015) 17–24. doi:10.1016/j.desal.2015.08.009.

[37] D. He, C.E. Wong, W. Tang, P. Kovalsky, T. David Waite, Faradaic Reactions in Water Desalination by Batch-Mode Capacitive Deionization, Environ. Sci. Technol. Lett. 3 (2016) 222–226. doi:10.1021/acs.estlett.6b00124.

[38] P.M. Biesheuvel, A. van der Wal, Membrane capacitive deionization, J. Memb. Sci. 346 (2010) 256–262. doi:10.1016/j.memsci.2009.09.043.

[39] Y.J. Kim, J.H. Choi, Enhanced desalination efficiency in capacitive deionization with an ion-selective membrane, Sep. Purif. Technol. 71 (2010) 70–75. doi:10.1016/j.seppur.2009.10.026.

[40] R. Zhao, P.M. Biesheuvel, A. Van Der Wal, Energy consumption and constant current operation in membrane capacitive deionization, Energy Environ. Sci. 5 (2012) 9520–9527. doi:10.1039/c2ee21737f.

[41] R.L. Zornitta, L.A.M. Ruotolo, Simultaneous analysis of electrosorption capacity and kinetics for CDI desalination using different electrode configurations, Chem. Eng. J. 332 (2018) 33–41. doi:10.1016/j.cej.2017.09.067.

[42] S. Porada, L. Weinstein, R. Dash, A. van der Wal, M. Bryjak, Y. Gogotsi, P.M. Biesheuvel, Water desalination using capacitive deionization with microporous carbon electrodes., ACS Appl. Mater. Interfaces. 4 (2012) 1194–1199. doi:10.1021/am201683j.

[43] X. Gao, A. Omosebi, J. Landon, K. Liu, Surface charge enhanced carbon electrodes for stable and efficient capacitive deionization using inverted adsorption-desorption behavior, Energy Environ. Sci. 8 (2015) 897–909. doi:10.1039/c4ee03172e.

[44] K.C. Leonard, J.R. Genthe, J.L. Sanfilippo, W.A. Zeltner, M.A. Anderson, Synthesis and characterization of asymmetric electrochemical capacitive deionization materials using nanoporous silicon dioxide and magnesium doped aluminum oxide, Electrochim. Acta. 54 (2009) 5286–5291. doi:10.1016/j.electacta.2009.01.082.

[45] K.M. Barcelos, K.S.G.C. Oliveira, D.S.A. Silva, E.A. Urquieta-González, L.A.M. Ruotolo, Efficient and stable operation of capacitive deionization assessed by electrode and membrane asymmetry, Electrochim. Acta. 388 (2021) 138631. doi:10.1016/j.electacta.2021.138631.

[46]   Y. Oren, Capacitive deionization (CDI) for desalination and water treatment - past, present and future (a review), Desalination. 228 (2008) 10–29. doi:10.1016/j.desal.2007.08.005.

[47]   H. Wang, T. Yan, P. Liu, G. Chen, L. Shi, J. Zhang, Q. Zhong, D. Zhang, In situ creating interconnected pores across 3D graphene architectures and their application as high performance electrodes for flow-through deionization capacitors, J. Mater. Chem. A. 4 (2016) 4908–4919. doi:10.1039/c5ta10703b.

[48]   X. Gu, Y. Yang, Y. Hu, M. Hu, J. Huang, C. Wang, Nitrogen-doped graphene composites as efficient electrodes with enhanced capacitive deionization performance, RSC Adv. 4 (2014) 63189–63199. doi:10.1039/c4ra11468j.

[49]   S. Zhang, Y. Wang, X. Han, Y. Cai, S. Xu, Optimizing the fabrication of carbon nanotube electrode for effective capacitive deionization via electrophoretic deposition strategy, Prog. Nat. Sci. Mater. Int. 28 (2018) 251–257. doi:10.1016/j.pnsc.2018.02.010.

[50]   X. Liu, H. Liu, M. Mi, W. Kong, Y. Ge, J. Hu, Nitrogen-doped hierarchical porous carbon aerogel for high-performance capacitive deionization, Sep. Purif. Technol. 224 (2019) 44–50. doi:10.1016/j.seppur.2019.05.010.

[51]   O. Sufiani, J. Elisadiki, R.L. Machunda, Y.A.C. Jande, Modification strategies to enhance electrosorption performance of activated carbon electrodes for capacitive deionization applications, J. Electroanal. Chem. 848 (2019) 113328. doi:10.1016/j.jelechem.2019.113328.

[52]   R.L. Zornitta, F.J. García-Mateos, J.J. Lado, J. Rodríguez-Mirasol, T. Cordero, P. Hammer, L.A.M. Ruotolo, High-performance activated carbon from polyaniline for capacitive deionization Jos e, Carbon N. Y. 123 (2017) 318–333. doi:10.1016/j.carbon.2017.07.071.

[53]   S. Zhao, T. Yan, Z. Wang, J. Zhang, L. Shi, D. Zhang, Removal of NaCl from saltwater solutions using micro/mesoporous carbon sheets derived from watermelon peel via deionization capacitors, RSC Adv. 7 (2017) 4297–4305. doi:10.1039/c6ra27127h.

[54]   M. Qian, X.Y. Xuan, L.K. Pan, S.Q. Gong, Porous carbon electrodes from activated wasted coffee grounds for capacitive deionization, Ionics (Kiel). 25 (2019) 3443–3452. doi:10.1007/s11581-019-02887-9.

[55]   J. Kim, Y. Yi, D.H. Peck, S.H. Yoon, D.H. Jung, H.S. Park, Controlling hierarchical porous

structures of rice-husk-derived carbons for improved capacitive deionization performance, Environ. Sci. Nano. 6 (2019) 916–924. doi:10.1039/c8en01181h.

[56] A.P. Silva, A. Argondizo, P.T. Juchen, L.A.M. Ruotolo, Ultrafast capacitive deionization using rice husk activated carbon electrodes, Sep. Purif. Technol. 271 (2021) 118872. doi:10.1016/j.seppur.2021.118872.

[57] J. Elisadiki, Y.A.C. Jande, R.L. Machunda, T.E. Kibona, Y. Abeid, C. Jande, R. Lazaro, Porous carbon derived from Artocarpus heterophyllus peels for capacitive deionization electrodes, Carbon N. Y. 147 (2019) 582–593. doi:10.1016/j.carbon.2019.03.036.

[58] P.A. Chen, H.C. Cheng, H.P. Wang, Activated carbon recycled from bitter-tea and palm shell wastes for capacitive desalination of salt water, J. Clean. Prod. 174 (2018) 927–932. doi:10.1016/j.jclepro.2017.11.034.

[59] C.A.G. Quispe, C.J.R. Coronado, J.A. Carvalho, Glycerol: Production, consumption, prices, characterization and new trends in combustion, Renew. Sustain. Energy Rev. 27 (2013) 475–493. doi:10.1016/j.rser.2013.06.017.

[60] R.S. Ribeiro, A.M.T. Silva, M.T. Pinho, J.L. Figueiredo, J.L. Faria, H.T. Gomes, Development of glycerol-based metal-free carbon materials for environmental catalytic applications, Catal. Today. 240 (2015) 61–66. doi:10.1016/j.cattod.2014.03.048.

[61] M. Anitha, S.K. Kamarudin, N.T. Kofli, The potential of glycerol as a value-added commodity, Chem. Eng. J. 295 (2016) 119–130. doi:10.1016/j.cej.2016.03.012.

[62] S. Hu, X. Luo, C. Wan, Y. Li, Characterization of crude glycerol from biodiesel plants, J. Agric. Food Chem. 60 (2012) 5915–5921. doi:10.1021/jf3008629.

[63] M. Gonçalves, C.S. Castro, I.K.V. Boas, F.C. Soler, E.D.C. Pinto, R.L. Lavall, W.A. Carvalho, Glycerin waste as sustainable precursor for activated carbon production: Adsorption properties and application in supercapacitors, J. Environ. Chem. Eng. 7 (2019) 103059. doi:10.1016/j.jece.2019.103059.

[64] A.B. Leoneti, V. Aragão-Leoneti, S.V.W.B. de Oliveira, Glycerol as a by-product of biodiesel production in Brazil: Alternatives for the use of unrefined glycerol, Renew. Energy. 45 (2012) 138–145. doi:10.1016/j.renene.2012.02.032.

[65] J.M. Clacens, Y. Pouilloux, J. Barrault, Selective etherification of glycerol to polyglycerols over impregnated basic MCM-41 type mesoporous catalysts, Appl. Catal. A Gen. 227 (2002) 181–190. doi:10.1016/S0926-860X(01)00920-6.

[66] H. Kunieda, A. Akahane, Jin-Feng, M. Ishitobi, Phase behavior of polyglycerol didodecanoates in water, J. Colloid Interface Sci. 245 (2002) 365–370. doi:10.1006/jcis.2001.8000.

[67] K.A. Oudhoff, F.A. Vandamme, E.P. Edwin, P.J. Schoenmakers, W.T. Kok, Characterization of glycerin-based polyols by capillary electrophoresis, J. Chromatogr. A. 1046 (2004) 263–269. doi:10.1016/j.chroma.2004.06.097.

[68] A. Hejna, P. Kosmela, K. Formela, Ł. Piszczyk, J.T. Haponiuk, Potential applications of crude glycerol in polymer technology–Current state and perspectives, Renew. Sustain. Energy Rev. 66 (2016) 449–475. doi:10.1016/j.rser.2016.08.020.

[69] N.S.M.N.M. Din, Z. Idris, Y.S. Kian, H.A. Hassan, Preparation of polyglycerol from palm-biodiesel crude glycerin, J. Oil Palm Res. 25 (2013) 289–297.

[70] X. Luo, X. Ge, S. Cui, Y. Li, Value-added processing of crude glycerol into chemicals and polymers, Bioresour. Technol. 215 (2016) 144–154. doi:10.1016/j.biortech.2016.03.042.

[71] J.A. Melero, G. Vicente, M. Paniagua, G. Morales, P. Muñoz, Etherification of biodiesel-derived glycerol with ethanol for fuel formulation over sulfonic modified catalysts, Bioresour. Technol. 103 (2012) 142–151. doi:10.1016/j.biortech.2011.09.105.

[72] Y.K. Krisnandi, R. Eckelt, M. Schneider, A. Martin, M. Richter, Glycerol upgrading over zeolites by batch-reactor liquid-phase oligomerization: Heterogeneous versus homogeneous reaction, ChemSusChem. 1 (2008) 835–844. doi:10.1002/cssc.200800128.

[73] M.S. Khayoon, B.H. Hameed, Synthesis of hybrid SBA-15 functionalized with molybdophosphoric acid as efficient catalyst for glycerol esterification to fuel additives, Appl. Catal. A Gen. 433–434 (2012) 152–161. doi:10.1016/j.apcata.2012.05.013.

[74] C. García-Sancho, R. Moreno-Tost, J.M. Mérida-Robles, J. Santamaría-González, A. Jiménez-López, P.M. Torres, Etherification of glycerol to polyglycerols over MgAl mixed oxides, Catal. Today. 167 (2011) 84–90. doi:10.1016/j.cattod.2010.11.062.

[75] A.M. Ruppert, J.D. Meeldijk, B.W.M. Kuipers, B.H. Erné, B.M. Weckhuysen, Glycerol etherification over highly active CaO-based materials: New mechanistic aspects and related colloidal particle formation, Chem. - A Eur. J. 14 (2008) 2016–2024. doi:10.1002/chem.200701757.

[76] S. Salehpour, M.A. Dubé, Towards the sustainable production of higher-molecular-weight polyglycerol, Macromol. Chem. Phys. 212 (2011) 1284–1293. doi:10.1002/macp.201100064.

[77] Z. Helwani, M.R. Othman, N. Aziz, J. Kim, W.J.N. Fernando, Solid heterogeneous catalysts for transesterification of triglycerides with methanol: A review, Appl. Catal. A Gen. 363 (2009) 1–10. doi:10.1016/j.apcata.2009.05.021.

[78] S.G. Chopade, K.S. Kulkarni, A.D. Kulkarni, N.S. Topare, Biodiesel from trans-esterification of triglycerides with methanol : a review, Acta Chim. Pharm. Indica. 2 (2012) 8–14.

[79] M. de A. Medeiros, T.M. Cançado, C.M.M. Leite, R.M. Lago, Combined processes of glycerol polymerization/carbonization/activation to produce efficient adsorbents for organic contaminants, J. Chem. Technol. Biotechnol. 87 (2012) 1654–1660. doi:10.1002/jctb.3805.

[80] Y. Cui, J.D. Atkinson, Tailored activated carbon from glycerol: Role of acid dehydrator on physiochemical characteristics and adsorption performance, J. Mater. Chem. A. 5 (2017) 16812–16821. doi:10.1039/c7ta02898a.

[81] J. Ma, J. Ma, C. Zhang, J. Song, W. Dong, T.D. Waite, Flow-electrode capacitive deionization (FCDI) scale-up using a membrane stack con fi guration, Water Res. 168 (2020) 115186. doi:10.1016/j.watres.2019.115186.

[82] C. Zhang, L. Wu, J. Ma, M. Wang, J. Sun, T.D. Waite, Evaluation of long-term performance of a continuously operated flow-electrode CDI system for salt removal from brackish waters, Water Res. 173 (2020) 115580. doi:10.1016/j.watres.2020.115580.

[83] S.C. Yang, H. Kim, S. il Jeon, J. Choi, J. gu Yeo, H. ran Park, J. Jin, D.K. Kim, Analysis of the desalting performance of flow-electrode capacitive deionization under short-circuited closed cycle operation, Desalination. 424 (2017) 110–121. doi:10.1016/j.desal.2017.09.032.

[84] A. Rommerskirchen, C.J. Linnartz, D. Müller, L.K. Willenberg, M. Wessling, Energy

Recovery and Process Design in Continuous Flow-Electrode Capacitive Deionization Processes, ACS Sustain. Chem. Eng. 6 (2018) 13007–13015. doi:10.1021/acssuschemeng.8b02466.

[85] D.I. Oyarzun, A. Hemmatifar, J.W. Palko, M. Stadermann, J.G. Santiago, Adsorption and capacitive regeneration of nitrate using inverted capacitive deionization with surfactant functionalized carbon electrodes, Sep. Purif. Technol. 194 (2018) 410–415. doi:10.1016/j.seppur.2017.11.027.

[86] J. Lee, S. Kim, C. Kim, J. Yoon, Hybrid capacitive deionization to enhance the desalination performance of capacitive techniques, Energy Environ. Sci. 7 (2014) 3683–3689. doi:10.1039/c4ee02378a.

[87] M. Pasta, C.D. Wessells, Y. Cui, F. La Mantia, supporting: A desalination battery, Nano Lett. 12 (2012) 839–843.

[88] A. Siekierka, B. Tomaszewska, M. Bryjak, Lithium capturing from geothermal water by hybrid capacitive deionization, Desalination. 436 (2018) 8–14. doi:10.1016/j.desal.2018.02.003.

[89] M.E. Suss, V. Presser, Water Desalination with Energy Storage Electrode Materials, Joule. 2 (2018) 10–15. doi:10.1016/j.joule.2017.12.010.

[90] S. Shanbhag, Y. Bootwala, J.F. Whitacre, M.S. Mauter, Ion Transport and Competition Effects on NaTi2(PO4)3 and Na4Mn9O18 Selective Insertion Electrode Performance, Langmuir. 33 (2017) 12580–12591. doi:10.1021/acs.langmuir.7b02861.

[91] B. Shapira, E. Avraham, D. Aurbach, Side Reactions in Capacitive Deionization (CDI) Processes: The Role of Oxygen Reduction, Electrochim. Acta. 220 (2016) 285–295. doi:10.1016/j.electacta.2016.10.127.

[92] K.C. Smith, R. Dmello, Na-Ion Desalination (NID) Enabled by Na-Blocking Membranes and Symmetric Na-Intercalation: Porous-Electrode Modeling, J. Electrochem. Soc. 163 (2016) A530–A539. doi:10.1149/2.0761603jes.

[93] J. Lee, K. Jo, J. Lee, S.P. Hong, S. Kim, J. Yoon, Rocking-Chair Capacitive Deionization for Continuous Brackish Water Desalination, ACS Sustain. Chem. Eng. 6 (2018) 10815–10822.

doi:10.1021/acssuschemeng.8b02123.

[94] M.M. Mekonnen, A.Y. Hoekstra, Sustainability: Four billion people facing severe water scarcity, Sci. Adv. 2 (2016) 1–7. doi:10.1126/sciadv.1500323.

[95] A. El Mansouri, M. Hasnaoui, A. Amahmid, S. Hasnaoui, Feasibility analysis of reverse osmosis desalination driven by a solar pond in Mediterranean and semi-arid climates, Energy Convers. Manag. 221 (2020) 113190. doi:10.1016/j.enconman.2020.113190.

[96] A.G. Pandolfo, A.F. Hollenkamp, Carbon properties and their role in supercapacitors, J. Power Sources. 157 (2006) 11–27. doi:10.1016/j.jpowsour.2006.02.065.

[97] D. Lu, W. Cai, Y. Wang, Optimization of the voltage window for long-term capacitive deionization stability, Desalination. 424 (2017) 53–61. doi:10.1016/j.desal.2017.09.026.

[98] L.R. Kumar, S.K. Yellapu, R.D. Tyagi, X. Zhang, A review on variation in crude glycerol composition, bio-valorization of crude and purified glycerol as carbon source for lipid production, Bioresour. Technol. 293 (2019) 122155. doi:10.1016/j.biortech.2019.122155.

[99] M. de A. Medeiros, R.M. Lago, Polimerização do glicerol: uma reação simples e versátil para produzir diferentes materiais a partir do coproduto do biodiesel, Quim. Nova. 34 (2011) 1079–1084.

[100] A.R.C. Bredar, A.L. Chown, A.R. Burton, B.H. Farnum, Electrochemical Impedance Spectroscopy of Metal Oxide Electrodes for Energy Applications, ACS Appl. Energy Mater. 3 (2020) 66–98. doi:10.1021/acsaem.9b01965.

[101] K. Xu, S.P. Ding, T.R. Jow, Toward Reliable Values of Electrochemical Stability Limits for Electrolytes, J. Electrochem. Soc. 146 (1999) 4172–4178. doi:10.1149/1.1392609.

[102] K.M. Barcelos, K.S.G.C. Oliveira, L.A.M. Ruotolo, Insights on the role of interparticle porosity and electrode thickness on capacitive deionization performance for desalination, Desalination. 492 (2020) 114594. doi:10.1016/j.desal.2020.114594.

[103] J. Lee, P. Srimuk, K. Aristizabal, C. Kim, S. Choudhury, Y.C. Nah, F. Mücklich, V. Presser, Pseudocapacitive Desalination of Brackish Water and Seawater with Vanadium-Pentoxide-Decorated Multiwalled Carbon Nanotubes, ChemSusChem. 10 (2017) 3611–3623.

doi:10.1002/cssc.201701215.

[104] L. Zhao, T. Takimoto, M. Ito, N. Kitagawa, T. Kimura, N. Komatsu, Chromatographic separation of highly soluble diamond nanoparticles prepared by polyglycerol grafting, Angew. Chemie - Int. Ed. 50 (2011) 1388–1392. doi:10.1002/anie.201006310.

[105] W. Shen, Z. Li, Y. Liu, Surface Chemical Functional Groups Modification of Porous Carbon, Recent Patents Chem. Eng. 1 (2008) 27–40. doi:10.2174/2211334710801010027.

[106] M. Almazrouei, S. Elagroudy, I. Janajreh, Transesterification of waste cooking oil: Quality assessment via thermogravimetric analysis, Energy Procedia. 158 (2019) 2070–2076. doi:10.1016/j.egypro.2019.01.478.

[107] J.H. Zhou, Z.J. Sui, J. Zhu, P. Li, D. Chen, Y.C. Dai, W.K. Yuan, Characterization of surface oxygen complexes on carbon nanofibers by TPD, XPS and FT-IR, Carbon N. Y. 45 (2007) 785–796. doi:10.1016/j.carbon.2006.11.019.

[108] H. Marsh, F.R. Reinoso, Activated Carbon, 1st ed., Elsevier Science, 2006.

[109] J.J. Lado, R.L. Zornitta, F.A. Calvi, M.I. Tejedor-tejedor, M.A. Anderson, L.A.M. Ruotolo, Study of sugar cane bagasse fly ash as electrode material for capacitive deionization, J. Anal. Appl. Pyrolysis. 120 (2016) 389–398. doi:10.1016/j.jaap.2016.06.009.

[110] P. Kichambare, J. Kumar, S. Rodrigues, B. Kumar, Electrochemical performance of highly mesoporous nitrogen doped carbon cathode in lithium-oxygen batteries, J. Power Sources. 196 (2011) 3310–3316. doi:10.1016/j.jpowsour.2010.11.112.

[111] M.A. Pimenta, G. Dresselhaus, M.S. Dresselhaus, L.G. Cançado, A. Jorio, R. Saito, Studying disorder in graphite-based systems by Raman spectroscopy, Phys. Chem. Chem. Phys. 9 (2007) 1276–1291. doi:10.1039/b613962k.

[112] K.S. Munir, M. Qian, Y. Li, D.T. Oldfield, P. Kingshott, D.M. Zhu, C. Wen, Quantitative analyses of MWCNT-Ti Powder Mixtures using Raman Spectroscopy: The Influence of Milling Parameters on Nanostructural Evolution, Adv. Eng. Mater. 17 (2015) 1660–1669. doi:10.1002/adem.201500142.

[113] Z. Yue, T. Gao, H. Li, Robust synthesis of carbon@Na4Ti9O20 core-shell nanotubes for

hybrid capacitive deionization with enhanced performance, Desalination. 449 (2019) 69–77. doi:10.1016/j.desal.2018.10.018.

[114] M. Thommes, K. Kaneko, A. V. Neimark, J.P. Olivier, F. Rodriguez-Reinoso, J. Rouquerol, K.S.W. Sing, Physisorption of gases, with special reference to the evaluation of surface area and pore size distribution (IUPAC Technical Report), Pure Appl. Chem. (2015) 1–19. doi:10.1515/pac-2014-1117.

[115] S. Zhao, T. Yan, H. Wang, G. Chen, L. Huang, J. Zhang, L. Shi, D. Zhang, High capacity and high rate capability of nitrogen-doped porous hollow carbon spheres for capacitive deionization, Appl. Surf. Sci. 369 (2016) 460–469. doi:10.1016/j.apsusc.2016.02.085.

[116] Z. Xie, X. Shang, J. Yan, T. Hussain, P. Nie, J. Liu, Biomass-derived porous carbon anode for high-performance capacitive deionization, Electrochim. Acta. 290 (2018) 666–675. doi:10.1016/j.electacta.2018.09.104.

[117] J.J. Lado, R.E. Pérez-Roa, J.J. Wouters, M.I. Tejedor-Tejedor, C. Federspill, M.A. Anderson, Continuous cycling of an asymmetric capacitive deionization system: An evaluation of the electrode performance and stability, J. Environ. Chem. Eng. 3 (2015) 2358–2367. doi:10.1016/j.jece.2015.08.025.

[118] J. Kang, J. Min, S.I. Kim, S.W. Kim, J.H. Jang, Three-level micro–meso–macroporous three-dimensional graphene for highly fast capacitive deionization, Mater. Today Energy. 18 (2020) 100502. doi:10.1016/j.mtener.2020.100502.

[119] Y. Zhao, G. Luo, L. Zhang, L. Gao, D. Zhang, Z. Fan, Nitrogen-doped porous carbon tubes composites derived from metal-organic framework for highly efficient capacitive deionization, Electrochim. Acta. 331 (2020) 135420. doi:10.1016/j.electacta.2019.135420.

[120] I. Cohen, E. Avraham, Y. Bouhadana, A. Soffer, D. Aurbach, Long term stability of capacitive de-ionization processes for water desalination: The challenge of positive electrodes corrosion, Electrochim. Acta. 106 (2013) 91–100. doi:10.1016/j.electacta.2013.05.029.

[121] J.S. Kang, S. Kim, D.Y. Chung, Y.J. Son, K. Jo, X. Su, M.J. Lee, H. Joo, T.A. Hatton, J. Yoon, Y.E. Sung, Rapid Inversion of Surface Charges in Heteroatom-Doped Porous Carbon:

A Route to Robust Electrochemical Desalination, Adv. Funct. Mater. 1909387 (2019) 1–11. doi:10.1002/adfm.201909387.

[122] T. Wu, G. Wang, Q. Dong, B. Qian, Y. Meng, J. Qiu, Asymmetric capacitive deionization utilizing nitric acid treated activated carbon fiber as the cathode, Electrochim. Acta. 176 (2015) 426–433. doi:10.1016/j.electacta.2015.07.037.

[123] W. Tang, D. He, C. Zhang, P. Kovalsky, T.D. Waite, Comparison of Faradaic reactions in capacitive deionization (CDI) and membrane capacitive deionization (MCDI) water treatment processes, Water Res. 120 (2017) 229–237. doi:10.1016/j.watres.2017.05.009.

[124] S. Hand, J.S. Guest, R.D. Cusick, Technoeconomic Analysis of Brackish Water Capacitive Deionization: Navigating Tradeoffs between Performance, Lifetime, and Material Costs, Environ. Sci. Technol. 53 (2019) 13353–13363. doi:10.1021/acs.est.9b04347.

[125] G. Quan, H. Wang, F. Zhu, J. Yan, Porous biomass carbon coated with SiO2 as High performance electrodes for capacitive deionization, BioResources. 13 (2018) 437–449. doi:10.15376/biores.13.1.437-449.

[126] A.M. Dehkhoda, N. Ellis, E. Gyenge, Effect of activated biochar porous structure on the capacitive deionization of NaCl and ZnCl2 solutions, Microporous Mesoporous Mater. 224 (2016) 217–228. doi:10.1016/j.micromeso.2015.11.041.

[127] G. Quan, L. Chu, X. Han, C. Ding, T. Chen, J. Yan, Facile synthesis of novel hierarchically porous carbon derived from nature biomass for enhanced removal of NaCl, Water Sci. Technol. 74 (2016) 1821–1831. doi:10.2166/wst.2016.372.

[128] M.E. Suss, S. Porada, X. Sun, P.M. Biesheuvel, J. Yoon, V. Presser, Water desalination via capacitive deionization: what is it and what can we expect from it?, Energy Environ. Sci. 8 (2015) 2296–2319. doi:10.1039/c5ee00519a.

[129] W. Xing, J. Liang, W. Tang, D. He, M. Yan, X. Wang, Y. Luo, N. Tang, M. Huang, Versatile applications of capacitive deionization (CDI)-based technologies, Desalination. 482 (2020) 114390. doi:10.1016/j.desal.2020.114390.

[130] S.D. Datar, K. Mohanapriya, D.J. Ahirrao, N. Jha, Comparative study of electrosorption performance of solar reduced graphene oxide in flow-between and flow-through capacitive

deionization architectures, Sep. Purif. Technol. 257 (2021) 117972. doi:10.1016/j.seppur.2020.117972.

[131] E.M. Remillard, A.N. Shocron, J. Rahill, M.E. Suss, C.D. Vecitis, A direct comparison of flow-by and flow-through capacitive deionization, Desalination. 444 (2018) 169–177. doi:10.1016/j.desal.2018.01.018.

[132] I. Cohen, E. Avraham, Y. Bouhadana, A. Soffer, D. Aurbach, The effect of the flow-regime, reversal of polarization, and oxygen on the long term stability in capacitive de-ionization processes, Electrochim. Acta. 153 (2015) 106–114. doi:10.1016/j.electacta.2014.12.007.

[133] L. Xu, L. Tang, S. Peng, Y. Mao, D. Wu, Magnetic array for efficient and stable Flow-electrode capacitive deionization, Chem. Eng. J. 446 (2022) 137415. doi:10.1016/j.cej.2022.137415.

[134] P.T. Juchen, K.M. Barcelos, K.S.G.C. Oliveira, L.A.M. Ruotolo, Using crude residual glycerol as precursor of sustainable activated carbon electrodes for capacitive deionization desalination, Chem. Eng. J. 429 (2022) 132209. doi:10.1016/j.cej.2021.132209.

[135] B. Han, G. Cheng, Y. Wang, X. Wang, Structure and functionality design of novel carbon and faradaic electrode materials for high-performance capacitive deionization, Chem. Eng. J. 360 (2019) 364–384. doi:10.1016/j.cej.2018.11.236.

[136] Y. Qu, P.G. Campbell, L. Gu, J.M. Knipe, E. Dzenitis, J.G. Santiago, M. Stadermann, Energy consumption analysis of constant voltage and constant current operations in capacitive deionization, Desalination. 400 (2016) 18–24. doi:10.1016/j.desal.2016.09.014.

[137] C. Tsouris, R. Mayes, J. Kiggans, K. Sharma, S. Yiacoumi, D. DePaoli, Mesoporous carbon for capacitive deionization of saline water, Env. Sci Technol. 45 (2011) 10243–10249. doi:10.1021/es201551e.

[138] S.J. Seo, H. Jeon, J.K. Lee, G.Y. Kim, D. Park, H. Nojima, J. Lee, S.H. Moon, Investigation on removal of hardness ions by capacitive deionization (CDI) for water softening applications, Water Res. 44 (2010) 2267–2275. doi:10.1016/j.watres.2009.10.020.

[139] A.M. Dehkhoda, N. Ellis, E. Gyenge, Electrosorption on activated biochar: Effect of thermo-chemical activation treatment on the electric double layer capacitance, J. Appl. Electrochem.

44 (2014) 141–157. doi:10.1007/s10800-013-0616-4.

[140] C. Boyadjiev, Mass Transfer Theories. In: Theoretical Chemical Engineering, in: Theor. Chem. Eng. Model. Simul., 2010: pp. 1–594. doi:10.1007/978-3-642-10778-8.

[141] C.H. Hou, C. Liang, S. Yiacoumi, S. Dai, C. Tsouris, Electrosorption capacitance of nanostructured carbon-based materials, J. Colloid Interface Sci. 302 (2006) 54–61. doi:10.1016/j.jcis.2006.06.009.

[142] K.L. Yang, T.Y. Ying, S. Yiacoumi, C. Tsouris, E.S. Vittoratos, Electrosorption of ions from aqueous solutions by nanostructured carbon aerogel, Langmuir. 17 (2001) 1961–1969. doi:10.1006/jcis.2002.8314.

[143] J.N. Israelachvili, Intermolecular and Surface Forces, Third, Academic Press, 2011. doi:https://doi.org/10.1016/C2009-0-21560-1.

[144] J.H. Choi, Determination of the electrode potential causing Faradaic reactions in membrane capacitive deionization, Desalination. 347 (2014) 224–229. doi:10.1016/j.desal.2014.06.004.

[145] J. Kang, T. Kim, K. Jo, J. Yoon, Comparison of salt adsorption capacity and energy consumption between constant current and constant voltage operation in capacitive deionization, Desalination. 352 (2014) 52–57. doi:10.1016/j.desal.2014.08.009.

[146] J.J. Lado, V. Cartolano, E. García-Quismondo, G. García, I. Almonacid, V. Senatore, V. Naddeo, J. Palma, M.A. Anderson, Performance analysis of a capacitive deionization stack for brackish water desalination, Desalination. 501 (2021). doi:10.1016/j.desal.2020.114912.

[147] Y.A. Chen, C.S. Fan, C.H. Hou, Optimizing the energetic performance of capacitive deionization devices with unipolar and bipolar connections under constant current charging, J. Taiwan Inst. Chem. Eng. 93 (2018) 201–210. doi:10.1016/j.jtice.2018.06.039.

6   ACADEMIC PRODUCTION

6.1   Journals

JUCHEN, PATRICIA T.; RUOTOLO, LUÍS A.M. Roles of mass transfer and cell architecture in electrochemical desalination performance using polyglycerol activated carbon electrodes. CHEMICAL ENGINEERING JOURNAL, v. 452, p. 139226, 2023.

JUCHEN, PATRICIA T.; BARCELOS, KAMILLA M.; OLIVEIRA, KAÍQUE S.G.C.; RUOTOLO, LUÍS A.M. Using crude residual glycerol as precursor of sustainable activated carbon electrodes for capacitive deionization desalination. CHEMICAL ENGINEERING JOURNAL, v. 429, p. 132209, 2022.

SILVA, ALESSANDRA P.; ARGONDIZO, ALEXANDRE; JUCHEN, PATRICIA T.; RUOTOLO, LUÍS A.M. Ultrafast capacitive deionization using rice husk activated carbon electrodes. SEPARATION AND PURIFICATION TECHNOLOGY, v. 271, p. 118872, 2021.

6.2   Conferences

JUCHEN, P. T.; BARCELOS, K. M.; RUOTOLO, L. A. M. Carvões ativados obtidos a partir do glicerol residual de biodiesel e sua aplicação como eletrodos para dessalinização eletroquímica. In: XXIV Congreso de la Sociedad Iberoamericana de Electroquímica SIBAE 2020, 2020.

JUCHEN, P. T.; BARCELOS, K. M.; RUOTOLO, L. A. M. Dessalinização por deionização capacitiva utilizando eletrodos assimétricos de carvão ativado de poliglicerol. In: XXIV Congreso de la Sociedad Iberoamericana de Electroquímica SIBAE 2020, 2020.

JUCHEN, P. T.; BARCELOS, K. M.; OLIVEIRA, K. S. G. C.; RUOTOLO, L. A. M. Asymmetric electrochemical desalination using activated carbon electrodes produced with residual glycerol of biodiesel. In: XXIII Simpósio Brasileiro de Eletroquímica e Eletroanalítica, XXIII SIBEE, 2021.

7   APPENDIX
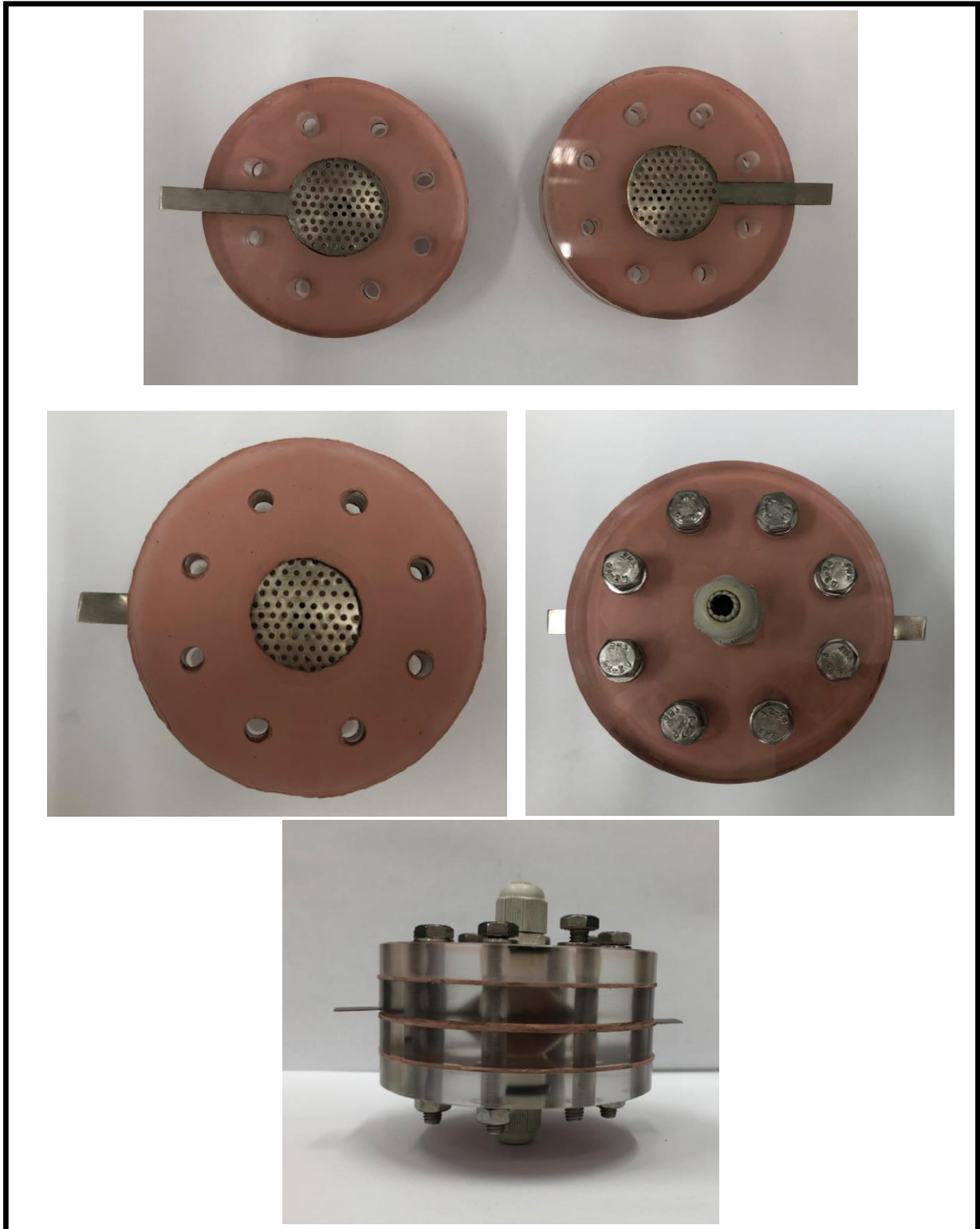

Figure 7.1. Detailed photos of the flow-by cell (FBC).

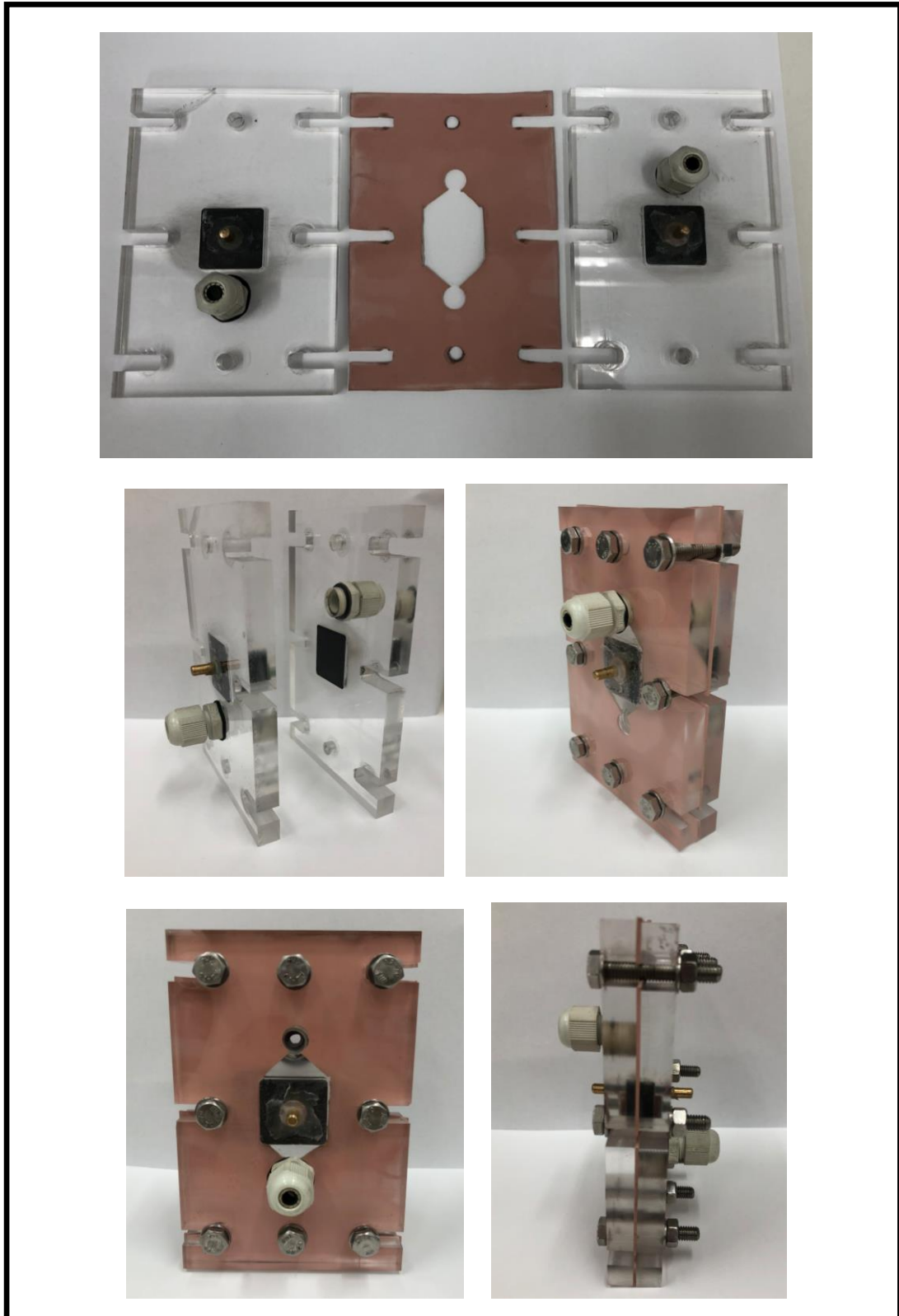**Figure 7.2**. Detailed photos of the flow-through cell (FTC).

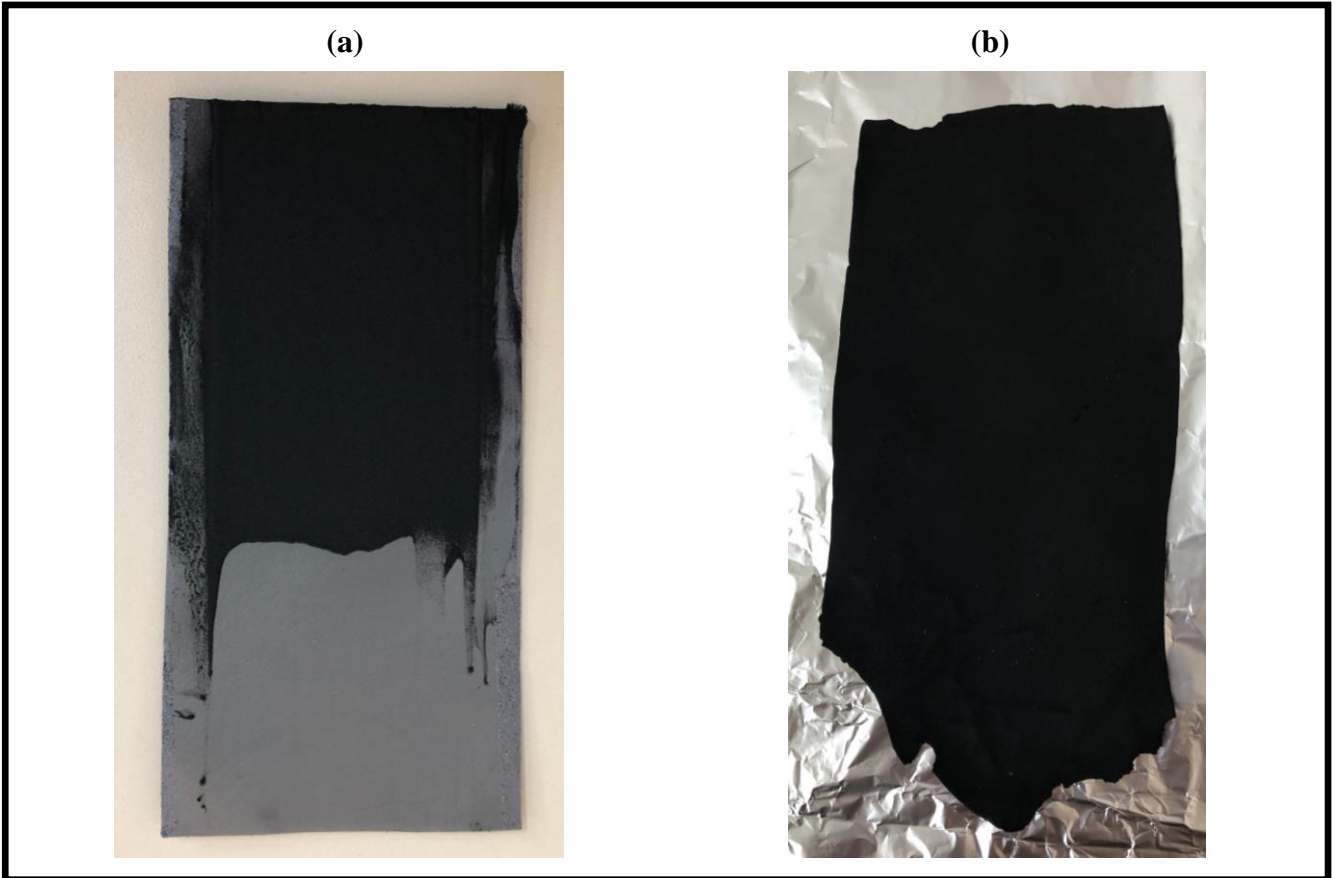**Figure 7.3**. Detailed photos of the Percolation flow cell (PFC).

Figure 7.4. Photos of the electrodes prepared by **(a)** blade-casting (BC) and **(b)** free-standing (FS) procedures, respectively.